Preliminary Design for a Storm Surge Barrier in Tokyo Bay

Final Report

CEGM3000: Multi-Disciplinary Project

MDP Group 386

TU Delft

Preliminary Design for a Storm Surge Barrier in Tokyo Bay

Final Report

by

MDP Group 386

Student Name	Student Number
Pieter André de la Porte	5184754
Cecilia de Bruin	5402212
Eveliina Moonen	5231655
Josephine Sloots	5058104
Seppe Smeijers	4793692
Jens Ulenkate	5212391

Supervisors:	Prof. dr. ir. S. N. Jonkman, TU Delft
	Mr. dr. ir. C. Mai Van, TU Delft
	Dr. ir. A.A. Verhagen, TU Delft
	Prof. dr. ir. M. Esteban, Waseda University
Project Duration:	September 1, 2025 - November 10, 2025
Faculty:	Faculty of Civil Engineering and Geoscience, TU Delft
Cover image:	Cityscape of Tokyo city with the Rainbow bridge Free Photo from Vecteezy

TU Delft

Preface

This report presents the results of a Multidisciplinary Project focused on the preliminary design of a storm surge barrier in Tokyo Bay. The Multidisciplinary Project (MDP) is part of the Master's program in Civil Engineering and Geosciences at Delft University of Technology and aims to explore a topic that benefits from collaboration across different disciplines. The project brought together six students with diverse fields of expertise within Civil Engineering and Geosciences, including Coastal Engineering, Hydraulic and Offshore Structures, and Remote Sensing. It provided a unique opportunity to work on a real and highly relevant engineering challenge from our different backgrounds through a collaboration between Waseda University and Delft University of Technology.

Over the course of ten weeks in Tokyo, we had the privilege of working closely with experts, meeting inspiring professionals, and experiencing the culture and hospitality of Japan. The project has been an invaluable professional and personal experience for all of us.

A special thanks goes out to Prof. dr. ir. M. Esteban from Waseda University for giving us this amazing opportunity. His efforts in connecting us with important and insightful contacts, as well as his thorough feedback and his support and guidance, and the significant amount of time he devoted to our project, have been invaluable to its success.

Furthermore, would like to express our gratitude to our supervisors from TU Delft for their guidance, support, and the considerable time they dedicated to our project. Their constructive feedback has been essential to the success of our work. We especially thank prof. dr. ir. S. N. Jonkman, Mr. dr. ir. C. Mai Van, and Dr. ir. A. A. Verhagen.

We would also like to recognize the valuable support of Marc Walraven from Rijkswaterstaat/I-STORM for funding our project and for sharing his valuable insights and expertise throughout the process. His support and enthusiasm have been inspirational throughout our MDP.

In addition to our main supervisors, we would also like to acknowledge the many others who contributed to this project by sharing valuable feedback, information and contacts. A special thanks goes out to Annie-sensei from the University of Tokyo, Tsuchiya-sensei from the Japan Riverfront Research Centre, Mikami-sensei from Waseda University, Kato-sensei from the Ministery of Land, Infrastructure, Transport and Tourism, Akiyama-sensei from Waseda University, Takagi-sensei from the Institute of Science Tokyo, Nakayasu-sensei from Kanadevia Corporation, and all those who supported us along the way.

MDP Group 386
Tokyo, November 2025

Abstract

Tokyo Bay likely faces increasing risks of typhoon-induced flooding as sea level rises and typhoons intensify under climate change. A storm surge barrier (SSB) has been proposed to mitigate this risk, yet little investigated. This study presents initial considerations regarding a potential configuration for a SSB protecting Tokyo.

The barrier's requirements and location are identified through boundary conditions and a criteria analysis, respectively. For dimensioning, typhoon parameters (wind speed, atmospheric pressure, wind direction, and precipitation) are derived through probabilistic analysis. A one-dimensional model evaluates water levels during a typhoon to assess the potential SSB location and dimensions. Finally, key SSB dimensions are derived using rules of thumb.

Preliminary results suggest that an effective SSB could be located between Haneda Airport and Disneyland. The concept comprises ungated caisson sections separated by a navigational gate and flow inlets equipped with flap gates, offering both storm surge protection and runoff storage capacity. However, this study represents an initial, system-wide assessment at a relatively coarse level. Despite simplifications, the study finds river-ocean interaction crucial for Tokyo, as the surge could induce river flooding during typhoons.

Summary

Tokyo Bay is vulnerable to a variety of natural hazards, including typhoon-induced flooding. The existing coastal defense system is unlikely to withstand the extreme water levels that are expected due to future sea level rise and intensifying typhoons due to climate change (Hoshino et al. (2016b); Nakamura et al. (2020)). Within Tokyo Bay, the city of Tokyo is particularly vulnerable due to its low-lying topography (Takagi et al., 2023), large population and economic importance (Esteban et al., 2014), making it the primary focus area of this study.

To enhance urban resilience in Tokyo, the Tokyo Metropolitan Government introduced the TOKYO Resilience Plan in 2022 (Tokyo Metropolitan Government, 2023). An alternative or complementary approach would be the construction of a storm surge barrier (SSB) (Esteban et al., 2014). To the authors' knowledge, very limited research has been done regarding a SSB for Tokyo Bay as a solution to the flood risk problems. To date, Tsuchiya (2024) and Ohta (2024) have explored a storm surge barrier (SSB) for Tokyo Bay, while hypothetical barriers at the bay entrance have been investigated by Fuentes (2014) and Tian (2014). However, these studies have not examined the associated storage capacity behind a hypothetical barrier located close to the city of Tokyo.

Consequently, the aim of this study is to provide preliminary insights regarding the possible location and configuration, including conceptual dimensions for a SSB to protect Tokyo Bay, and specifically Tokyo, against flooding associated with typhoons.

First, a boundary condition analysis is performed to obtain an overview of the context, constraints, and influencing factors that shape all subsequent design decisions. The aspects considered include an environmental assessment, reference projects, and conditions set by stakeholders and field experts, resulting in the functional requirements of the barrier. Subsequently, the most promising location for the SSB is determined via a Multi-Criteria Decision Analysis (MCDA) with criteria based on the stakeholder analysis: costs, protectiveness, accessibility, and technical feasibility. The relative importance of the criteria was determined by the pairwise ranking method, and the results were further substantiated using a Cost-Property Value Analysis.

A design typhoon, upon which the barrier is dimensioned and for which the storage capacity is evaluated, is determined using two approaches. In Method 1, the storm surge and precipitation intensities during the design typhoon are assumed to be independent variables. The storm surge is determined by wind speed, pressure, and wind direction. The design wind speeds (18 hours before landfall) are considered the main variable to which the others are linked, and are derived from a Poisson process and a Generalized Pareto Distribution using the Peak Over Threshold Method. The design precipitation is obtained from a fitted parametric distribution, applied for precipitation rates 6 hours prior to landfall and rates 10 hours after landfall, based on surge duration (Kawai & Takemura, 2003). The combinations are found by pre-defining return periods for the two parameters.

In Method 2, the partial correlation between the storm surge, represented by wind speed from which pressure and wind direction follow, and precipitation is incorporated through a joint probability analysis by fitting the Frank copula to the two univariate distributions, as described by Method 1, and by applying a Monte Carlo simulation in order to find the parameter combinations corresponding to the design typhoon.

The combinations following either two methods resulting in the most critical water levels (when evaluating the storage capacity or determining hydraulic loads in the model), are referred to as the critical combinations of parameters of a design typhoon. The 1D-model is used to find the critical water levels during a surge in the bay, which are modeled separately as the water level behind and in front of the barrier. The simulation is started at barrier closure with gates reopening once the basin and bay levels equalize. The boundary conditions for the 1D-model include sea-level rise, subsidence, tides, storage capacity, barrier closure timing, and base river discharge. Other input parameters are determined by

the evaluated combinations of the design typhoon, including storm surge, peak river discharge, and waves. Here, the storm surge is estimated by the empirical formula by Horikawa (1978) correlating storm surges with pressure, wind speed, and wind direction, obtained 18 hours before landfall, following the proposed relationship between surge height and wind speed by Needham and Keim (2013). The peak river discharge is derived through a simple hydrological model.

Once water levels are evaluated in the 1D-model, with the maximum head difference found, the critical load on the SSB can be determined. This results in the design requirements used for the preliminary design of SSB components, such as the gates, flow inlets, and the ungated sections. In the present exercise, some very rough conceptual designs are provided, based on hydraulic loads derived from Voorendt (2022) and the EurOtop (2018), and navigational requirements following PIANC – The World Association for Waterborne Transport Infrastructure (2014) guidelines. These are for illustrative purposes only. Gate selection is based upon a MCDA to evaluate six gate types for constructability, space, maintenance, and operation. The selected gate is dimensioned for the design scenario given the critical wind speed, with provisions for secondary functions and adaptability to future climate conditions. Again, only for illustrative purposes.

Preliminary results suggest that an effective SSB could be located between Haneda Airport and Disneyland. The boundary condition analysis established a design lifetime of 150 years (starting construction sometime in the second half of the 21st century) for the barrier, which should be dimensioned for a 200-year return period storm.

Following Method 1 and Method 2, respectively 6 and roughly 600 typhoon events, are obtained for a 200-year return period. The critical scenario for the storage capacity, as identified by the 1D-model, occurs when the gates are closed at high tide, coinciding with a peak discharge of 11221 $[m^3/s]$ and a surge level of 1.30 $[m]$. This results in a maximum bay water level of +4.1 $[m]$ T.P. during barrier closure, and +4.3 $[m]$ T.P. for the full storm surge cycle. The resulting critical combination of parameters of a design typhoon are a wind speed of 53.6 $[m/s]$ and precipitation of 45.9 $[mm/6hr]$ and 137.4 $[mm/10hr]$. Yet, during the surge cycle in this event, the water levels remain below the dike crest at +5.6 $[m]$ A.P. (= +6.73 $[m]$ T.P.), including the 95% confidence bounds.

The maximum hydraulic load is defined as the maximum head difference over the barrier and derived from a predefined event described by Method 1, giving Δh is 3.8 $[m]$, not yet incorporating waves. In this scenario, a storm surge height of 1.4 $[m]$ is generated by a wind speed of 58.4 $[m/s]$ with negligible precipitation while the barrier is closed at low tide. This forms the basis for dimensioning the SSB gates and ungated barrier sections.

The MCDA for gate selection suggests the flap gate as the most optimal, with a height of 32.86 $[m]$ and a width of 22.22 $[m]$ as conceptual key dimensions for the navigational gate. Flow inlets with a gate height of 27.01$[m]$ are required, spanning a total length of 780$[m]$ of the barrier. The ungated barrier is designed as a horizontally composite caisson, with a crest height of 26 $[m]$, a caisson width of 30 $[m]$, and a base width of the armour unit body equal to 43.5 $[m]$.

For the barrier in Tokyo Bay, secondary functions could include energy generation, using wave or tidal energy (Wavenergy.it S.r.l. (2014); Equinox Ocean Turbines (2025)). Furthermore, the vertical wall on the basin side presents an opportunity for port expansion. Additionally, climate change adaptability can be achieved by designing the substructure for multiple gate sizes or by over-dimensioning the foundation to allow future heightening of the ungated barrier.

In conclusion, preliminary results of this study suggest that an SSB could be located between Haneda Airport and Disneyland effectively protecting Tokyo. The concept comprises ungated caisson sections separated by a navigational gate and flow inlets equipped with flap gates, offering both storm surge protection and runoff storage capacity. Furthermore, the study finds that storage capacity behind the barrier is essential for Tokyo, as during typhoons in which heavy rainfall and storm surges coincide, river discharge into the bay is obstructed. Therefore, the primary function of this barrier in Tokyo Bay is to prevent typhoon-induced surges from entering Tokyo, while simultaneously providing sufficient storage capacity for river inflows to prevent hinterland flooding. However, this study represents an initial, system-wide assessment at a relatively coarse level. The main sources of uncertainty in the current study lie in the representation of river–ocean interaction (including backwater effects), hydrological modeling, and the dimensioning of the SSB, highlighting these as priority topics for further research.

Contents

List of Figures

List of Tables

1

Introduction

This chapter serves as an introduction to the report. It begins with a general introduction in Section 1.1, followed by a description of the problem in Section 1.2, which leads into the report's objectives in Section 1.3, addressing the main research question and outlining the approach used to address it.

1.1. General introduction

Tokyo Bay is vulnerable to a variety of natural hazards, including typhoon-induced flooding. The existing coastal defense system is unlikely to withstand the extreme water levels that are expected due to future sea level rise and intensifying typhoons due to climate change (Nakamura et al. (2020); Hoshino et al. (2016b)). Tokyo Bay is surrounded by many big cities, and the economic consequences of such flooding would be serious (Hoshino et al., 2016b). Within Tokyo Bay, the city of Tokyo is particularly vulnerable due to its low-lying topography (Takagi et al., 2023), large population, and economic importance (Esteban et al., 2014), making it the primary focus area of this study.

To enhance urban resilience in Tokyo, the Tokyo Metropolitan Government introduced the *TOKYO Resilience Plan* in 2022. This initiative includes expanding underground storage, constructing high-standard levees to manage heavy precipitation, and raising seawalls to mitigate storm surges and sea-level rise (Tokyo Metropolitan Government (2025a); Esteban et al. (2014)). An alternative or complementary approach is the construction of a storm surge barrier, hereinafter referred to as SSB or barrier, which Esteban et al. (2014) identifies as a potentially more efficient solution for increasing protection levels in Tokyo Bay, and specifically in Tokyo. The primary function of this barrier in Tokyo Bay is to prevent typhoon-induced surges from entering Tokyo, while simultaneously providing sufficient storage capacity for river inflows to prevent backward flooding.

The aim of this report is to provide preliminary insights for a SSB protecting Tokyo against floodings associated with typhoons.

1.2. Problem description

As noted in Section 1.1, Tokyo Bay faces significant challenges from natural disasters, which are expected to intensify due to climate change (Esteban et al., 2014).

This section provides the context and background for the project, emphasizing the importance of protecting Tokyo Bay and its surrounding communities against floodings. First, it introduces the reader to the economic value of the Tokyo Bay area for Japan and the scale of Tokyo Bay and especially the Tokyo Metropolitan Area. Then it discusses the threat of flooding caused by typhoons to Tokyo Bay and the limitations of the current coastal defense system in Tokyo. Consequently, the need for additional protection measures follows, such as a storm surge barrier.

1.2.1. Introduction to Tokyo Bay and Tokyo

Tokyo Bay is situated in the southern Kantō region of Japan, bordering Tokyo, Kanagawa Prefecture, and Chiba Prefecture along the southern shore of the island of Honshu. Connecting to the Pacific Ocean via the Uraga Channel, the land areas around Tokyo Bay form one of Japan's most populated and industrialized regions. These cover approximately $[1,500\ km^2]$, and has been extended by roughly $[249\ km^2]$ of new land through land reclamation conducted through the course of the past centuries, particularly in the 20th century.

Tokyo Bay serves as a major hub for transportation and commerce. Several of Japan's busiest ports are located along the Bay's shoreline, including Tokyo, Yokohama, Chiba, Kawasaki, Yokosuka, and Kisarazu ports, all vital to the national and regional economy (Lloyds Bank Trade – International Trade Portal, 2025). The bay is fed by numerous rivers, notably the Arakawa, Edogawa, Tamagawa, and Nakagawa (Japan Science and Technology Agency, 2019). An overview of the bay is given in Figure 1.1.

Figure 1.1: Tokyo Bay (Google Maps, 2025).

Looking specifically at Tokyo, the main rivers that flow through Tokyo into Tokyo Bay are the Arakawa, Edogawa, and Tama Rivers (Parker, 2016), as shown in Figure 1.2.

Figure 1.2: Tokyo Rivers (Google Maps, 2025).

The Greater Tokyo Area, encompassing Tokyo and parts of six neighboring prefectures, is the world's highest populated metropolitan area, with approximately 37.8 million inhabitants (Invest Tokyo, Tokyo Metropolitan Government, 2018). Tokyo, the capital and most populated city of Japan, is home to over 14 million residents. Economically, Tokyo accounts for a nominal GDP of 113.7 trillion yen (US$1.04 trillion) (Invest Tokyo, Tokyo Metropolitan Government, 2018).

Within Tokyo Bay, the city of Tokyo is particularly vulnerable due to its low-lying topography (Takagi et al., 2023), large population, and economic importance (Esteban et al., 2014), making it the primary focus area of this study.

1.2.2. Flooding in Tokyo due to typhoons

This subsection introduces the threat of flooding in Tokyo due to typhoons. It first provides general information about typhoons in Japan, followed by an explanation of the mechanisms that contribute to flooding in the city, which leads to a short description of historic flood events, and concludes with a description of the existing flood defense infrastructure.

Typhoon characteristics for Japan

In Japan, a tropical storm with wind speeds exceeding 17 $[m/s]$ is classified as a typhoon (Typhoon, n.d.-b). The characteristics of a typhoon include low atmospheric pressure, strong rotating winds, and heavy rainfall (World Meteorological Organization, 2023).

On average, about 30 typhoons form each year over the northwest Pacific Ocean, with most making landfall in Japan between May and October, and the peak season occurring in August and September. Typhoons occurring later in the season tend to be stronger than those earlier. Typically, typhoons move at a relatively slow pace of 2040 $[km/hr]$, and their paths can be predicted with reasonable accuracy (Guide, n.d.). The strongest winds are usually located on the right side of the storm's forward motion, particularly in the right-front quadrant (Oceanic & Administration, 2023). Typhoons achieve their greatest intensity while over warm tropical waters, but they begin to weaken as soon as they move inland (PAGASA, n.d.).

Flooding mechanisms

In Tokyo, the risk of flooding primarily arises from the simultaneous occurrence of heavy precipitation and storm surge induced by strong winds during a typhoon (Sekine et al., 2020). It is thus hypothesized that for Tokyo the greatest flood risk occurs during typhoons in which heavy rainfall and storm surges coincide, restricting river discharge into the bay.

Storm surge

In case of a typhoon event, both the atmospheric pressure drop and strong winds contribute to the development of the surge. The decrease in atmospheric pressure reduces the downward force exerted by the atmosphere on the water column beneath the sea surface, causing the water level to rise. This phenomenon is known as the inverse barometer effect (Gornitz, 2017).

In addition, wind plays a significant role in the formation of storm surges. The wind stress exerted on the sea surface depends on both its strength and its direction relative to the coastline. The influence of wind on sea level increases inversely with water depth (Gornitz, 2017). However, not all typhoons generate storm surges in Tokyo Bay. Md. Rezuanul Islam (2020) conducted a sensitivity analysis and found that for Tokyo Bay, the direction of the typhoon path, landfall location and forward speed also affect storm surge development. The study further determined that the most hazardous storm surge scenario in the upper bay occurs when a typhoon moves parallel to the longitudinal axis of Tokyo Bay and makes landfall approximately 25 $[km]$ southwest of the bay.

Heavy precipitation

Heavy precipitation during the passage of a typhoon occurs because warm ocean water evaporates rapidly under the influence of strong winds. This process saturates the lower atmosphere with water vapor. The moist air is then forced upward by the low atmospheric pressure at the storm's center, expanding and cooling as it rises. As the air cools, the water vapor condenses into droplets, forming thick clouds (ClickView, 2017). The most intense rainfall typically occurs in the ring of thunderstorms surrounding the eye, while bands of heavy rain can extend hundreds of kilometers outward. Throughout the typhoon's lifetime, the heaviest precipitation generally occurs to the right of the cyclone's track, within approximately six hours before and after landfall (NOAA, 2005).

The greatest flood risk arises when high river discharges from heavy precipitation coincide with a storm surge. Under these conditions, rivers might be unable to discharge effectively into the bay due to elevated water levels in the bay, which could lead to the rivers flooding into the city. As Tokyo is traversed by numerous rivers (see Figure 1.2), flood risk represents a major concern for the city.

Current flood defense system for Tokyo

In the current flood defense system of Tokyo, two main components can be distinguished:

- **Tidal barrier line**: designed to protect the city from elevated sea levels during storm surges;
- **River defense system**: aimed at preventing fluvial flooding from rivers.

The tidal barrier line consists of 15 floodgates, 21 flood embankments, and approximately 60 $[km]$ of continuous seawall. This barrier line stands about 5 to 8 times higher than the average low-water level in the bay. Under normal conditions, the floodgates remain open to allow vessel passage and river discharge. During a storm surge, however, the gates are closed, and a pumping system is activated to prevent rising water levels within the rivers (Tokyo Metropolitan Government & Harbor, 2023).

The river defense system comprises the following main components:

- **Creation of space for the river**: Additional capacity is created through the construction of retention ponds, underground storage areas, and diversion channels. The Arakawa Floodway is an example of a diversion channel that enables flood control of the Sumida River. At the bifurcation point, a floodgate closes and diverts excess water into the Arakawa River (Stalenberg & Vrijling, 2009).
- **Flood-retaining structures**: Quay walls and flood walls are constructed along urban rivers, while super levees are implemented along major rivers to provide enhanced flood protection (Stalenberg & Vrijling, 2009).

Historic flood events

The largest storm surge–induced disaster in Tokyo Bay occurred during the Taisho Typhoon of 1917, which caused extensive flooding as a result of both storm surge and river overflow. The disaster claimed 1,301 lives and injured 2,215 people (Tatekoji et al., 2016). The recorded storm surge level reached 2.1 $[m]$ (Hoshino et al., 2012), occurring during spring high tide. Typhoon Taisho landed near Namazu in Suruga Bay, which is around 150 $[km]$ from Tokyo (Tatekoji et al., 2016). The typhoon track is illustrated in Figure 1.3.

A more recent flooding event is Typhoon Hagibis which struck Japan in 2019 with maximum sustained wind speeds of approximately 62.5 $[m/s]$ and the highest total rainfall on record, exceeding 1 $[m]$ in 48 $[hr]$, causing extensive flooding and landslides across multiple regions (BBC News, 2019). The event

resulted in at least 95 fatalities, while more than 93,000 residential and commercial structures were damaged or destroyed. The total economic losses were estimated at around $10 billion (Insurance Journal, 2019).

Typhoon Hagibis was particularly destructive due to its angle of approach and landfall location. The storm remained offshore until making landfall 130 $[km]$ southwest of Tokyo, allowing it to draw energy from the sea for an extended period. Upon landfall, it interacted with upper-level jet stream winds, which distributed the strongest winds across a larger area than usual (Voiland, 2019). The typhoon track is shown in Figure 1.3. The storm surge associated with Hagibis produced a sea-level anomaly of 2 $[m]$ at the head of Tokyo Bay. However, the inner densely populated areas around the bay experienced only minor coastal damage, partly because the peak surge coincided with a low spring tide (Shimozono et al., 2020).

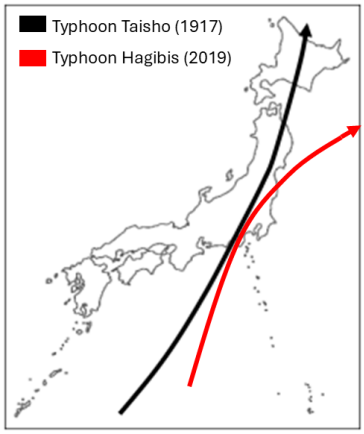

Figure 1.3: Typhoon tracks for typhoon Taisho (1917) and typhoon Hagibis (2019), alternated from Hoshino et al., 2012.

1.2.3. Storm surge barrier as a potential solution for Tokyo Bay

Despite the extensive flood defense system, Esteban et al. (2014) predict significant challenges because of the combined effect of an increase in typhoon intensity and sea level rise. As a result, many communities around Tokyo Bay face significant risks and potentially severe economic consequences. One proposed measure to enhance regional protection is the construction of a storm surge barrier, which Esteban et al. (2014) identifies as a potentially more efficient solution for safeguarding Tokyo Bay, and particularly Tokyo, than increasing the height of existing levees. Examples of successful applications of a SSB include the Maeslant Barrier and the Thames Barrier, both of which have proven to be effective solutions for coastal flood protection (Zhong et al., 2012; McVeigh, 2023).
This preliminary analysis is based on the hypothesis that the water defenses in the city of Tokyo are struggling to provide adequate protection against extreme water levels in the bay, driven by rising sea levels and increasingly intense typhoons, while also maintaining sufficient storage capacity for river discharge following extreme precipitation during typhoon events. Therefore, the primary function of this barrier in Tokyo Bay is to prevent typhoon-induced surges from entering Tokyo, while simultaneously providing sufficient storage capacity for river inflows to prevent backward flooding.

This leads to the research objectives of this report, which are presented in Section 1.3.

1.3. Research objectives

As mentioned before, the aim of this report is to provide preliminary insights for a SSB protecting Tokyo Bay, and specifically to protect Tokyo against floodings associated with typhoons. To the authors' knowledge, some studies have been conducted in the past (Fuentes, 2014; Ohta, 2024; Tian, 2014; Tsuchiya, 2024). These studies have not conducted research to the storage capacity behind the barrier in combination with conceptual configurations and dimensions. The main research question addressed

in this report is defined as:

> *What could be a preliminary design of a storm surge barrier that protects Tokyo Bay and specifically Tokyo from severe flooding during an extreme storm surge in combination with heavy precipitation resulting from a typhoon?*

To address the main research question, the following sub-questions should be answered:

> *a. What are the boundary conditions and functional requirements for designing a possible storm surge barrier protecting Tokyo Bay, and specifically Tokyo?*
>
> *b. What is a viable location for a storm surge barrier protecting Tokyo Bay, and specifically Tokyo?*
>
> *c. For what design typhoon should the storm surge barrier protect Tokyo Bay, and specifically Tokyo?*
>
> *d. How sufficient is the storage capacity at the selected barrier location to accommodate river discharge to protect Tokyo Bay, and specifically Tokyo during a storm surge induced by a typhoon?*
>
> *e. What would be the dimensions of the storm surge barrier to protect Tokyo Bay, and specifically Tokyo against floodings induced by typhoons?*

The boundary conditions and functional requirements (sub-question a) are determined based on literature research and interviews. The applied method is described in Section 2.1, and the results are presented in Section 3.1.

Based on the identified boundary conditions and additionally performed literature research, a potentially suitable location for the barrier (sub-question b) is identified using a Multi-Criteria Decision Analysis (MCDA) evaluating multiple possible barrier locations. The methodology is outlined in Section 2.2, and the corresponding results are discussed in Section 3.2.

The typhoon that the barrier at the location following the MCDA must withstand (sub-question c) is referred to as the design typhoon. The method proposed to derive this design typhoon is described in Section 2.3, with results presented in Section 3.3.

Using the design typhoon and the selected location, a one-dimensional hydrodynamic model, also referred to as a 1D-model, is developed to simulate the water levels behind and in front of the barrier following the interaction between surge and river run-off during a typhoon. The methodology for this model is provided in Section 2.4, and the corresponding results, showing water levels behind and in front of the barrier, are presented in Section 3.4. The results include an evaluation of the storage capacity at the selected location (sub-question d), and the resulting 1D-model can be used for the derivation of design parameters, such as surge height, required for dimensioning the barrier.

Finally, a preliminary system design for the storm surge barrier is developed (sub-question e) with the applied methods described in Section 2.5, 2.6, and 2.7 and the resulting preliminary design shown in Section 3.5, 3.6, and Section 3.7.1, where particular attention is given to the gate design.

In Appendix A, the project flow chart is presented. This chart illustrates which disciplines contributed to each section of the project and highlights areas of overlap where knowledge was shared between disciplines to enable progress across the different fields of work.

2

Methodology

This chapter describes the methodology followed to answer the main research question by addressing each of the sub-questions.

Firstly, in Section 2.1, a boundary condition analysis is conducted based on a literature review and interviews. The analysis includes an environmental, and stakeholder analysis, and a study of reference projects, all resulting in the definition of functional requirements. As a first design step, in Section 2.2, criteria are selected for a Multi-Criteria Decision Analysis (MCDA), which is applied to identify the most promising location for the barrier. Additionally, a cost-property value analysis based on literature is performed to validate the selected location.

Afterwards, the methodology for finding the design typhoon for the Tokyo Bay area is explained in Section 2.3. This design typhoon is used to define the components of the 1D-model and the design parameters for dimensioning the barrier. To establish the design typhoon, values must be obtained for key typhoon parameters. This is achieved using two methods: the first treats storm surge and precipitation independently, while the second considers them jointly by fitting a joint probability distribution. Once the design typhoon has been defined, the methodology for constructing the 1D-model is presented in Section 2.4, including the boundary conditions, typhoon-related parameters, and the underlying mathematical formulations of the water level behind and in front of the barrier. The 1D-model is used to determine whether the selected barrier location has sufficient storage capacity and the maximum hydraulic load on the barrier required for dimensioning the barrier. The combination of typhoon parameters resulting in the critical storage capacity and maximum hydraulic load are referred to as the critical combinations of the design typhoon.

Lastly, the methods applied to derive the design of the system and the design of the main structural components of the SSB are presented in Section 2.5, 2.6, and 2.7. Criteria are defined for a second MCDA to identify the most suitable gate type. In addition, the methodology to derive a conceptual design of the gates including key dimensions, is presented. Lastly, the methodology for a load assessment is outlined.

2.1. Boundary condition analysis

A boundary condition analysis is performed to obtain an overview of the context, constraints, and influencing factors that shape all subsequent design decisions and considerations. It provides the basis for creating solutions that are both technically feasible and aligned with site-specific conditions. Accordingly, an environmental assessment and stakeholder analysis are performed. Consequently, the functional requirements are determined. These elements are derived through a combination of literature review, expert interviews (see Appendix B and C), and reference projects.

2.1.1. Environmental analysis

To understand the conditions under which the SSB must be designed, an environmental analysis of Tokyo Bay and its surrounding areas is conducted. This analysis examines the geological, ecological, and economic characteristics of the region.

Geology

In order to explore and evaluate possible locations of the potential SSB, the geological conditions of the Tokyo Bay and Tokyo Metropolitan Area are summarized below. This includes the bathymetry of Tokyo Bay, the elevation of the surrounding land, subsoil conditions, and seismic activity.

A contour map of Tokyo Bay was generated using data with a resolution of 500 $[m]$, provided by the Japan Oceanographic Data Center (Japan Oceanographic Data Center, n.d.). This way, the costs and technical feasibility related to the depths of a SSB would be assessed.

The vulnerable areas within the Tokyo Bay Area must be identified to determine an effective location for the SSB. Using the elevation map provided by Tokyo Metropolitan Government (2025b), the low-lying zones prone to inundation during extreme typhoon events are highlighted. These areas are particularly at risk in the case of storm surges combined with peak river discharges resulting from intense precipitation during a typhoon.

Soil conditions are analyzed to find feasible locations for the placement and construction of components of the SSB, such as navigational gates. The soil conditions are found in a reference report from Kaizuka, 1993.

Since Tokyo Bay is subjected to earthquakes, seismic hazards should be taken into account while designing the SSB. Estimates of hazard classification and probability of occurrence are obtained from studies from ThinkHazard! (2025) and Stein et al. (2006). Design standards follow from the Building Standard Law of Japan (Kuramoto, 2006). Using these findings, proper mitigation measures can be included in the design.

Ecology

The potential SSB should avoid interference with the ecological system as much as possible. Therefore, ecological hubs, habitat types, and species interactions within the Tokyo Bay area are identified through literature review and analysis of environmental databases.

The SSB should have as little impact as possible on existing ecological conditions to ensure the preservation of fish migration, water quality, and natural tidal flats. Therefore, flow inlets are included into the design to allow for connectivity between riverine and marine systems. Section 2.6 elaborates on a possible flow inlet design.

Economics

The economic context serves to determine the economic value of important infrastructure in areas around the bay that are at risk of flooding. Therefore, it is essential to identify critical industries and infrastructure in the Tokyo Bay area that are subjected to storm surge–induced flooding. Literature sources, national databases, Google Earth, and reports from the Ministry of Land, Infrastructure, Transport and Tourism (MLIT) were reviewed to map ports and shipping routes. Industrial areas and transportation networks were reviewed as potential economic factors, however, these factors fall outside the scope of the analysis. Statistical data on port capacities, GDP contribution, and transport throughput were used to evaluate the economic significance of the bay area.

Furthermore, future development trends, such as increases in vessel size and the expansion of port facilities, are considered to assess long-term protection requirements and to ensure that the SSB performs effectively throughout its design life.

2.1.2. Stakeholder analysis

The construction of a SSB in Tokyo Bay would affect a wide range of parties, each with different interests and responsibilities, and some with much influence and power. These interests must be taken into account in the design process to generate as much support as possible. Therefore, a stakeholder analysis was conducted to identify the relevant parties and their interests.

Information was gathered from policy documents, government reports, expert interviews, and academic literature to determine their roles, interests, and potential conflicts.

2.1.3. Study of reference projects

To gain insight into potential design approaches and feasible dimensions of structural components, several reference projects were studied. These references serve as an example to help identify opportunities and constraints relevant to the environmental and spatial conditions of Tokyo Bay. From Mooyaart and Jonkman (2017), three major storm surge barriers were selected for analysis: the St. Petersburg Barrier, the MOSE Barrier in Venice, and the Eastern Scheldt Barrier, due to their comparable functional and hydraulic challenges, such as large navigational openings and depths. In addition, two other large-scale hydraulic structures, the Dutch Closure Dam and the Hartel Barrier, were reviewed to provide complementary insights into multi-functionality, ecological impact, and operational reliability.

2.1.4. Functional requirements

The functional requirements follow from the boundary condition analysis and define the functions that the SSB must perform. They primarily indicate the types of events against which the barrier should provide protection, and the design life of the barrier is also specified. In addition, considerations such as climate change, added value, redundancy, and the preservation of existing activities in the bay, both economic and ecological, are incorporated into the functional requirements.

2.2. Location

The most promising location for the barrier is determined via an MCDA analysis. The resulting barrier location is most likely to fulfill the requirements determined in Section 2.1.

In the following sections, the methodology for obtaining the most promising barrier location is presented. First, possible locations are defined, which is followed by a first verification step whether they are technically feasible. The remaining locations are evaluated using an MCDA, and the results are validated with a cost-property value analysis. Consequently, the most promising barrier location can be found.

2.2.1. Possible locations

First, several locations are defined for the possible location of the SSB based on span length, bathymetry, and protected area. Locations are defined either by prioritizing outcomes of the boundary condition analysis or by providing an alternative to a previously evaluated location. By analyzing and integrating the bathymetry, the average depth, maximum depth, total span, and wet cross-sectional area of each location are determined. These variables are later used to assess the locations.

2.2.2. Conceptual verification

Secondly, the identified locations undergo a conceptual verification process to assess their technical and physical feasibility. This is done by evaluating the maximum depth, since a large depth significantly increases construction complexity, costs, and therefore risks as well. The St. Petersburg SSB has the world's largest vertical gate height of 23.5 $[m]$ (Hunter, 2012). Assuming technical innovation in the future, this value is multiplied by a factor of 1.5 to obtain a limit for the maximum depth, resulting in a practical depth limit of approximately 35 $[m]$. All locations that have a maximum depth equal or larger than 35 $[m]$ are discarded based on technical feasibility.

2.2.3. MCDA

The locations remaining after the conceptual verification in Section 2.2.2 are compared by means of a Multi-Criteria Decision Analysis to evaluate their potential and feasibility.

Criteria

Based on the stakeholder analysis in Section 2.1.2, four main criteria and three sub-criteria are formulated. The four main criteria considered are: *costs*, *protectiveness*, *accessibility*, and *technical feasibility*. Regarding protectiveness, three subcriteria are formulated: *residential area*, *port area* and *ecological habitats*. Each location is assigned a qualitative score on each criterion corresponding to its perfor-

mance on that criterion, see Table 2.1.

Table 2.1: Qualitative scoring system using symbols.

Symbol	Value	Meaning
++	5	Excellent
+	4	Good
0	3	Moderate
-	2	Fair
–	1	Poor

The performance of each location per criterion is found by establishing a formula per criterion. The derivation of the formulas is explained for each criterion in Appendix D.

Weights

Since not all criteria are considered equally important, weights are determined to account for their significance. This way, a more realistic comparison can be made of the locations in terms of total score. To execute this as objectively as possible, a pairwise ranking method is applied. Each criterion is compared with every other one in pairs. For each comparison, based on the stakeholder analysis and expert interviews, it is decided which of the two is judged to be more important and should therefore receive a higher weight using a ranking matrix. By assigning a 1 in the ranking matrix, the row criterion is preferred over the column criterion; a 0 means it is not preferred. If two criteria both receive a 1 respective to each other this means that they are of equal importance. Each row is summed horizontally. To ensure that all criteria obtain a non-zero weight, the criterion with a horizontal sum of 0 is given a 1, and all other total scores are doubled. Next, the obtained scores are normalized, to reflect the relative importance. This method is applied for both the main as well as the sub criteria.

Determining the final MCDA scores

The scores of the locations are multiplied by the corresponding weights, and the weighted sum is retrieved for each location. The location that has the highest weighted sum is considered to be the most likely location to fulfill the requirements determined in Section 2.1.

2.2.4. Validation: Cost-property value analysis

Lastly, the results of the MCDA are validated by estimating the costs of each location and property value that is safeguarded by each barrier location. This way, initial findings of the economic efficiency of the potential barrier locations are obtained. The analysis consists of three main components: cost estimation, property value estimation, and cost-property value ratio evaluation. The methodology for calculating the costs and property value estimation is explained in Appendix G.

Cost-Property Value Ratio

The property value-cost ratio ($^{PV}/_{C}$) is calculated as the ratio of property value to costs for each location.

$$\frac{\text{PV}}{\text{C}} = \frac{\text{Property Value}}{\text{Costs}}$$

A ratio greater than 1 indicates economic viability. The higher the ratio, the more cost-effective the location regarding property value. The results from this cost-property value analysis are compared with the results of the MCDA to validate the outcome of the MCDA. If the highest property value-cost ratio coincides with the outcome of the MCDA, the MCDA is assumed to be further substantiated.

2.3. Design typhoon for Tokyo

In this section, the methodology for determining the typhoon used to evaluate Location 7 and design the barrier is described. This typhoon represents the critical event associated with a 200-year return period and is therefore referred to as the design typhoon, as it defines the conditions for which the barrier is designed. The design typhoon is used to determine components of the 1D-model as described in

Section 2.4, namely the storm surge height h_{surge} and the amount of precipitation h_{precip} for a certain return period. Furthermore, the surge height and other parameters belonging to the design typhoon can be used to determine the design parameters required for dimensioning the barrier in Section 2.5. In order to determine the design typhoon, values need to be found for important typhoon parameters. In this report the parameters wind speed, atmospheric pressure, and wind direction are used to determine the storm surge, in which wind speed (specifically wind speed 18 hours prior to landfall) is considered the main variable to represent the storm surge as described in Section 2.4.2.

This report proposes two methods to determine the design typhoon, the first method considers the storm surge height and precipitation intensity independent from each other and combines the two components through return periods chosen per component (Method 1). The second method does consider the storm surge height and precipitation intensity together by fitting a joint probability distribution for which one return period can be used to determine the design typhoon (Method 2). It should be noted that the occurrence of storm surge and rainfall during a typhoon is highly correlated, however, the storm surge height and precipitation intensity are not strongly correlated. Therefore, the magnitudes of the two components are treated statistically independent in Method 1, while in Method 2, their joint behavior is represented through a bivariate probability distribution.

In summary, the report proposes two different methods to derive the design typhoon. The design typhoon can be described by four parameters: wind speed, atmospheric pressure, wind direction, and precipitation, where different combinations of the parameters still lead to the design typhoon. The different combinations following from the design typhoon can be evaluated with the 1D-model as described in Section 2.4.

In this section, first Method 1 is discussed, followed by Method 2. Much of Method 1 can also be used in Method 2, therefore, only the difference between the two methods is explained in Section 2.3.3

2.3.1. Method 1: Storm surge variables

This section describes the methodology for deriving design values for wind speed, atmospheric pressure, and wind direction. First, the data used to determine these parameters is presented, followed by a discussion of the methods employed to obtain the design values for each parameter.

Data to determine surge

Ideally only data of typhoons that hit Tokyo would be used to obtain the most realistic results. However, there is only limited data for Tokyo due to a comparative lack of typhoons affecting the city, increasing the chance of biased results when fitting probability distributions. As a result, in the proposed approach, the area of interest for selecting typhoons that are used in the analysis is expanded to the Northwestern Pacific to include a larger number of typhoons. The dataset includes the typhoon name, date, longitude, latitude, wind speed, atmospheric pressure, and storm track direction.

Additionally, the dataset including the typhoons obtained in the area of interest is filtered based on the occurrence of landfall events, following the approach described by Needham and Keim (2013). To apply the correlation identified by Needham and Keim, as explained in Section 2.4.2, the wind speeds 18 hours prior to landfall are determined for each qualifying typhoon in the dataset. As a result, only typhoons with landfall events were considered where the typhoon had to be above the ocean for 18 hours before a landfall event for a wind speed to be stored. As this database will be used in a Peak Over Threshold method following Extreme Value Analysis, the typhoon has to be above the ocean 18 hours straight before it can be considered an independent landfall event, which is further explained in Section 2.3.1.

Consequently, the database includes the date, longitude, latitude, wind speed, atmospheric pressure, and storm track direction 18 hours prior to landfall for typhoons that have been above the ocean for 18 hours straight until landfall. This decreased the size of the database and is assumed to be a reasonable approach as only typhoons that make landfall are of interest for Tokyo as they can create a surge in Tokyo, as described in Section 1.2. This database is further referred to as $Database_{T,NWP}$.

In addition to $Database_{T,NWP}$, a second database is created to store the typhoons that made landfall in Tokyo, further referred to as $Database_{T,T}$. This is done by filtering the the 18-hour prior to landfall derived dataset ($Database_{T,NWP}$) using the specific typhoon data of Tokyo. The typhoons that made landfall in Tokyo which are included in $Database_{T,T}$.

Consequently, the data selection process results in two distinct databases: the Typhoon Northwestern Pacific database ($Database_{T,NWP}$) and the Typhoon Tokyo database ($Database_{T,T}$).

Wind speed

The goal of this section is to determine the probability per year of a typhoon with a wind speed W exceeding w hitting Tokyo with the direction to create a surge:

$$P[W > w|\text{Hitting Tokyo in direction of surge}].$$

The direction to create a surge also includes the fact that the typhoon needs to make landfall as explained in Section 2.3.1.

In order to find the wind speeds belonging to a typhoon with the design return period, the extremes are of interest. As a result, in this analysis, the Peak Over Threshold (POT) method is performed, originating from Extreme Value Analysis theory, which evaluates the extremes in data. The POT is performed on the $Database_{T,NWP}$ to increase the number of typhoons evaluated and therefore arrive to a more representative distribution as explained in Section 2.3.1. In Section 2.3.1 it is explained how from the GPD modeling the Northwestern Pacific typhoons, the typhoons in Tokyo can be described. Consequently, this section explains how eventually the probability per year of a typhoon reaching Tokyo with the direction to cause a surge with a wind speed 18 hours prior to landfall exceeding w is determined.

Peak Over Threshold - POT

In this method, a threshold wind speed is set, where afterwards a GPD is fitted to the typhoon events exceeding the threshold. The mathematical formulation of the GPD is shown in Equation 2.1.

$$H(y) = \begin{cases} 1 - \left(1 + \dfrac{\xi y}{\sigma_c}\right)^{-\frac{1}{\xi}}, & \text{for } \xi \neq 0 \\ 1 - \exp\left(-\dfrac{y}{\sigma_c}\right), & \text{for } \xi = 0 \end{cases} \tag{2.1}$$

When the GPD is used in POT, it models the exceedance events over a threshold, resulting in the mathematical formulation shown in Equation 2.2, with W wind speed 18 hours before landfall and c the threshold wind speed.

$$P[W > w \mid W > c] = \begin{cases} \left(1 + \dfrac{\xi(w - th)}{\sigma_{th}}\right)^{-\frac{1}{\xi}}, & \text{for } \xi \neq 0, \\ \exp\left(-\dfrac{w - th}{\sigma_{th}}\right), & \text{for } \xi = 0. \end{cases} \tag{2.2}$$

$$\text{Where } \sigma_c = \sigma + \xi(c - \mu)$$

The variables of a GPD in the POT are the shape parameter ξ, the location parameter μ, the scale parameter σ, and the previously named threshold c. As the IBTrACS database only provides information on typhoon events, the probability modeled by the GPD gives the chance of a wind speed 18 hours prior to landfall exceeding a certain wind speed w, given W surpasses the threshold c per storm in the Northwestern Pacific.

To perform the POT, the evaluated events should be independent from each other. A single typhoon can make multiple landfalls, resulting in numerous wind speed values 18-hour prior to landfall. However, these subsequent landfall events can occur soon after each other, which could influence the independence

needed for POT. Independence of the landfall events is assumed by the condition that a typhoon should be on the ocean for 18 hours straight before landfall. If the condition is met, the wind speed is stored. This could imply that a typhoon can have multiple landfall events where the wind speed is stored, as it makes landfall, then goes out to sea again and stays in the ocean for at least 18 hours. However, a typhoon changes dramatically during landfall, therefore the subsequent landfall is considered independent if it has been on the ocean again for 18 hours.

Despite the relatively short data period of 41 years (1984 - 2024), a moving window spanning 21 years with a time shift of 5 years was used to evaluate whether the extremes changed in time. Per moving window, the threshold value has been determined before fitting a GPD using threshold stability plots, to ensure enough extreme typhoon events were left to obtain a relatively reliable fit of the GPD.

The GPD following the POT will give a conditional probability as shown in Equation 2.2. To obtain the unconditional probability, the distribution should be multiplied by the exceedance probability $P[W > c]$:

$$P[W > w] = P[W > w \mid W > c] \cdot P[W > c] = q_{w,18h}$$

Poisson process

Until now, the probability of a wind speed 18 hours prior to landfall exceeding w per typhoon event is obtained. The probability per year of a typhoon reaching Tokyo with the direction to cause a surge with a wind speed 18 hours prior to landfall exceeding w can be modeled via a Poisson process describing $P[N \geq 1]$, with N the number of typhoon events having a wind speed 18 hours prior to Tokyo exceeding w and having the direction of causing a surge. The Poisson process applicable is given by Equation 2.3.

$$\begin{aligned} P[N \geq 1] &= 1 - P[N = 0] \\ P[N \geq 1] &= 1 - \exp(-\lambda \cdot q_{w,18h}) \end{aligned} \tag{2.3}$$

In Equation 2.3, λ represents the number of typhoons coming to Tokyo per year with the direction to create a surge and make landfall. By incorporating $q_{w,18h}$ into the Poisson process, spatial homogeneity is implicitly assumed in the occurrence of typhoons, i.e., that the probability of a typhoon of a given intensity reaching Tokyo is equivalent to that of reaching any other location within the Northwestern Pacific. This assumption is used to simplify the analysis, although the route of typhoons is clearly influenced by geography and macro-level atmospheric processes (including trade winds) and other phenomena. This analysis could lead to conservative results, when in reality, the strongest typhoons are less likely to reach Tokyo. However, as climate change projections show that the severity of typhoons is likely to increase, this assumption could account for some of the expected increased intensity of typhoons (Esteban et al., 2014).

λ is derived by in Equation 2.4, where the total number of typhoons making landfall near Tokyo ($N_{Tokyo,landfall}$) is divided by the number of years evaluated (N_y). For simplicity, it is assumed using Figure 3.6b, that the filtered typhoons making landfall in Tokyo all have the storm direction to create a surge. As a result, λ represents the rate of typhoons coming to Tokyo per year, with the direction to create a surge and make landfall. Additionally, it is assumed that the rate of typhoons stays constant during the entire evaluated time period. This means that despite the parameters of the GPD changing in time thanks to the moving window method, the rate of typhoons stays constant. This assumption stems from the fact that only a limited number of typhoons have arrived in Tokyo through the years, meaning that the probability increases of the changes in the rate through time being biased. Furthermore, climate change projections show that the number of typhoons reaching Tokyo will not increase, but will intensify (Esteban et al., 2014), substantiating the constant λ.

$$\lambda = \frac{N_{Tokyo,landfall}}{N_y} \tag{2.4}$$

Design Wind Speed - $W_{design,RT}$

The design wind speed $W_{design,RT}$ 18 hours prior to landfall can be derived from the design return periods. In Method 1, these are different predetermined return periods RT. The derivation in Equation 2.5 leads to the final $W_{design,RT}$.

$$\begin{aligned} P[N \geq 1] &= \frac{1}{RT} \\ 1 - \exp(-\lambda \cdot q_{w,18h}) &= \frac{1}{RT} \\ q_{w,18h} &= -\frac{\ln\left(1 - \frac{1}{RT}\right)}{\lambda} \\ GPD(W_{\text{design},RT}) &= -\frac{\ln\left(1 - \frac{1}{RT}\right)}{\lambda} \\ W_{\text{design},RT} &= GPD^{-1}\left(-\frac{\ln\left(1 - \frac{1}{RT}\right)}{\lambda}\right) \end{aligned} \tag{2.5}$$

Uncertainty quantification

The uncertainties are quantified by bootstrapping the exceedances used during the single-fit procedure n times. For each iteration, the fitting procedure described in this section is applied. This process results in a dataset of length n containing all fitted parameters for each bootstrap sample. From this dataset, the 95% confidence interval of the fitted distribution describing the 18-hour wind speed prior to landfall can be obtained.

During the bootstrapping procedure, the threshold is kept equal to the threshold of the single-fit procedure, as only the exceedances are bootstrapped, and the bootstrapped data will have the same length each time, such that stability can be assured. However, this method leads to a larger variance than when the entire dataset employed to fit the single-fit GPD is used, as a larger variety between values in the bootstrapped datasets is possible. Yet, if the number of exceedances on which the GPD is fitted were unknown, the stability of the fit cannot be assured. If the threshold is too low, more samples may be included, leading to a biased fit; if it is too high, the limited number of samples may result in large error variance. Next to that, the uncertainty of the rate, λ, for the Poisson process is not quantified for simplicity. Consequently, the confidence bounds obtained through this uncertainty quantification method may be overly optimistic.

Atmospheric pressure

The report proposes to find a relationship between atmospheric pressure and wind speed 18 hours prior to landfall using the $Database_{T,NWP}$. The approach used to find the relationship is described below.

In order to establish a relationship, the atmospheric pressure and wind speed 18 hours prior to landfall are plotted against each other, where the relationship is assumed to be fitted through the data, such as a polynomial of some order. The fitting process is done via a Best Linear Unbiased Estimation BLUE, a least-squares estimation approach as shown in Equation 2.6.

$$\hat{X}_{\text{BLUE}} = \left(A^{\text{T}}\Sigma_Y^{-1}A\right)^{-1} A^{\text{T}}\Sigma_Y^{-1}Y \tag{2.6}$$

Here Y represents the observed atmospheric pressure values with shape $m \times 1$, A represents the design matrix including the entries using the wind speed 18 hours prior to landfall of the to be fitted polynomial for which the coefficients need to be estimated with size $m \times (1 + order) = m \times n$), Σ_Y represents the variance matrix comprising the uncertainty in the observed values with size $m \times m$, here the measured atmospheric pressure 18 hours prior to landfall, and $\hat{x}_{BLUE}$ consists of the estimated coefficients with size $n \times 1$.

The fit of the polynomial is evaluated using the Overall Model Test OMT (Equation 2.7). In equation 2.7, $T_{q=m-n}$ represents the test statistic for q, which is equal to the number of observations m

minus the number of unknowns n. $\hat{e}$ is equal to the observations Y minus the estimated values $\hat{Y} = A\,\hat{x}$, and k_α is the threshold value which can be found for a given false alarm rate α from $\chi^2(q, 0)$. The fitted model is rejected by the OMT if $T_{q=m-n} > k_\alpha$.

$$T_{q=m-n} = \hat{\epsilon}^T \Sigma_Y^{-1} \hat{\epsilon} > k_\alpha \tag{2.7}$$

If the OMT rejects a fitted model, another model is proposed (such a higher-order polynomial). In order to test whether the new model is better than the rejected model alternative hypothesis testing is applied via the Generalized Likelihood Ratio Test GLRT (Equation 2.8). Here $\hat{e}_0$ represents the residuals of the original model and $\hat{e}_a$ the residuals of the alternative model. Additionally, k_α is now derived using α from $\chi^2(q, 0)$ with q equal to the number of additional parameters in the alternative model. Under the GLRT, if $T_q > k_\alpha$, the alternative hypothesis should be accepted thanks to its significantly smaller residuals than the original hypothesis.

$$T_q = \hat{e}_0^T Q_{yy}^{-1} \hat{e}_0 \; - \; \hat{e}_a^T Q_{yy}^{-1} \hat{e}_a > k_\alpha \tag{2.8}$$

Once an alternative hypothesis is accepted, the alternative hypothesis should also pass the OMT. Consequently, this is an iterative process until a model passes the OMT.

Wind direction

In the formula posed by Horikawa, see Section 2.4.2, θ is defined as the angle between the optimal wind direction for generating the largest storm surge and the actual wind direction. The optimal wind direction for the case of Tokyo is determined by Horikawa. The actual wind direction is assumed to be parallel with the storm's track, since the strongest winds are typically located on the right-hand side of the storm's forward motion (Oceanic & Administration, 2023). This can be explained by the fact that the wind turns around the eye of the typhoon, substantiating the assumption that the resultant wind speed is highest where the storm track and wind direction are parallel.

As explained in Section 2.3.1, the landfall events of typhoons in Tokyo are all considered to have a near-ideal wind direction from Figure 3.6b. As a result, the rate λ in the Poisson distribution is assumed to incorporate the number of typhoons with the optimum wind direction to create a storm surge making landfall in Tokyo, resulting in λ describing the number of typhoons making landfall with an optimal or near-optimal wind direction for generating a surge.

2.3.2. Method 1: Precipitation during typhoons in Tokyo

Precipitation Data

For the 1D-model, precipitation data are required for both the period leading up to landfall and the duration of the surge itself. Consequently, these two phases are treated separately, as the behavior of a typhoon changes significantly at the moment of landfall. Before landfall, the typhoon's eye remains over the sea, and precipitation in the Tokyo Bay area mainly results from its outer rainbands, typically at relatively low rates. However, as the typhoon makes landfall, precipitation intensity increases significantly, reaching its most extreme levels (Zhai et al., 2024). As a result, the cumulative precipitation from 6 hours before the moment of landfall until the moment of landfall and the cumulative precipitation from the moment of landfall until 10 hours later have been determined per typhoon for the Tokyo specific database ($Database_{T,T}$) as explained in Section 2.3.1. In contrast to the wind speed 18 hours prior to landfall, rainfall is assumed to be extremely location dependent. Therefore, only Tokyo specific data is used.

The duration of these 6 and 10-hour windows stems from the following considerations. A 6-hour window is assumed to provide a relatively unbiased estimate of the precipitation behavior before landfall in comparison to smaller time windows as it is less dependent on the correct classification of the moment of landfall. Furthermore, 6 hours resembles roughly half a tidal cycle, which is relevant for the 1D-model tidal scenarios. The window duration of 10-hours stems from the fact that a storm surge can remain inside Tokyo Bay for approximately 10 hours, and the corresponding precipitation during this period is of interest (Kawai & Takemura, 2003).

Consequently, two datasets are derived, the first including the cumulative precipitation data from 6 hours before landfall until landfall ($Database_{6hr}$) and the second including the cumulative precipitation data from the moment of landfall until 10 hours later ($Database_{10hr}$).

Possible Correlations

To gain insight into the co-occurrence of rainfall amounts and storm surge height, first a correlation is explored between these two components. More specifically, since wind speed 18 hours prior to landfall is considered the main variable, as explained in Section 2.4.2, a correlation between wind speed intensity 18 hours prior to landfall and precipitation amounts during a typhoon in Tokyo is explored. To determine if a correlation is present, the simple approach of plotting wind speeds against the cumulative precipitation amounts is used, where, after the resulting scatter plots are visually interpreted whether a clear relationship is present.

In addition, the relationship between the 6-hour cumulative rainfall amount prior to landfall and the 10-hour cumulative rainfall amount following landfall is explored to substantiate the assumption made in Section 2.3.2, stating that the precipitation amount prior to landfall is independent from the precipitation amount following landfall. Again, the simple approach of plotting the two variables against each other to visually determine whether a clear relationship is present, is used.

Fitting distributions

For both the 6-hour and 10-hour cumulative precipitation, a parametric distribution is fitted. The goodness of fit is evaluated using graphical methods, such as the QQ-plot and Logscale-plots.

Precipitation design value

The design value for both the 6-hour and 10-hour cumulative precipitation during a typhoon that makes landfall in Tokyo can be derived using Equation 2.9. In Equation 2.9 $P[R > r_{design}]$ stands for the probability per typhoon that makes landfall in Tokyo that the precipitation exceeds the design precipitation for a certain return period. However, here the return period is not in years, but in typhoons (RN) as the probability is per typhoon. This means that a return period of n_{years} is converted to $n_{typhoons}$ by multiplying n_{years} with the rate of the number of typhoons making landfall per year λ derived with Equation 2.4.

$$\begin{aligned} P[R > r_{design}] &= \frac{1}{RN} \\ 1 - P[R \leq r_{design}] &= \frac{1}{RN} \\ 1 - Dist(r_{design}) &= \frac{1}{RN} \\ r_{design} &= Dist^{-1}(1 - \frac{1}{RN}) \end{aligned} \tag{2.9}$$

Uncertainty quantification

The uncertainties are quantified for the 6-hour and 10-hour precipitation distributions by bootstrapping the $Database_{6hr}$ and $Database_{10hr}$ respectively n times. For each iteration, the fitting procedure described in this section is applied. This process results in two datasets, one for the 6-hour and one for the 10-hour precipitation, of length n, containing all fitted parameters for each bootstrap sample. From these datasets, the 95% confidence intervals of the fitted distributions describing the 6-hour cumulative precipitation until landfall and the 10-hour cumulative precipitation from landfall respectively, can be obtained.

2.3.3. Method 2: Joint probability distribution between surge and precipitation

The second method comprises of fitting a joint probability distribution between the storm surge height and precipitation amount. As wind speed 18 hours prior to landfall is considered the main variable as described in Section 2.4.2, the joint probability distribution is fitted between wind speed intensity

18 hours prior to landfall and 6-hour cumulative precipitation amount prior to landfall, and between wind speed intensity 18 hours prior to landfall and 10-hour cumulative precipitation amount following landfall. When determining the storm surge height in Method 2, the parameters atmospheric pressure and wind direction are considered to remain the same as for Method 1.

The approach followed in this report to fit a joint probability distribution is similar to the proposed approach by Um et al. (2017). In the article, first univariate distributions are fitted to the wind speeds and precipitation amounts of typhoons at the Jeju weather station in South Korea. Following graphical and statistical fit tests of the univariate distributions, a copula is fitted using the fitted univariate distributions and the data.

In the method proposed by this report, the bivariate distribution will describe the conditional probability per typhoon of a wind speed W exceeding w and of an amount of precipitation R exceeding r given that W surpasses the threshold c and the typhoon makes landfall in Tokyo:

$$P[W > w, R > r \mid W > c, landfall\ in\ Tokyo].$$

To obtain the probability of such a qualifying typhoon per year, again, the probability is modeled via a Poisson process.

Data

In order to fit the bivariate distribution, only the Tokyo specific database for wind speeds 18 hours prior to landfall derived in Section 2.3.1 ($Database_{T,T}$ and the Tokyo specific database for the 6-hour ($Database_{6hr}$) and 10-hour cumulative precipitation ($Database_{10hr}$) are used. However, only qualifying typhoons where the wind speed 18 hours prior to landfall exceeds c can be used, which reduces the number of data points further. This stems from the fact that the conditional probability is modeled by the bivariate distribution as explained in Section 2.3.3.

Univariate distributions

When fitting the bivariate distributions for this research, the fitted GPD for wind speed 18 hours prior to landfall derived in Section 2.3.1, and the fitted distributions for the 6- and 10-hour cumulative precipitation derived in Section 2.3.2 are used. All of these distributions model the probability per typhoon. This equivalent unit is required for fitting the bivariate distribution.

However, a clear distinction should be made between Method 1 and Method 2 for the GPD, explaining the wind speed 18 hours prior to landfall, as the GPD will model the conditional probability of $P[W > w \mid W > c]$ and not the unconditional probability $P[W > w]$ as derived for Method 1. This originates from the fitting approach used, such that the copula cannot be fitted when the GPD is first multiplied by the exceedance probability $P[W > c]$ to make it unconditional. On the other hand, it will not cause any issues as the extremes are only of interest and it can be accounted for in the fitting process.

Furthermore, again the assumption is made that the probability of a typhoon reaching Tokyo and making landfall is independent of its wind intensity as explained in Section 2.3.1. Under this assumption, the univariate distribution for the wind speed estimated for the Northwest Pacific can be applied directly to the Tokyo area. Rainfall, in contrast, is assumed to be inherently local and therefore remains modeled directly from Tokyo data. Moreover, thanks to its derived independence from wind speed (Section 3.3.2), the fitted parameters of the distributions for precipitation are assumed to remain the same despite that only typhoons in Tokyo with wind speeds 18 hours prior to landfall higher than c are considered.

Bivariate distribution

The bivariate distribution can now be established by fitting a copula between the two univariate distributions (either wind speed intensity and 6-hour cumulative precipitation amount, or wind speed intensity and 10-hour cumulative precipitation amount) and by using the data as specified in Section 2.3.3. As

the wind speed intensity and precipitation amount of a typhoon are considered independent in this report, as explained in Section 2.3.2, the hypothesis is that the Archimedean Frank copula will represent the relationship best thanks to its zero tail dependence property. Furthermore, this is substantiated by Um et al., 2017, who found that the Frank copula could best model the relationship between wind speed intensity and precipitation amount during typhoons. As a result, this report will not attempt to derive which copula describes the relationship between wind speed intensity and precipitation amount best, but assume that the Frank copula can be used to model the relationship based on the previously explained reasoning and article.

In order to fit the copula Maximum Likelihood Estimation was applied using the PyCopula package (blent-ai (Maxime Jumelle), 2025). After fitting the Frank copula, the strength and direction of dependence parameter θ can be obtained.

Poisson process

The bivariate distribution models the probability per typhoon of wind speeds exceeding w and precipitation exceeding r given that w is higher than the threshold c and it makes landfall in Tokyo in the direction to cause a surge. However, the goal is to find the probability of such typhoons making landfall in Tokyo per year. Again, as mentioned before, qualifying typhoons per year probability can be modeled using a Poisson process describing $P[N_q \geq 1]$, with N_q the number of qualifying typhoon events. The Poisson process applicable is given by Equation 2.10.

$$\begin{aligned} P[N_q \geq 1] &= 1 - P[N_q = 0] \\ P[N_q \geq 1] &= 1 - \exp(-\lambda_{q,Tokyo} \cdot p) \end{aligned} \tag{2.10}$$

In Equation 2.3 $p = P[W > w, R > r \mid W > c, landfall\ in\ Tokyo]$, and $\lambda_{q,Tokyo}$ represents the rate of qualifying typhoons per year, such that it has a wind speed 18 hours prior to landfall exceeding c and it makes landfall in Tokyo.

$\lambda_{q,Tokyo}$ is derived in Equation 2.11, where the total number of qualifying typhoons making landfall near Tokyo in the direction to cause a surge ($N_{Tokyo,landfall,q}$) is divided by the number of years evaluated (N_y). Again it is assumed using Figure 3.6b that the filtered typhoons making landfall in Tokyo all have the storm direction to create a surge. As a result, $\lambda_{q,Tokyo}$ represents the rate of qualifying typhoons coming to Tokyo per year, with the direction to create a surge and make landfall.

$$\lambda_{q,Tokyo} = \frac{N_{Tokyo,landfall,q}}{N_y} \tag{2.11}$$

Design wind speed & precipitation - $W_{design,RT}$ & $R_{design,RT}$

The design wind speed 18 hours $W_{design,RT}$ prior to landfall, and the precipitation before and during landfall $R_{design,RT}$, can be derived from the design return period. In Method 2, this is equal to the specified design return period of 200 years in Section 2.1.4. The derivation in Equation 2.12 leads to the design probability per typhoon, which can be fulfilled by multiple combinations of $W_{design,RT}$ and $R_{design,RT}$.

$$\begin{aligned} P[N_q \geq 1] &= \frac{1}{RT} \\ 1 - \exp(-\lambda_{q,Tokyo} \cdot p) &= \frac{1}{RT} \\ p &= -\frac{ln(1 - \frac{1}{RT})}{\lambda_{q,Tokyo}} \end{aligned} \tag{2.12}$$

Determining $W_{design,RT}$ and $R_{design,RT}$ from a bivariate distribution is different than from a univariate distribution. First, a Monte Carlo simulation should be applied, generating N_{MC} samples (here $N_{MC} = 10000$) from the bivariate distribution. Each sample contains a probability for each of the two samples reaching a certain value per typhoon, here ($P[W \leq w_{MC}] = p_{w,MC}$; $P[R \leq r_{MC}] = p_{r,MC}$). By using Equation 2.13 for the wind speed intensity and Equation 2.14 for the precipitation amount, their

corresponding wind speed intensity 18 hours prior to landfall and precipitation amount before or during landfall can be found. This can be done for all probability pairs, where each pair can be plotted with wind speed on the x-axis and precipitation on the y-axis.

$$\begin{aligned} P[W \leq w_{MC}] &= p_{w,MC} \\ GPD(w_{MC} - c) &= p_{w,MC} \\ w_{MC} &= GPD^{-1}(p_{w,MC}) + c \end{aligned} \tag{2.13}$$

$$\begin{aligned} P[R \leq r_{MC}] &= p_{r,MC} \\ Dist(r_{MC}) &= p_{r,MC} \\ r_{MC} &= Dist^{-1}(p_{r,MC}) \end{aligned} \tag{2.14}$$

The resulting design p derived with Equation 2.12 can lead to multiple combinations of values for $W_{design,RT}$ and $R_{design,RT}$ as different combinations can lead to the same probability p. Using the plot with generated values from the bivariate distribution, all combinations of $W_{design,RT}$ and $R_{design,RT}$ can be found that lead to p. Consequently, a single design return period resulting in the design typhoon can lead to multiple combinations of values for $W_{design,RT}$ and $R_{design,RT}$.

However, Method 2 produces two joint probability distributions that each describe the relationship between wind speed and precipitation for a given return period. Since the wind speed values in the two distributions do not align perfectly, it is not possible to directly identify the two corresponding precipitation amounts for the same wind speed. To overcome this, a polynomial is fitted through the resulting possible combinations of $W_{design,RT}$ and $R_{design,RT}$ for one of the joint probability distributions, providing a relationship between wind speed and precipitation. This enables the determination of the two corresponding precipitation values for the wind speed obtained from the other joint probability distribution. In order to fit the polynomial, the same procedure derived in Section 2.3.1 for the atmospheric pressure is applied.

Depending on the evaluation purpose, different combinations of $W_{design,RT}$ and $R_{design,RT}$ can be preferred. For instance, for the 1D-model in Section 2.4, the combination of $W_{design,RT}$ and $R_{design,RT}$ that leads to the maximum water level behind the barrier is explored. On the other hand, for dimensioning certain aspects of the barrier in Section 2.5 the $W_{design,RT}$ and $R_{design,RT}$ combination leading to the highest water level difference between the water level behind the barrier and in front of the barrier is required. These combinations will be referred to as critical combinations.

Uncertainty Quantification

The uncertainty of the bivariate distribution describing the relationship between wind speed and precipitation is not quantified across the entire distribution, similar to Method 1. Instead, the uncertainty is quantified for the resulting critical combinations. To obtain the 95% confidence bounds for the critical combinations, a bootstrapping procedure is applied, resulting in n sets of critical combinations. From these n realizations of critical combinations, the 95% confidence interval for wind speed and precipitation per evaluation purpose can be derived.

The bootstrapping procedure involves resampling the data used to obtain both the marginal distributions and the copula. Specifically, the exceedances used to fit the GPD describing wind speed, as well as the $Database_{6hr}$ and $Database_{10hr}$ used to fit the distributions describing the precipitation amounts, are each bootstrapped n times. In addition, the $Database_{T,T}$ is bootstrapped n times to derive a new subset of qualifying typhoons for each iteration. Consequently, the rate λ for the Poisson process varies per iteration.

In each bootstrap iteration, the newly obtained marginals are used in the copula fitting procedure, together with the resampled qualifying typhoon dataset. The one-dimensional model (derived in Section 2.4) is then executed for each iteration to obtain the critical combinations. Consequently, this

procedure yields the 95% confidence intervals for wind speed and precipitation for the critical combinations derived using Method 2.

2.3.4. Proxy Storm

To validate the outcomes of the proposed design scenarios, a historical event is analyzed. This event, referred to as the proxy storm, serves as a representative case providing a historical record of combined precipitation and wind speed conditions observed 18 hours prior to landfall.

2.4. 1D-model

This section describes the methodology for constructing the 1D-model and is divided into three parts: Section 2.4.1 outlines the methodology for obtaining the boundary conditions required for the 1D-model, Section 2.4.2 outlines the procedure for deriving the parameters related to the water level behind and in front of the barrier influenced by the design typhoon, and Section 2.4.4 presents the mathematical formulation of the 1D-model describing the water levels behind the barrier and in front of the barrier. The components of the 1D-model are illustrated in Figure 2.1.

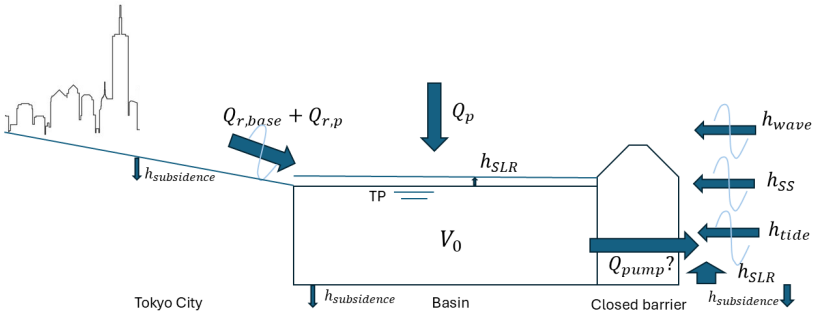

Figure 2.1: 1D-model schematization.

The 1D-model is used to determine whether the selected location of the barrier results in enough storage capacity such that the water level behind the barrier does not exceed the levee heights. The results are discussed in Section 3.4.4. Furthermore, the 1D-model can be used to determine the design hydraulic load for dimensioning the barrier in Section 2.5. The design hydraulic load can be determined by the largest water difference between the water level behind the barrier and in front of the barrier, resulting from a critical combination of wind speed and precipitation. The resulting maximum water level difference is outlined in Section 3.5.2 with the corresponding values for wind speed and precipitation belonging to the typhoon.

2.4.1. Boundary conditions for the 1D-model

The boundary conditions define the model components that are independent of the typhoon and that represent both current and projected future conditions. The boundary conditions for the 1D-model are found through literature research, where in this first simple 1D-model, the boundary conditions considered most important include sea level rise, subsidence, tide, storage capacity, barrier closure time, and the base river discharge. This model does not take into account inner basin geometry and gate configuration.

Sea level rise h_{SLR}

For sea level rise, the NASA projection tool is used (NASA, 2025). The sea level rise accounted for depends on the selected design life of the barrier. Furthermore, a conservative climate scenario is selected as other parameters, for example, parameters representing typhoon intensity, in this report could be seen as optimistic as they do not include climate scenario projections.

Subsidence $h_{subsidence}$
In order to determine whether the subsidence is significant, different literature sources are reviewed.

Tides h_{tide}
A simple approach is used to estimate the design tidal range and period for Tokyo Bay. The tidal range is determined by obtaining the minimum and maximum tidal values in one month observed by a measurement station located within Tokyo Bay, and the tidal period is assumed to be equal to the semi-diurnal period.

Afterwards, simplified analytical formulas are used to estimate the reduction in tidal range within the basin resulting from restricted tidal flow. The presence of the barrier restricts the exchange of water between the bay and the open sea, thereby reducing the tidal prism (the total volume of water that flows in and out of the basin during a tidal cycle (Bosboom & Stive, 2023)). As a consequence, the tidal response is dampened and the amplitude of the tide inside the basin decreases compared to the natural condition without a barrier.

The dampened tidal response has a negative impact on the tidal flats and, consequently, on the ecological activity within the basin. Tidal flats depend on regular inundation and exposure cycles, which sustain diverse habitats for benthic organisms, fish, and migratory birds. A decrease in tidal amplitude reduces the frequency and extent of these inundations, potentially leading to habitat loss, changes in sedimentation patterns, and a decline in biodiversity (Zhao et al., 2020). To limit the tidal range reduction, flow inlets are included in the design, as described in 2.6.2.

The formula for calculating the decreased tidal range is found in (Bosboom & Stive, 2023). This is given in Equation 2.15.

$$A_{eq} = C\,P^{q} \tag{2.15}$$

The equilibrium cross-sectional area (A_{eq}) in Equation 2.15 is estimated based on the assumed gate configuration of the barrier in Section X, see Equation 2.16.

$$A_{eq} = number_{\text{gates}} \times Width_{\text{gate}} \times Depth_{\text{gate}}, \tag{2.16}$$

The corresponding tidal prism (P) is determined through the O'Brien–Jarrett relationship in Equation 2.15, which relates the inlet cross-sectional area to the tidal prism by empirical constants $C = 1.08\times10^{-4}$ and $q = 1.0$. Since Tokyo Bay is determined to be a small basin, $L_{basin} < 1/10 \times L_{tide}$ and using the tidal prism P and the known basin area A_{basin}, the average tidal amplitude can be determined by Equation 2.17 (Bosboom & Stive, 2023).

$$H = \frac{P}{A_{\text{basin}}} \tag{2.17}$$

Equation 2.17 provides a highly simplified estimation and is used to determine the tidal range reduction for a barrier with one navigational gate and multiple flow inlets.

Storage capacity in basin V_0
The storage capacity in the basin (V_0) in cubic meters is determined by evaluating the enclosed surface area and the levee heights. The surface area is estimated using Google Earth (Google, 2025), while research on current and future levee heights is conducted using literature.

Storage volume in a river and catchment area
The storage volumes of reservoirs and retention ponds within the river catchment area are found through literature research.

The storage volume in the river itself when the water level is rising in the river from low to high is calculated through a rough estimation using equation 2.18.

$$\text{Volume} = L \cdot B \cdot H \tag{2.18}$$

with:

- Width (B): Varies depending on the location along the river, estimated from Google Earth Imagery (Earth, n.d.).
- Height (H): The allowable increase in water depth, based on low water level relative to levee heights.
- Length (L): Estimated from the river source to river mouth using Google Earth imagery (Earth, n.d.).

Barrier closure time

To determine the instant of barrier closure and the duration of the closure, reference projects such as the Maeslant Barrier in the Netherlands and the MOSE barrier in Venice are examined. Additional information on surge forecasting and surge duration specifically applicable to Tokyo is obtained through literature review.

River discharge

River discharge is divided into two components in the 1D-model, the base river discharge and the peak river discharge. Base river discharge is considered as a boundary condition since this is independent of typhoon occurrance and intensity. The peak discharge is induced by the typhoon and therefore discussed in Section 2.4.2. In this 1D-model, only the rivers that discharge into the basin created by the barrier are taken into account. The river discharge in the 1D-model originates from the rivers discharging behind the selected location of the barrier. Hereby, it is assumed that the water levels in the basin are sensitive to river discharge, whereas in the bay, water level changes due to river discharges can be neglected. This is based on the difference between the volume enclosed by the basin and the bay.

Base river discharge $Q_{r,base}$

To determine the base (or normal) discharge of the rivers discharging behind the selected location of the barrier, a typhoon–storm surge analysis is first conducted to identify the months during which both typhoon activity and surge threats are most prominent. In this analysis, the number of typhoons is compared with the number of surges per month during the typhoon season. The storm surges considered significant exceed a self-defined threshold of 50 [cm] above mean sea level (T.P.). These surges were then cross-referenced with typhoon records from the Tokyo Typhoon Database (see Section 2.3.1) to determine whether they coincided with typhoon events. From this comparison, the months with the highest frequency of typhoon-induced surges were identified. The river discharge corresponding to these months was then obtained through research of available data and literature.

2.4.2. Input parameters of the 1D-model related to a typhoon

This section introduces the methodology proposed in this report to determine the model components affected by a typhoon that influence the water levels in front of and behind the barrier. The components considered are the storm surge height, peak river discharge, and wave height, as illustrated in Figure 2.1.

Storm surge h_{ss}

To determine the storm surge during the design typhoon, an appropriate relationship must be identified. Several relationships from existing literature have been explored. As described in Section 1.2.2, the storm surge in a typhoon results from both a drop in atmospheric pressure and wind, and this information is used to guide the selection of candidate relationships. The most suitable formula is identified by validating each candidate against historical typhoon events. The choice of the best-fitting relationship is based on visual inspection and comparison of the R^2 values and the $RMSE$ values.

Following the validation analysis in Appendix J the relationship proposed by Horikawa is selected to model the storm surge height with 18-hour prior to landfall values for wind speed and atmospheric pressure as proposed by Needham & Keim. During the simulation of the storm surge, the actual wind direction is chosen to be constant, such that θ remains constant as explained in Section 2.3.1. However, it should be noted that θ, influenced by the maximum wind direction of a typhoon, is highly sensitive. Consequently, the resulting storm surge height should be interpreted with caution as the wind direction

strongly influences the storm surge height in this relationship. This relationship could therefore lead to underestimated results for lower storm surges and overestimated results for higher storm surges or vice versa, depending on the wind direction. As this is a very preliminary research report, the relationship is assumed to simulate the storm surge height reasonably well.

To conclude, in the 1D-model, the actual wind direction is equal to the ideal wind direction found in Section 3.3.1, the atmospheric pressure follows from the relationship between 18-hour wind speed prior to landfall and atmospheric pressure found in Section 3.3.1, and the wind speed 18 hours prior to landfall follows from either the results of Method 1 in Section 3.3.1 or Method 2 in Section 3.3.3.

Peak river discharge, $Q_{r,p}$

This preliminary report proposes to determine the peak river discharge by multiplying the amount of precipitation per time unit p times the catchment area of the rivers discharging behind the selected location for a barrier. The precipitation per time unit can be derived from the cumulative precipitation divided by the duration of the period of the summed precipitation from Section 2.3.2. As a result, the precipitation is averaged over the summed period.

As a result of this simplified approach, the 1D-model does not represent the processes of precipitation, land storage, and river storage and runoff in a sophisticated manner, as a more complex hydrological model would. This simplification is likely the main source of uncertainty in the model results, as precipitation during a typhoon is expected to be a major contributor to the water level behind the barrier simulated by the 1D-model.

In the resulting 1D-model, the precipitation following from Method 1 in Section 3.3.2 and/or Method 2 in Section 3.3.3 can be used to determine the peak river discharge.

Waves, h_{wave}

Waves are generated by the typhoon-induced winds and can result in higher water levels at the shore. Whether they play a significant factor in the 1D-model for the selected location of the barrier is found through literature research. It is separately considered in the determination of dimensions and loads, as stated in 2.5.2.

2.4.3. Wind speed & precipitation combinations

The 1D-model is used to evaluate the storage capacity of the location of the selected barrier and determine the maximum water level difference between the water level behind and in front of the barrier (hydraulic load) during a typhoon. To determine the critical water levels for each objective, both the design typhoon resulting from Method 1 and Method 2 are used to determine possible combinations between wind speed and precipitation that could lead to the critical combinations.

Each combination of wind speed and precipitation per method is evaluated when the gates close at low, mid, and high tide in order to determine the influence of the tidal component on the water levels behind and in front of the barrier.

In this section the combinations per method are described for each objective.

Method 1

In Method 1, the combinations of the parameters should be chosen such that they represent the design return period of the typhoon. As Method 1 leans on the assumption that the wind speed intensity and precipitation amount during a typhoon are uncorrelated and therefore independent, the probability of a typhoon making landfall in Tokyo per year with a wind speed exceeding $w_{RT,w}$ and a cumulative

precipitation exceeding $r_{RT,p}$ can be described as:

$$P[W > w_{RT,w},\ R > r_{RT,r} \mid \text{Landfall in Tokyo}] = P[W > w_{RT,w} \mid \text{Landfall in Tokyo}] \cdot P[R > r_{RT,r} \mid \text{Landfall in Tokyo}] \tag{2.19}$$

$$\text{with } P[W > w_{RT,w} \mid \text{Landfall in Tokyo}] = \frac{1}{RT_w} \tag{2.20}$$

$$\text{with } P[R > r_{RT,r} \mid \text{Landfall in Tokyo}] = \frac{1}{RT_r} \tag{2.21}$$

Consequently, $w_{RT,w}$ and $r_{RT,r}$ follow from the resulting design values per return period for wind speed and cumulative precipitation, respectively.

Storage capacity

The combination of wind speed and precipitation of the design typhoon, leading to the determination whether the selected barrier location provides enough storage capacity, likely consists of both a high wind speed and high precipitation. When both components are relatively high, it is hypothesized that the rivers discharging behind the barrier will have a large discharge, and simultaneously there will be a large storm surge. The high water levels in front of the barrier obstruct the outflow of water accumulating behind the barrier due to the river discharge. Consequently, the return periods for wind speed and cumulative precipitation that could lead to relatively large values for both components are included.

Hydraulic load

The critical combination of wind speed and precipitation of the design typhoon, which determines the hydraulic load at the selected barrier location and is used for dimensioning the barrier, is hypothesized to consist of either very high wind speeds with low precipitation, or vice versa. When one component is extreme and the other relatively low, the resulting conditions are assumed to produce the largest difference between the water levels in front of and behind the barrier.

For example, a typhoon with very high wind speeds and negligible river discharge in the rivers discharging behind the barrier would generate a large storm surge, causing high water levels in front of the barrier while the levels behind it remain nearly unchanged. Consequently, the return periods for wind speed and cumulative precipitation that could produce the largest water level difference using Method 1 are selected.

Method 2

Method 2 describes the design typhoon with the design return period already as combinations between wind speed and cumulative precipitation as outlined in Section 2.3.3. Therefore, for each wind speed, the corresponding cumulative precipitation until landfall and from the moment of landfall can be obtained from the results after applying the methods described in Section 2.3.3.

Storage capacity

Similar to Method 1, the critical combination of wind speed and precipitation of the design typhoon, determining whether the selected barrier location provides enough storage capacity, likely consists of both high wind speed and high precipitation. Consequently, the combinations between wind speed and cumulative precipitation that could lead to relatively large values for both components are evaluated in the 1D-model.

Hydraulic load

Again, similar to Method 1, the critical combination of wind speed and precipitation of the design typhoon, which determines the hydraulic load at the selected barrier location and is used for dimensioning the barrier, is hypothesized to consist of either very high wind speeds with low precipitation, or

vice versa. When one component is extreme and the other relatively low, the resulting conditions are assumed to produce the largest difference between the water levels in front of and behind the barrier. In Method 2, the combinations are selected that include either an extreme wind speed and negligible precipitation, or vice versa, after applying the methods as outlined in Section 2.3.3.

Proxy Storm

The observed combination of storm surge height, precipitation, and river discharge during the selected proxy storm is applied as input to the one-dimensional (1D) model. The results of the model can determine whether the selected location of the barrier has enough storage capacity to withstand the selected proxy storm and what the hydraulic load would have been on the barrier during the selected proxy storm. Furthermore, it can help validate the results from the 1D-model following from the design typhoon from either Method 1 or Method 2.

Furthermore, the selected proxy storm is evaluated under the same tidal scenarios (low, mid, and high tide) as the design typhoon originating from Method 1 and Method 2. The observed tidal height at the moment of landfall of the selected proxy storm is not of interest in order to compare the results of the 1D-model of the proxy storm with the 1D-model results of the design typhoon of either Method 1 or Method 2.

2.4.4. Mathematical formulation of 1D-model

The 1D-model is constructed to evaluate the storage capacity of the barrier at the selected barrier location and determine the hydraulic load on the barrier at the selected barrier location under the design typhoon. However, these different objectives cannot be described by the same 1D-model due to simplicity assumptions. As a result, first the 1D-model is described to evaluate the storage capacity, followed by the description of the 1D-model to determine the hydraulic load.

1D-model evaluating storage capacity

The water level inside and outside of the barrier can be modeled separately. The water level behind the barrier, also referred to as the water level in the basin h_{basin}, can be described by Equation 2.22 for when the barrier is closed and opened, respectively. The water level in front of the barrier, also referred to as the water level in the bay h_{bay} can be modeled using Equation 2.23.

$$h_{\text{basin}}(t) = \begin{cases} \text{Barrier closed:} & h_{\text{tide}}(t_0) + h_{\text{r,discharge}}(t) + h_{\text{precipitation}}(t) \\ & \quad + h_{\text{SLR}} - h_{\text{r,storage}}, \quad t_0 \leq t + t_0 \leq t_{\text{open}} \\ \text{Barrier open:} & h_{\text{tide}}(t + t_0) + h_{\text{r,discharge}}(t) + h_{\text{precipitation}}(t) \\ & \quad + h_{\text{SLR}} - h_{\text{r,storage}} + \Delta h + h_{\text{surge}}(t), \quad t + t_0 \geq t_{\text{open}} \end{cases} \tag{2.22}$$

$$h_{bay}(t) = h_{\text{tide}}(t + t_0) + h_{\text{surge}}(t) + h_{\text{SLR}}, \text{ for } t + t_0 \geq t_0 \tag{2.23}$$

In Equation 2.22 and 2.23, h_{SLR} representing sea level rise determined in Section 2.4.1, $h_{r,storage}$ representing the storage capacity of the rivers discharging behind the barrier and their catchment areas determined in Section 2.4.1, and Δh describing the maximum water level increase after opening the barrier determined in Section 2.4.4, are assumed to be constant values in the 1D-model. Assuming that the river storage capacity $h_{r,storage}$ is a constant value in the model could be optimistic, as this means that the river storage will fill completely during every typhoon, whilst the basin behind the barrier will not necessarily be full at that point.

The other parameters are not constant in time and are described by separate formulas. The tide is modeled as a sinusoidal as shown in Equation 2.24, where the amplitude and phase inside and outside of the barrier are assumed to be the same. The period T_{tide} and the amplitude of the tide A_{tide} is defined in Section 2.4.1.

$$h_{\text{tide}} = A_{\text{tide}} \sin\left(\frac{2\pi}{T_{tide}} \cdot (t_0 + t)\right) \tag{2.24}$$

The Equation 2.25 models the river discharge linearly over time, where the derivation of $Q_{\text{river,discharge,t}}$ is defined in Section 2.4.1. The $Q_{\text{river,discharge,t}}$ depends on time as the cumulative precipitation before

the typhoon makes landfall differs from the cumulative precipitation during landfall as described by Section 2.3.2. As a result, the slope of $h_{basin}(t)$ is expected to change at the moment of landfall in the model.

$$h_{\text{river,discharge}}(t) = Q_{\text{river,discharge,t}} \cdot t \tag{2.25}$$

Equation 2.26 describes the precipitation that falls directly in the basin. Here the cumulative precipitation is divided by the duration of the summation period to obtain an average precipitation per time unit. The same approached is used in Section 2.4.1. $h_{\text{precipitation,t}}$ also depends on time, as the cumulative precipitation until landfall differs from the cumulative precipitation during landfall. Therefore, the slope is expected to change at the moment of landfall.

$$h_{\text{precipitation,basin}}(t) = h_{\text{precipitation,t}} \cdot t \tag{2.26}$$

The report assumes that $h_{bay}(t)$ is not influenced by precipitation in the bay directly. This assumption could lead to the 1D-model underestimating the water levels in Tokyo Bay during a typhoon.

Equation 2.27 describes the surge, which is assumed to be a constant value during the duration of the surge $\Delta t_{\text{surge duration}}$ starting at the moment of landfall. The value h_{surge} is determined in the approach used in Section 2.4.2, where the surge can be calculated for certain design return periods.

$$h_{\text{surge}}(t) = \begin{cases} 0, \text{ for } t < t_{\text{landfall}} \\ h_{\text{surge}}, \text{ for } t_{\text{landfall}} \leq t \leq t_{\text{landfall}} + \Delta t_{\text{surge duration}} \\ 0, \text{ for } t > t_{\text{landfall}} + \Delta t_{\text{surge duration}} \end{cases} \tag{2.27}$$

As shown in Equations 2.22 and 2.23, the model starts at t_0 at which point the gates are closed. This timestamp determines the water level of the basin at the start point from when the water level in the basin and the bay are modeled separately. During this time period, the typhoon makes landfall at $t_{landfall}$ from where some parameter values change, as described in the paragraphs before. The gates reopen at t_{open} when the water level in the basin becomes greater than or equal to that in the bay (Equation 2.28) such that water can flow out of the basin. From that moment, it is assumed that the water level inside the basin will adapt to the water level outside the barrier, where the water level inside the basin compared to the water level outside of the barrier cannot exceed a difference of Δh (See Equation 2.30). The gates can be closed once more when the criterion in Equation 2.28 is satisfied again. From that moment, the water level behind the barrier follows Equation 2.22, which describes the closed-barrier condition.

$$Criterion: \left\{ h_{\text{basin}} \geq h_{\text{Bay}} \text{ with } h_{\text{basin}} = h_{\text{tide}}(t_0) + h_{\text{r,discharge}}(t) + h_{\text{precipitation}}(t) + h_{\text{SLR}} - h_{\text{r,storage}} \right. \tag{2.28}$$

Water level increase in basin after opening of the barrier

The water level in the basin can still accumulate in the basin if the gates are opened, but a large river discharge remains. This is the result of the flow restriction imposed by the gates. The resistance due to the gates consists of expansion losses and boundary resistance. A head difference is needed for the outflow through the barrier, which supplies the system with enough energy to overcome the resistance experienced through the gates.

The situation can be described as follows: the barrier opens when $h_{\text{basin}} = h_{\text{Bay}}$, meaning there is no steady head difference to drive flow into the basin. Meanwhile, the basin continues to receive river and rainfall inflow Q_r, which must be balanced by the outflow Q_{out} through the barrier opening. The key requirement is that, even when the barrier is closed, the water must be able to flow out of the basin at the same rate as the inflow from the river. It is further assumed that no flow occurs as long as there is no head difference, since the resistance of the gate must be overcome by a driving energy.

This approach follows the principles outlined in 'Unsteady Flow in Open Channels' by Labeur and Battjes (Battjes & Labeur, 2017). The governing relation is Equation 2.29:

$$h_s - h_b = \frac{l}{gA_c}\frac{dQ}{dt} + W \tag{2.29}$$

where W is the head loss due to boundary resistance and expansion loss, expressed in Equation 2.30:

$$W = \Delta H_e + \Delta H_r = \frac{|U|U}{2g} + c_f \frac{l}{R}\frac{|U|U}{g} \tag{2.30}$$

In this formulation, steady flow is assumed, i.e.,

$$\frac{dQ}{dt} = 0 \tag{2.31}$$

Using Equation 2.32 as a relation for U the cross-sectionally averaged velocity,

$$U = \frac{Q}{A_c} \tag{2.32}$$

the expression for the head rise can be rewritten as Equation 2.33:

$$\Delta h = \left(\frac{1}{2g} + \frac{c_f\, l}{gR}\right)\left(\frac{Q}{A_c}\right)^2 \tag{2.33}$$

The parameters of Equation 2.30 are defined as:

- c_f is the boundary resistance coefficient $\approx$ 0.01 - 0.03, with 0.02 adopted as an average value (Battjes & Labeur, 2017),
- R = the hydraulic radius ($R = {}^{A_c}/_{P}$, with P the wetted perimeter) equal to the depth at the barrier 19.75 $[m]$,
- l is the length of the channel, here $\approx$ 200 $[m]$ assumed similar to the Hollandse IJsselkering,
- Q the discharge of the Arakawa river, which is determined for each evaluated scenario $[m^3/s]$,
- The wet cross-sectional area, A_c, is determined by only the navigational gates, assumed to give a more conservative estimation for this simplified approach, determined in Section 2.5.3, where A_c is given by:

$$\begin{aligned} A_c &= A_{\text{navigational}} \\ &= R \times P_{\text{navigational}} \\ &= 19.75\ [m] \times 350\ [m] \\ &= 6{,}912.5\ [m^2] \end{aligned} \tag{2.34}$$

Equation 2.30 results in a maximum head difference needed to overcome the energy losses, which is also the maximum water level rise in the basin $h_{basin}(t \geq t_{open})$ after the gates are opened relative to the water level outside the barrier $h_{bay}(t \geq t_{open})$ that can be expected due to the restricted outflow. The value for the maximum head difference changes per scenario as it is dependent of the amount of precipitation.

1D-model determining hydraulic load

To determine the hydraulic load, the maximum water difference between the water level behind and in front of the barrier should be found. The maximum water difference can occur under two instances. Either the water level behind the barrier largely exceeds the water level in front of the barrier, or the water level in front of the barrier largely exceeds the water level behind the barrier. This results in two different formulations of the 1D-model: a. $h_{basin,max} >> h_{bay,max}$ and b. $h_{basin,max} << h_{bay,max}$.

a. $h_{basin,max} >> h_{bay,max}$

Under this scenario, the gates are opened during the entire length of the storm surge as there is extreme river discharge in combination with a negligible storm surge. As a result, under the assumption that the tide component remains the same behind and in front of the barrier, the maximum difference in water level can be calculated using Equation 2.33 for Δh.

b. $h_{basin,max} << h_{bay,max}$

Under this scenario, the gates are closed during the entire the entire length of the storm surge as there is negligible river discharge in combination with an extreme storm surge. The 1D-model can be composed similarly to the 1D-model used to evaluate the storage capacity. The 1D-model now formulates $h_{basin}(t)$ as described by Equation 2.35 and $h_{bay}(t)$ as described by Equation 2.36.

$$h_{basin}(t) = h_{\text{tide}}(t_0) + h_{\text{SLR}}, \text{ for } t_0 \geq t + t_0 \tag{2.35}$$

$$h_{\text{Bay}}(t) = h_{\text{tide}}(t + t_0) + h_{\text{surge}}(t) + h_{\text{SLR}}, \text{ for } t + t_0 \geq t_0 \tag{2.36}$$

The difference between the 1D-model to evaluate the storage capacity and this model is that now the water level behind the barrier is not influenced by the precipitation amount and consequently river run-off. This assumption stems from the fact that the precipitation amount is assumed to be negligible and furthermore, the storage capacity can be used to obstruct much of the extra river run-off if present at all.

2.5. System design storm surge barrier

This section describes the method applied to determine the key dimensions of the potential SSB. The methodology for the system design of the SSB consists of the following steps:

1. Define the main system components and functions.
2. Identify design parameters.
3. Determine navigational requirements using design guidelines by PIANC – The World Association for Waterborne Transport Infrastructure (2014) and Ligteringen (2009).
4. Establish the main hydraulic features and dimensions of the components of the barrier
5. Identify suitable locations for each component based on hydraulic, spatial, and navigational considerations.

2.5.1. Main system components and functions

The components and the accompanying functions of the proposed SSB are inspired on the reference projects described in Section 2.1.3 and on lectures of Wüthrich (2025).

To preserve ecological connectivity and maintain uninterrupted shipping activities, the navigational gates remain in open position during normal conditions. Under extreme conditions, the gates are closed to prevent storm surge to enter the basin. During these closure periods, shipping activities are assumed to be suspended due to the extreme conditions, indicating there is no need for navigation locks.

Due to the scope of the project, only the preliminary dimensions of the gated sections for navigational and environmental purposes, and ungated sections of the barrier are presented in the following sections.

2.5.2. Design parameters

In order to determine the key dimensions of the SSB, the design parameters must be identified. The design parameters follow from the 1D-model discussed in Section 2.4 and from literature review. These parameters are the relevant water levels in the bay during high and low tide, storm surges, sea level rise, and wind speed. These are discussed in Sections 2.4.1, 2.4.2, 2.4.1 and 2.4.3, respectively. The depth of the sea bed results from the bathymetry of the location of the SSB.

The design water level with respect to T.P., DWL, at the seaward side of the barrier, hence in Tokyo Bay, is expressed by Equation 2.37.

$$DWL = HAT + SLR + SS \tag{2.37}$$

Where:

HAT	$[+m]$ $T.P.$	Highest astronomical tide
SLR	$[m]$	Sea level rise
SS	$[m]$	Storm surge

The design low water level with respect to T.P., DLWL, in the storage basin is expressed by Equation 2.38.

$$DLWL = LAT + SLR \tag{2.38}$$

Where

LAT	$[+m]$ $T.P.$	Lowest astronomical tide
SLR	$[m]$	Sea level rise

The significant wave height and peak wave period of the wind-generated waves are determined using the equation of Carter (1982), see Equation 2.39.

$$\text{If } D > 1.167 \cdot \frac{X^{0.7}}{U^{0.4}} : \begin{cases} \text{If } X < 2.32 \cdot U^2, & H_s = 0.0163 \cdot X^{0.5} \cdot U \quad \text{(fetch-limited, growing sea)} \\ & T_p = 0.566 \cdot X^{0.3} \cdot U^{0.4} \\ \text{If } X \geq 2.32 \cdot U^2, & H_s = 0.0248 \cdot U^2 \quad \text{(fetch-limited, fully developed)} \\ & T_p = 0.728 \cdot U \end{cases} \tag{2.39}$$

With U_{10} the wind speed at 10 meters above water level in $[m/s]$, X the maximum fetch length in $[km]$, and D duration of the wind in hours.

Due to the basin-like structure of Tokyo Bay, it is assumed that the waves are fetch-limited, and thus, equation 2.39 is applied. The wind speed at 10 $[m]$ above water level U_{10} in $[m/s]$ for a return period of 1/200 years is determined in Table 3.15. Due to the rotating wind direction around the eye of the typhoon, it can be assumed that the maximum fetch corresponds with a wind direction, hence wave direction, of 30° further south to the perpendicular axis to the barrier. The maximum fetch length, X in $[km]$, corresponding to this wind direction is obtained with Google Earth (Google, 2025).

Using the significant wave height, the maximum wave height is found from the correlation of Candella (2016), see Equation 2.40

$$H_{max} = 1.6 \cdot H_{m0} \tag{2.40}$$

Where $H_{m0} \approx H_s$.

The peak tidal discharge is calculated using Equation 2.41:

$$Q = \frac{\pi \cdot V}{T} \tag{2.41}$$

Where Q is the peak tidal discharge $[m^3/s]$, V is the tidal volume $\left[m^3\right]$, and T is the tidal period $[s]$. Using the storage area behind the barrier found in Section 2.4.1 and the tidal range found in Section 2.4.1, the tidal volume is obtained by direct multiplication. The tidal period is set to 6 hours.

2.5.3. Navigational requirements

The navigational openings must facilitate existing and future shipping activities. Therefore, it must be determined what minimum navigational opening width and depth is needed. This is accomplished using the maximum expected vessel size and the shipping intensity through the barrier cross-section.

Current and future shipping activities

Current and future shipping activities are determined by a literature review on shipping intensity and vessel sizes.

Navigation depth

The design depth d_{nav} is computed according to PIANC – The World Association for Waterborne Transport Infrastructure (2014):

$$d_{nav} = D_s - \zeta_{tide} + s_{max} + \zeta_m + s_s \tag{2.42}$$

With the following parameters:

d_{nav}	$[m]$	Depth of navigation channel
D_s	$[m]$	Draft of design ship
ζ_{tide}	$[m]$	Tidal elevation above reference level below which no entrance is allowed
s_{max}	$[m]$	Maximum sinkage due to squat
ζ_m	$[m]$	Vertical motion due to wave response
s_s	$[m]$	Remaining safety margin to account for trim and other things not considered or net under keel clearance

The maximum sinkage due to squat in open water conditions s_{max} is found using the following formula (Barrass, 1979):

$$s_{max}\delta = C_B \cdot \left(\frac{V^2}{100}\right) \tag{2.43}$$

With the following parameters:

$\delta = s_{max}$	$[m]$	ship squat
C_B	$[-]$	ship blockage coefficient
V	$[kn]$	Vessel speed

Lastly, since the navigational depth must be guaranteed during low water conditions as well, the tidal difference must be added to obtain the depth to the sill of the gate d_{sill}.

Navigation width

The minimum required span of the gates (W_{min}) is calculated using the following equations for one- and two-way channels, respectively (PIANC – The World Association for Waterborne Transport Infrastructure, 2014):

$$W_{min} = \left(W_{BM} + \sum W_i + W_{BR} + W_{BG}\right) \cdot W_s \tag{2.44}$$

$$W_{min} = \left(2 \cdot W_{BM} + 2 \cdot \sum W_i + W_{BR} + W_{BG} + \sum W_p\right) \cdot W_s \tag{2.45}$$

All "W-factors" are given along with the calculations in the results Section 3.5.3.

Verification of shipping intensity

Lastly, it must be verified whether the opening can meet the expected shipping intensity, without the vessels having to slow down to meet safety requirements. This is done by evaluating whether the available spacing between the vessels, measured from the fronts of both vessels, is sufficient for the vessel activities (see Equation 2.46)

$$L_{available} \geq L_{required} \tag{2.46}$$

The available distance between vessels is calculated by Equation 2.47.

$$L_{available} = \frac{\text{Service time of navigational opening per day[s]}}{\text{Number of vessels passing the opening per day [-]}} \cdot V \tag{2.47}$$

Where V is the vessel speed in $[m/s]$.

The minimum required distance from the stern of the vessel traveling in front and the bow of the craft traveling behind is $1.45 \cdot L_s$ according to Groeneveld (2002). The required vessel distance is determined by Equation 2.48.

$$L_{required} = (1.45 + 1) \cdot L_s \tag{2.48}$$

Where L_s is the length of the vessel in $[m]$.

2.5.4. Suitable locations of the barrier components

Until now, only a rough estimate of the barrier location has been determined in Section 2.2.3. To gain a clearer understanding of the surrounding infrastructure, an indicative map was created using data from Google Maps (Google, 2025). Based on spatial, hydraulic, and operational considerations, the barrier alignment was defined, as well as the barrier components.

2.6. Component design storm surge barrier

This section presents the design procedure of the different components of the SSB: navigational gates, gated flow inlets, and ungated barrier. Due to the scope of the project, a conceptual design of the navigational gate is established, and only the key dimensions of the gated flow inlet and ungated barrier are determined. The following methodology is applied:

1. Designing the navigational gate
   (a) Selecting a suitable gate type by comparing several gate types identified by Mooyaart and Jonkman (2017) by means of a MCDA;
   (b) Determining the key dimensions of the general gate components;
   (c) Defining loads acting on the gate;
   (d) Visualizing the design by a technical drawing.
2. Designing the gate for the flow inlet.
3. Designing the ungated barrier.

2.6.1. Gate design

For the gate design, proper gate types must be defined, whereafter the most promising gate type is selected by means of a MCDA. Furthermore, the dimensions of the gate are determined, and a technical drawing is established accordingly.

Gate type

Mooyaart and Jonkman (2017) summarize different gate types applied in other SSB designs. Based on the functional requirements established in Section 2.1.4 and given the requirement to enable navigation (Section 2.5.3), four gate types that can span the openings that follow from the navigational requirement are evaluated.

MCDA

The MCDA for the gates follows a similar procedure as for the barrier location in section 2.2.3. Each gate type is evaluated according to five main criteria. These criteria are:

- Ease of construction
- Required space

- Ease of maintenance
- Adaptability
- Operation time

The detailed explanation of the MCDA can be found in Appendix K

Dimensions gate

The dimensions of the flap gate are determined based on the wave elevation in the most critical loading combination, explained in Section 2.4.3, and on the height-to-width ratios of the existing Kanadevia flap gate design. It is assumed that the height-to-width ratio of the Kanadevia flap gate is applicable to other flap gate designs. The design manual by Coastal Technology Research Center (2020) is used as a reference for the current Kanadevia flap gate configuration. In addition, several rules of thumb for circular members from Hoving (2025) are applied to obtain preliminary dimensions of the flap gate components.

It is assumed that the flap gate should be high enough to prevent overtopping. This assumption is in line with the one-dimensional basin model, where the basin is only additionally filled with water originating from river discharge and precipitation. Based on the height-to-width relationship of the Kanadevia flap gate, a suitable width is estimated. This assumption is used as a first starting point. The gate is designed as a structure consisting of airtight circular tubes to ensure buoyancy. Dimensions are obtained using general design rules of thumb, while the dimensions of the substructure are assumed based on the height-to-width ratio of the Kanadevia flap gate for this stage of the analysis. The used rules of thumb are given in Equation 2.49 and 2.50 (Hoving, 2025).

$$D = 0.023 \cdot L \tag{2.49}$$

$$t = \frac{D}{25} \tag{2.50}$$

Where:

- D is the member diameter in $[m]$.
- L is the member length in $[m]$.
- t is the member thickness in $[m]$.

Loads on the gate

An overview of all loads acting on the barrier is created based on the most critical loading combination, found from the 1D-model from Section 2.4.3. This load combination ensures a maximum head difference between the water levels in the bay and the basin.

When destabilizing forces are larger than stabilizing forces, failure of the barrier occurs. Destabilizing forces are those that act to set the barrier in motion, such as wind, water, and wave pressures. Stabilizing forces act to keep the barrier at rest, such as its self-weight. For a conceptual configuration of the barrier the following loads are considered: self-weight, buoyancy, wind load, hydrostatic load, and wave load. Note that earthquake loads should be accounted for as well, but are out of the scope of this preliminary design.

Figure 2.2 presents an overview of the different loads and gives a rough idea of different water levels. The loads are calculated according to the obtained dimensions. The waves are characterized as nonlinear, accounting for steeper crests (0.55 of wave height) and broader troughs (0.45 of wave height).

For the gate height, it is assumed that this is equal to the design water depth, plus two times the crest height to account for overtopping due to gate-wave interaction.

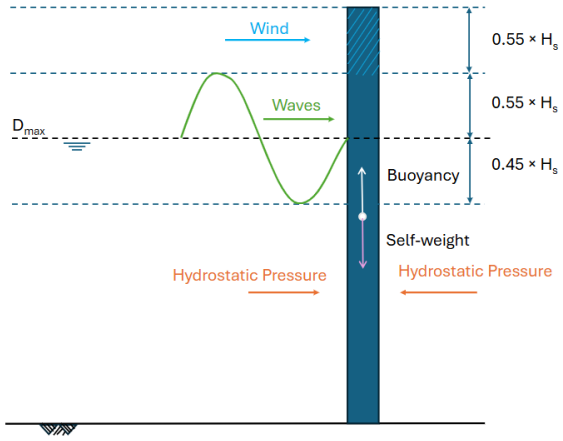

Figure 2.2: Overview of the loads on the gate.

Each load is visualized separately in Appendix E.

Wind Load

A first indication of the wind load is calculated using Equation 2.51 (Voorendt, 2022).

$$p_w = \frac{1}{2} \cdot \rho_{air} \cdot v_w^2(z) \tag{2.51}$$

Where:

- $\rho_{air} = 1.225\ [kg/m^3]$, the density of air.
- v_w is the extreme wind speed in $[m/s]$.

Figure E.1 shows a representation of a wind pressure on a structure with a length equal to the design water depth plus two times the wave crest height.

Hydrostatic Load

The hydrostatic load is found using Equation 2.52 that follows from Pascals law (Pascal, 1663):

$$p(z) = \rho_{water} \cdot g \cdot z \tag{2.52}$$

Where:

- $\rho_{water} = 1025\ [kg/m^3]$, the density of sea water.
- $g = 9.81\ [m/s^2]$, the gravitational constant.
- z, the variable coordinate in $[m]$. In Equation 2.52, the z-coordinate is zero at the water surface.

Figure E.2 presents the hydrostatic pressure on the structure. The hydrostatic pressure linearly increases with depth. Due to storm surge, waves, and precipitation, the water levels in front and behind the gate differ, and therefore, the hydrostatic pressures are different.

Equation 2.53 shows how the design water depth at the bay side of the barrier (D_{max}) is obtained.

$$D_{max} = d_{sill} + SLR + HAT + SS \tag{2.53}$$

Where:

- d_{sill} is depth of navigational gate in $[m]$.

- SLR is sea level rise in $[m]$.
- HAT is the highest astronomical tide in $[m]$.
- SS is storm surge in $[m]$.

Wave Load

The wave load is calculated using the Goda method (Peters, 2025):

$$p_1 = \alpha_1 \cdot \rho_{water} \cdot g \cdot H_d \tag{2.54}$$

$$p_2 = \frac{p_1}{cosh(2\pi \cdot \frac{h}{L_d})} \tag{2.55}$$

Where:

- $\alpha_1 = 0.6 = 0.5 \cdot \left(\frac{4\pi \frac{h}{L_d}}{sinh(4\pi \frac{h}{L_d})} \right)^2$, a coefficient in $[-]$, where:
  - h is the design water depth in [m].
  - $L_d = \frac{g \cdot T^2}{2\pi}$, the design wave length in $[m]$, where:
    - T is the wave period in $[s]$.
- $H_d = 1.8 \cdot H_s$, the design wave height in $[m]$, where:
  - H_s is the significant wave height in $[m]$.

Figure E.3 presents the wave loads on the gate. Equation 2.54 and 2.55 determine respectively the wave pressure p_1 at the design water level and p_2 at the bottom. Between the two pressures, a linear pressure profile is assumed. From the design water level up to the top of the gate, the wave pressure decreases linearly to zero over a height of $\eta = 1.8 \cdot H_s$ in $[m]$. Since η exceeds the gate height, the part of the pressure distribution above the gate cannot act on the structure. Therefore, these pressures are neglected. The calculation of the wave pressure p_3 at the top of the gate is obtained using Equation 2.56.

$$p_3 = p_1 - p_1 \cdot \frac{1.1 \cdot H_s}{\eta} \tag{2.56}$$

Self-weight

Equation 2.57 presents the equation to calculate the self-weight of any component. Equation 2.58 presents the equation to calculate the self-weight of circular members (Hoving, 2025).

$$G = \rho \cdot g \cdot V \tag{2.57}$$

$$G_{circular\,member} = \rho \cdot g \cdot \pi \cdot (D_{out} - t) \cdot t \cdot L \tag{2.58}$$

Where:

- ρ is the density of the material in $[kg/m^3$.
- V is the volume of the material in $[m^3]$.
- D_{out} is the outer diameter of the member in $[m]$.
- t is the wall thickness of the member in $[m]$.
- L is the length of the member in $[m]$.

Buoyancy

The buoyancy of any component is calculated using the Equation 2.59. Equation 2.60 is used to calculate the buoyancy of circular members (Hoving, 2025).

$$V_b = \rho_{water} \cdot V \cdot g \tag{2.59}$$

$$V_b = \rho_{water} \cdot g \cdot \pi \cdot L \cdot 0.25 \cdot D_{out}^2 \tag{2.60}$$

All Loads

Figure 2.3 shows a combination of the wind, hydrostatic, wave loads, self-weight, and buoyancy force acting on the gate.

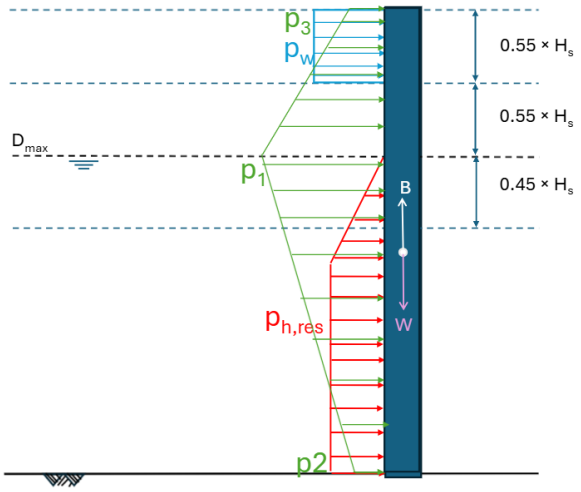

Figure 2.3: All loads on the gate.

2.6.2. Flow inlets

For this preliminary design, the gates used in the flow inlets are chosen to be the same type as the gate used for the navigational opening. An additional benefit when using one gate type over the whole barrier is that all gates operate in the same manner.
To dimension the flow gates, only the cross-sectional area is determined, and this follows from the approach described by Mooyaart et al. (2014). This formula determines the required cross-sectional area to maintain sufficient flow velocities through the barrier gates, to allow vessels to maintain their maximum velocities, as shown in Equation 2.61.

$$A = \frac{Q_{\text{tide}}}{U_{\text{max}}} \tag{2.61}$$

In this approach, A is the required cross-sectional area for both the navigational gates and flow gates in $[m^2]$, U_{max} is the maximum allowable velocity for vessel passage and is set to 1.5 $[m/s]$ (Mooyaart et al., 2014) and the peak tidal discharge Q_{tide} in $[m^3/s]$ is determined in Section 2.5.2. The cross-sectional area of the navigational gates are subtracted, and the remaining required area is used to determine the required length of flow inlets. In this approach, it is assumed that the barrier has no additional effects on the tidal amplitude, which is a simplification of reality (Du et al., 2016), (Ralston, 2022).

2.6.3. Ungated barrier

The selection of the ungated SSB type is based on several key design considerations:

- The structure must enable secondary functions;

- The bathymetry of the chosen location shows a maximum depth of 18 $[m]$ and an average depth of 12 $[m]$ (see Section 3.2.1), making dry construction using cofferdams impractical. Therefore, materials such as clay should be avoided. Besides, the required volume of material for constructing a sloping barrier, such as an embankment, increases quadratic with depth, leading to high costs (Gedda et al., 2019).
- The seismicity of Tokyo Bay makes sand applications undesirable due to risk of liquefaction.
- Japan is experienced with caisson-based hydraulic structures (Tanimoto, 1994), motivating the selection of a caisson-type ungated barrier.

Taking this into account, it is decided to implement a caisson in the design. To reduce crest elevation requirements and increase structural resilience for secondary functions, an armour unit body is included in front of the caisson. This results in a horizontal composite caisson which is further dimensioned using the methodology in the next sections.

Armour unit body design

The armour unit body consists of an armour layer, filter layers, and a permeable core. This report only focuses on its external geometry.

Crest level

The required crest level of the rubble mound armour body and the caisson can be calculated using Equation 2.62.

$$h_{crest} = DWL + R_c \tag{2.62}$$

where:

DWL	$[+\ m]\ T.P.$	Design water level with respect to T.P.
R_c	$[m]$	Minimum required freeboard height

The required freeboard height is determined using EurOtop (2018). The applicable equation for rubble mound slopes is shown in Equation 2.63.

$$R_C = \left[-\ln \left(\frac{q}{0.1036 \cdot \sqrt{g \cdot H_{m0}^3}} \right) \right]^{1/1.3} \cdot \frac{H_{m0} \cdot \gamma_f \cdot \gamma_\beta}{1.35} \tag{2.63}$$

With the oblique wave influence factor:

$$\gamma_\beta = 1 - 0.0063 * |\beta| \tag{2.64}$$

where:

R_c	$[m]$	Minimum required freeboard height
q	$[m^3/s/m]$	Critical overtopping discharge
g	$[m/s^2]$	Gravitational acceleration (= 9.81)
$H_{m0} \approx H_S$	$[m]$	Significant wave height at the toe of the structure
γ_f	[-]	Influence factor for roughness elements on the slope (EurOtop, 2018)
γ_β	[-]	Influence factor for oblique wave attack
β	$[^o]$	Angle of wave attack

Since secondary functions are wished to be incorporated into the design of the SSB, it is assumed that people will be present near the crest, and a clear view of the sea is desired. Therefore, according to the EurOtop (2018) the maximum allowed overtopping discharge is 0.3 $[l/s/m]$ for a significant wave height H_{m0} of 3 $[m]$. The manual does not provide discharge values for larger significant wave heights. Thus, it is assumed that this discharge is applicable to the SSB for Tokyo Bay.

A single rock armour layer and a smooth slope (no berm) of 1:1.5 is chosen, which results in a roughness factor γ_f of 0.45 for a permeable core (EurOtop, 2018). Due to the caisson behind, it is assumed that the crest freeboard height is equal to the armour freeboard height.

The angle of wave attack, β, is discussed in section 2.5.2.

For construction purposes, the required crest level is rounded up to an integer.

Base bidth of armour unit body
The base width of the armour unit body B_{aub} is determined by Equation 2.65:

$$B_{aub} = (h_{crest} + d_{sb}) \cdot \arctan(1/1.5) + B_{crest} \tag{2.65}$$

A characteristic stone size D_{n50} of 1.5 $[m]$ is assumed. The crest width of the armour unit B_{crest} is equal to $3 \cdot D_{n50}$.

Caisson design

The dimensions for the caisson follow from horizontal, rotational, and vertical stability (see Equation 2.66) under the critical load case of DWL at bay side and DLWL at basin side. The rubble mound breakwater in front of the caisson is assumed to dissipate all wave energy. Therefore, the caisson is assumed to only be subjected to hydrostatic loads and uplift load, see Figure 2.4.

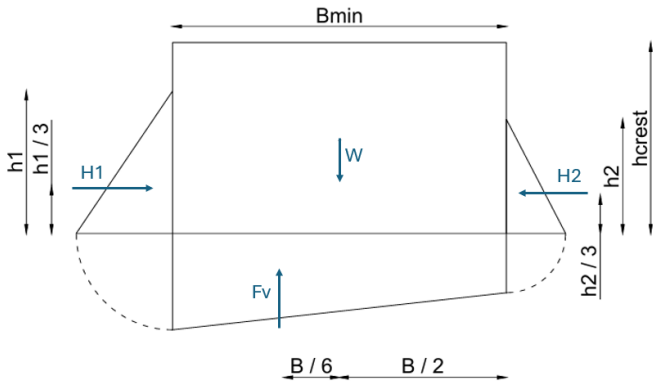

Figure 2.4: Loads on caisson.

$$\sum H = 0 \quad \sum V = 0 \quad \sum M = 0. \tag{2.66}$$

Horizontal stability

$$\frac{\sum H}{\sum V} \leq f \tag{2.67}$$

Where f is the friction factor that accounts for friction between the caisson and the underlayer. It is obtained from of Engineers (1992) while assuming that the underlayer consists of "clean fine sand, silty, or clayey fine to medium sand", hence f is 0.45.

The resultant of the horizontal forces $\sum H$ is the difference between the hydrostatic loads at each side of the caisson. The resultant of the vertical forces $\sum V$ follows from the self-weight of the caisson W and uplift pressure underneath the caisson F_v, see Figure 2.4.

$$\sum H = H_1 - H_2 = \frac{1}{2} \cdot h_1^2 \cdot \rho_w \cdot g - \frac{1}{2} \cdot h_2^2 \cdot \rho_w \cdot g \tag{2.68}$$

$$\sum V = W - F_v = \rho_c \cdot g \cdot B_{min,caisson} \cdot h_{crest} - \rho_w \cdot g \cdot (h_2 + \frac{1}{2} \cdot (h_1 - h_2)) \cdot B_{min,caisson} \tag{2.69}$$

Rotational stability

$$\frac{\sum M}{\sum V} \leq \frac{B}{6} \tag{2.70}$$

The resultant of the moments is evaluated in the middle of the caisson.

$$\sum M = M_{H1} - M_{H2} + M_{Fv} = \frac{h_1}{3} \cdot H_1 - \frac{h_2}{2} \cdot H_2 + \frac{B_{min,caisson}}{6} \cdot F_v \tag{2.71}$$

Vertical stability
The bearing capacity of the soil, p'_{max}, must be able to resist the acting loads, see Equation 2.72

$$\sigma_{max} = \frac{\sum V}{L \cdot B} - \frac{\sum M}{\frac{1}{6} \cdot L \cdot B} < p'_{max} \tag{2.72}$$

Again, the resultant from the moments is evaluated at the center of the caisson base. The length of the caisson L is assumed to be 1. A bearing capacity p'_{max} of 225.000 $[N/m^2]$ is chosen for the bearing capacity, close to the lower boundary for medium dense sand and gravel, and in the middle of the boundaries for medium dense sand (Spreadsheets, 2025). A mass density of 2400 $[kg/m^3]$ is used for the concrete caisson, ρ_c and of 1025 $[kg/m^3]$ for salt water ρ_w.

2.7. Design overview and adaptation

In this section, the methodology for the exploration of structural design possibilities for the SSB in Tokyo is described. First, an overview of the proposed SSB design and its principal dimensions is presented. Next, opportunities to integrate secondary functions within the design are discussed. Finally, the adaptability of the proposed concept is assessed in relation to climate-change-driven uncertainties, as well as other future-oriented considerations.

2.7.1. Design overview

All determined dimensions of the system and system components are combined for an overview. A figure is produced to visualize the design. If necessary additional assumptions are made.

2.7.2. Secondary functions

Potential secondary functions of the SSB are proposed to address functional requirements and specifically stakeholder ambitions. Drawing inspiration from similar projects and incorporating emerging technologies, these concepts illustrate how the storm surge barrier could serve not only as a protective structure but also as a multifunctional element within the urban and coastal environment.

2.7.3. Adaptation

Due to uncertainties associated with climate change, exploratory solutions are proposed to make sure that the structure can be adapted to future climate conditions or changing functional requirements resulting in a modular barrier design.

3

Results

This chapter presents the results obtained from the applied methodology, highlighting the key findings and outcomes of the project.

In Section 3.1, the results of the boundary condition analysis are presented, including an environmental analysis, stakeholder analysis, and a study of reference projects. At the end, the resulting functional requirements following the boundary condition analysis are presented. Section 3.2 shows the MCDA procedure and resulting barrier location. Additionally, the cost-property value analysis is presented, used to validate the outcomes of the MCDA.

Afterwards, the resulting design typhoon following either Method 1 or Method 2 for the Tokyo Bay area is presented in Section 3.3. Here, the first treats storm surge and precipitation independently, while the second considers them jointly by fitting a joint probability distribution. Since the design typhoon has been defined, the resulting 1D-model is presented in Section 3.4, including the boundary conditions, typhoon-related parameters, and the resulting critical water level behind and in front of the barrier following different combinations of typhoon parameters derived from the design typhoon of either Method 1 or Method 2 addressing either the storage capacity and the maximum hydraulic load on the barrier. Consequently, the critical combinations of typhoon parameters of the design typhoon following either Method 1 or Method 2 are presented per objective of the 1D-model.

Lastly, the resulting design of the system and the design of the key structural components of the SSB are presented in Section 3.5, 3.6, and 3.7. The designed components form the basis of the overall preliminary design. Furthermore, a more detailed design of the gates is presented.

3.1. Boundary conditions analysis

This section presents the results obtained from the boundary condition analysis.

3.1.1. Environmental analysis

This subsection presents the results obtained in the environmental analysis.

Geology

Figure 3.1 presents the generated contour map of the bathymetry. It indicates that the southern part of the bay reaches great depths, up to around 100 meters, while the northern part is relatively shallow, facilitating more favorable conditions for the construction of a SSB.

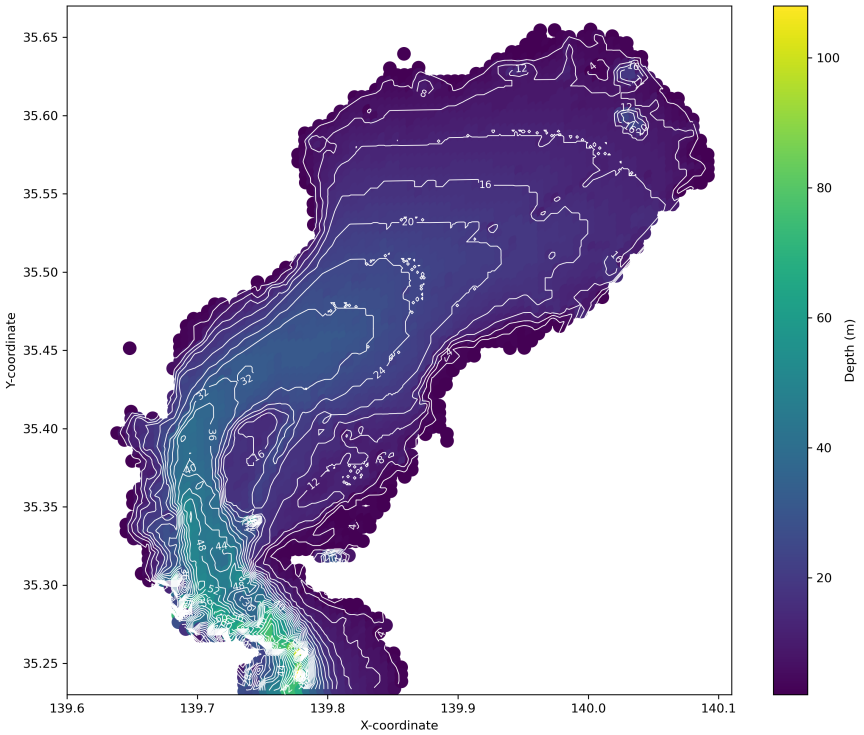

Figure 3.1: Contour Map Tokyo Bay (Japan Oceanographic Data Center, n.d.).

Based on the elevation map obtained from (Tokyo Metropolitan Government, 2025b), the zones below sea level are identified, which are mainly located along the shorelines of Tokyo Bay. Along the coasts of Chiba and Kanagawa, elevation increases rapidly toward the inland. In the delta region of Tokyo, located in the northern part of Tokyo Bay, the low-lying areas extend further inland along the rivers.

Based on the MSc thesis by Fuentes, 2014 and Tian, 2014 it is found that a large part of the bay consists mainly of mud, while sand is more dominantly found near the coastlines. At the entrance of the bay, a greater variety of sand types is present. Sand generally has a higher stiffness and shear strength than mud, making it more effective at transmitting loads to the underlying subsoil, and thus, a favorable construction site. Construction on mud would require additional measures to increase the soil strength.

Furthermore, based on available data, the Tokyo area is classified as a high seismic hazard region (ThinkHazard!, 2025). This classification indicates that there is more than a 30% chance of a potentially damaging earthquake occurring in the next 30 years (Stein et al., 2006). For severe shaking, a peak ground acceleration of 0.9 $[g]$ is expected (Stein et al., 2006). These findings indicate that the SSB must be designed to withstand significant dynamic forces resulting from seismic activity, in accordance with the Building Standard Law of Japan (Kuramoto, 2006). However, due to the project's scope, a preliminary design, no dynamic design verification is performed, and seismic effects are excluded from the design.

Ecology

Tokyo Bay is a dynamic estuarine ecosystem shaped by the inflow of freshwater from rivers and the mixing with saline water from the sea. The estuarine and coastal zones serve as nursery grounds for various fish species, where juveniles grow in the shallow, brackish waters before migrating offshore (Kasai et al., 2019). Migration between rivers and the bay highlights the strong ecological connectivity of the system, particularly for species that depend on both environments during their life cycle (Kasai et al., 2018). Urban development and intensive shipping activities have caused water pollution and seasonal reductions in dissolved oxygen levels. Living organisms in the water column and on tidal flats contribute to the natural purification of the bay (*Aquatic Creatures in Tokyo Bay*, 2015). Figure 3.2

presents the main ecological hubs identified within Tokyo Bay.

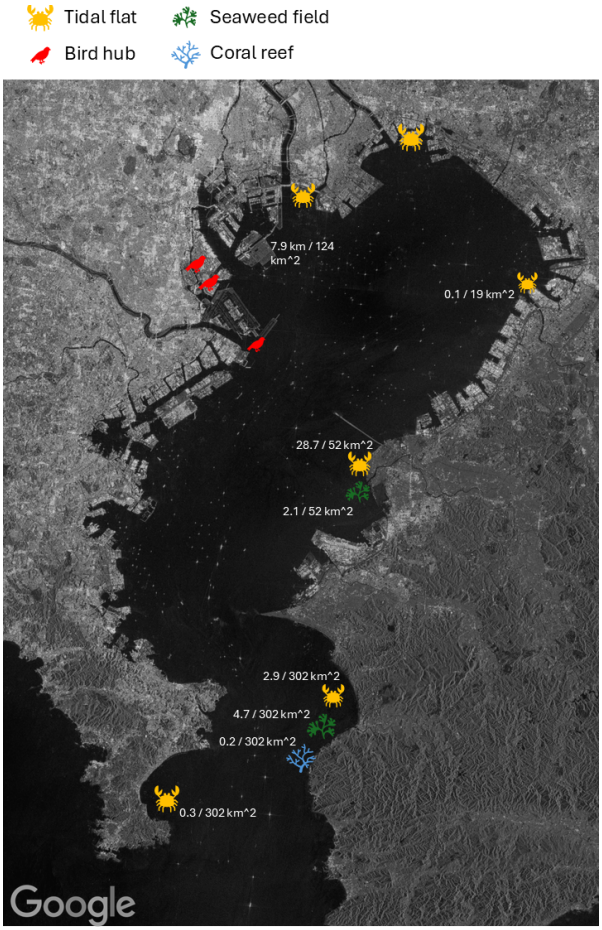

Figure 3.2: Ecological hubs in Tokyo Bay (Ministry of the Environment, Government of Japan, 2025).

Economics

Ports

The Tokyo metropolitan area encompasses six major ports: Tokyo, Kawasaki, Yokohama, Yokosuka, Chiba, and Kisarazu. Together, they generate approximately 200 trillion yen, about 38% of Japan's GDP, and handle around 7 million TEU of foreign trade annually. The region, with about 44 million inhabitants, forms the nation's economic core (Yamamoto, 2019). Therefore, the ports represent valuable assets that should be protected against flooding.

Shipping industry

Around 500 vessels transit the bay daily (Tokyo Bay Waterway Office, 2015). Tokyo Port currently accommodates ships up to 50,000 d.w.t. (15 $[m]$ draft, undefined length), with plans to increase capacity to 150,000 d.w.t. (16 $[m]$ draft, 400 $[m]$ length) (Bureau of Port and Harbor, Tokyo Metropolitan Government, 2023; OneOcean Group, n.d.-a; Tokyo Port Terminal Corporation, 2024). Kawasaki Port handles vessels up to 150 $[m]$ in length , Yokohama up to 264,000 d.w.t. (17 – 18 $[m]$ draft) (OneOcean Group, n.d.-b), and Chiba up to 314,000 d.w.t. (19 $[m]$ draft) (OneOcean Group, n.d.-c). For determining the width of the navigational opening, the governing ship size of the port behind the barrier is used.

Airport

Haneda Airport, situated within Tokyo Port, serves as a critical hub in Japan's national transportation network. Following the expansion of international flights in 2020, it has generated an estimated annual economic ripple effect of 650.3 billion yen (Ministry of Land, Infrastructure, Transport and Tourism, 2020). This highlights the airport's vital role not only in passenger transport but also in sustaining economic activity, making its protection by a SSB or other means from coastal hazards essential for maintaining national connectivity and resilience. (Ministry of Land, Infrastructure, Transport and Tourism, 2020).

3.1.2. Stakeholder analysis

This section presents the findings of the stakeholder analysis.

Tokyo Metropolitan Government

The Tokyo Metropolitan Government aims to enhance waterfront spaces and develop attractive urban areas while maintaining effective flood protection for the hinterland at minimal cost (Manning, 2024). Tokyo Metropolitan Government launched the Tokyo Resilience Project in 2022, as mentioned in 1.1, with a budget of ¥7 trillion ($50 billion) (Inoue, 2024), which aims to increase the safety and security of the city from key disaster risks, including storm and flood, major earthquakes, ash from volcanic eruptions, disruption of power supply and communication services, and spread of a new infectious disease. Flood control measures consist of the development of river revetments and regulating reservoirs to prevent river flooding and the strengthening of sewer system facilities to be more water-resistant. Storm surge measures, as a response to 60 $[cm]$ sea level rise consists of the raising of sea walls and river revetments and using AI to help control floodgates more effectively (Tokyo Metropolitan Government, 2025a). In this 50 billion dollar plan, there is yet no space for a SSB. Consequently, the proposed barrier must demonstrate clear cost-effectiveness to gain institutional support. Furthermore, the inclusion of secondary functions that contribute to urban and social value could increase the likelihood of governmental endorsement.

National government

The national government's objectives are guided by the *Fundamental Plan for National Resilience*, which aims to: prevent loss of life, ensure continuity of essential social and economic functions, enable prompt recovery and reconstruction, and promote integrated public–private cooperation. The plan emphasizes strengthening infrastructure and early warning systems (Cabinet Secretariat, Government of Japan, 2018; Kato-sensei, 2025). Accordingly, the SSB should maintain uninterrupted economic activity, protect as many people as possible, and remain feasible from a construction and implementation perspective.

Residents

Residents' main concerns are assumed to include safety from flooding and tsunamis, environmental protection, and maintaining the local quality of life. It is assumed that residents support measures that protect the ecosystem and minimize construction-related disruption, while expecting transparent communication on progress, access limitations, and noise impacts.

Ports

The ports of Tokyo, Kawasaki, and Yokohama likely want to minimal disruptions during both construction and operation. They also seek to reduce repair costs and downtime following extreme events such as storm surges or tsunamis. To minimize port development disruptions, this preliminary design should incorporate larger vessel designs and evolving shipping demands to ensure future-proof port access.

Environmental protection agencies

Organizations like the Yasu-higata nature observation center advocate for the preservation of ecological areas such as Yatsu-higata and Sanbanze tidal flats, which are vital habitats for migratory birds and marine life (Kato-sensei, 2025; "Profile of Yatsu Higata", 2025). Maintaining ecological connectivity between rivers and the bay is essential for fish species that depend on both environments during their life cycle (Kasai et al., 2018, 2019; Ministry of the Environment, Government of Japan, 2025).

Fishermen
Fishing remains culturally and economically significant in Tokyo Bay, closely linked to traditional Edo-style cuisine. Fishermen and local communities advocate for the preservation of fishing grounds and access to sustainable marine resources (Kato-sensei, 2025; Ocean Outcomes, 2025; Statistics Bureau of Japan, 2020).

Construction companies
Construction firms likely prioritize the feasibility, safety, and efficiency of construction. It is assumed that the concerns are about budget adherence, schedule reliability, and manageable technical requirements. Unrealistic design demands could increase cost and safety risks, while maintenance requirements represent a long-term interest for the industry.

3.1.3. Study of reference projects
This section presents five hydraulic structures that could serve as an example for structural elements of the potential SSB for the Tokyo Bay Area.

St. Petersburg storm surge barrier
The St. Petersburg storm surge barrier is characterized by a total span of 25.4 $[km]$ and combines multiple functional elements, including embankment dams, six sluice complexes, and two navigation channels (200 $[m]$ and 110 $[m]$ wide). The system also integrates a highway, a tunnel beneath the widest channel, and a lift bridge over the smaller one. The main navigation channel accommodates ships up to 100,000 d.w.t., with a depth of 16 $[m]$. Two sector gates, each 110 $[m]$ wide and 23.5 $[m]$ high, close the channel during storm surge conditions(Hunter, 2012).

Key takeaways for the Tokyo Bay context include:

- Multiple navigation channels improved traffic allocation;
- Sluice complexes ensured controlled tidal exchange and river outflow;
- Integration between flood forecasting, early warning, and operational systems was emphasized;
- Continuous navigation and river discharge were maintained during construction.

MOSE, Venice storm surge barrier
The MOSE barrier in Venice spans 1.6 $[km]$, with sill levels at 10.7 $[m]$. It includes three 400 $[m]$-wide navigation openings closed by flap gates and a 360 $[m]$-wide regulated opening for tidal exchange (Mooyaart & Jonkman, 2017). Umgiesser (2020) highlights the importance of accounting for barrier closure time and its projected increase due to sea-level rise. The MOSE barrier serves as an example of gates with a large span width and relatively fast closing time.

Eastern Scheldt barrier
The Eastern Scheldt barrier extends 9 $[km]$ and includes one navigation lock and 62 openings with a 42 $[m]$ width and 7.6 $[m]$ depth. Vertical lift gates are used to close the openings (Mooyaart & Jonkman, 2017). Smaal and Nienhuis (1992) emphasizes the barrier's impact on the bay's morphological and ecological equilibrium, suggesting that such effects should be carefully assessed in advance. The Eastern Scheldt barrier demonstrates that the construction of a SSB can significantly affect the morphological and ecological environment behind it.

Dutch closure dam
The Dutch closure dam (Afsluitdijk) is a 32 $[km]$ hydraulic structure separating the saline Wadden Sea from the freshwater IJsselmeer. Constructed over 90 years ago, it provides flood protection, freshwater storage, ecological value, and transport connectivity, and is recognized as cultural heritage (Rijkswaterstaat, 2025c). Recent upgrades (in 2024) include six fish-friendly pumps with a total discharge capacity of 275 $[m^3/s]$, enabling drainage regardless of sea-side water levels (Rijkswaterstaat, 2024). This structure could serve as an example for large span barriers, secondary functions and the incorporation of pumps.

Hartel barrier

The Hartel Canal barrier was constructed to combine navigation and flood protection between Rotterdam and the hinterland. It includes two vertical lift gates (98.0 [m] and 49.3 [m] wide) designed to withstand a 1/10,000-year storm surge with a 5.5 [m] head difference. The upper 3.5 [m] of the structure allows overtopping to prevent excessive river levels during extreme conditions (Daniel & Leendertz, 1994). Similarly, river discharge may be a limiting factor for the feasibility and effectiveness of a SSB in Tokyo Bay, making the Hartel Canal barrier a relevant reference case.

3.1.4. Functional requirements

This subsection presents the functional requirements that serve as the basis for further design considerations. They are defined as follows:

- A design life of 150 years;
- Protection of the Tokyo Bay area against the extreme event of heavy precipitation and storm surge due to a typhoon with a return period of 200 years
- Facilitation of storage capacity behind the barrier to accommodate river inflows.
- Adaptability to future climate change scenarios and associated uncertainties;
- Addition of value for Tokyo Metropolitan Area through secondary functions;
- Provision of navigational access for existing and future shipping activities;
- Minimization of ecological and sedimentation impacts by maintaining adequate flow exchange through the inlets;
- Preservation of the remaining natural tidal flats.
- Incorporation of sufficient redundancy to ensure operational safety in case of component failure;

3.2. Location

This section presents the results from the location analysis.

3.2.1. Possible locations

Eight locations are selected as potential alignments for the barrier, as shown in Figure 3.3. The information presented in Section 2.1 forms the basis for this evaluation.

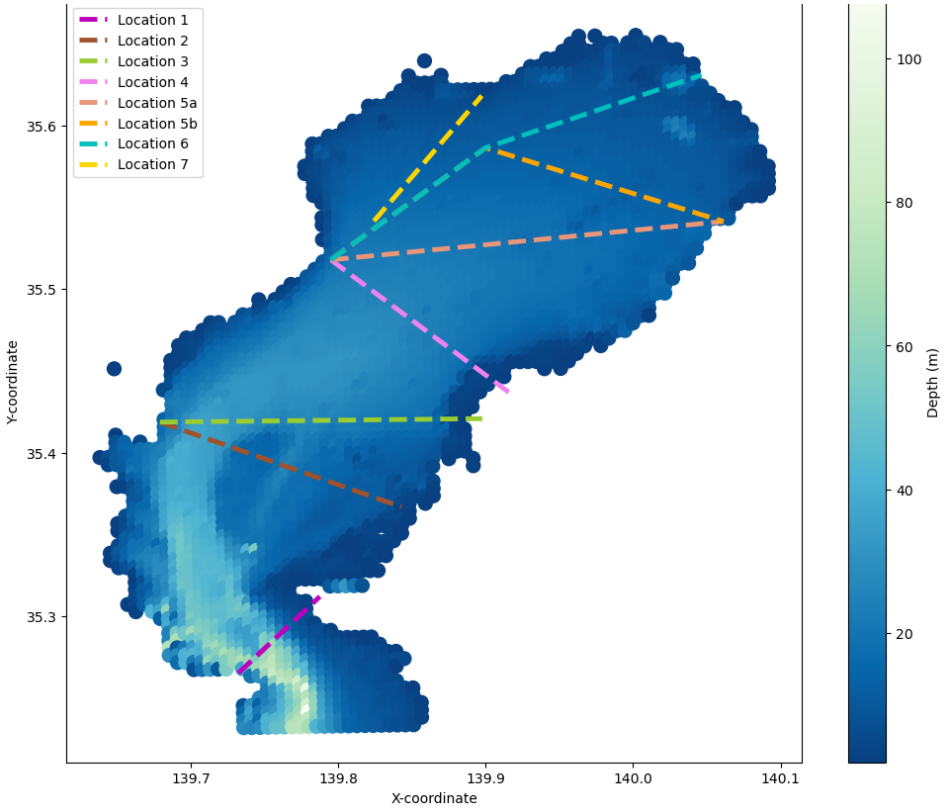

Figure 3.3: Possible locations of the placement of the SSB.

The key characteristics of each location are summarized below:

- **Location 1:** Shortest span possible. Between Yokosuka and Cape Futtsu; a short span; a large depth; protects the entire Tokyo Bay area.
- **Location 2:** Protecting the four main ports (Yokohama, Chiba, Kawasaki, Tokyo). Most of the low-lying areas are protected with the shallowest bathymetry possible.
- **Location 3:** Protecting the four main ports while avoiding interference with the tidal flat at Kuzuma. However, passes through seaweed fields; longer span and shallower bathymetry compared to Location 2.
- **Location 4:** Protection of a relatively large low-lying area with a short span. Aligns with the Aqua Line; presents structural challenges; relatively small span while protecting large parts of Kawasaki, Tokyo, Chiba, and major power plants.
- **Location 5a:** More focused on effectively protecting the residential area. Relatively shallow; large span; protects large areas of Kawasaki, Tokyo, and Chiba.
- **Location 5b:** Similar to 5a but avoids deeper sections and might allow for other secondary functions. Larger span.
- **Location 6:** Proposed in the conference by Tsuchiya (2024); large span; shallow; close to Tokyo, therefore potentially offering secondary functions for residents.
- **Location 7:** Short span and protection of the most vulnerable area only. Very shallow; may experience backwater accumulation due to river discharge; additional measures are needed to safeguard Haneda Airport and elevations in the Edo River due to storm surge.

Figure F.1 in Appendix F presents the bathymetry profiles of all locations, and Table 3.1 summarizes their main geometric properties.

Table 3.1: Characteristics of bathymetry of locations.

Location	**1**	**2**	**3a**	**4**	**5a**	**5b**	**6**	**7**
Average depth [m]	30	20	23	19	18	15	13	12
Maximum depth [m]	63	37	35	27	22	20	20	18
Total span [m]	8050	19080	24300	16130	29700	32530	30930	11770
Wet area [m^2]	242750	377070	552000	311585	543800	474770	406400	141725

3.2.2. Conceptual verification

Locations 1, 2, and 3 have maximum depths that exceed the limit set in Section 2.2.2, and therefore, are excluded from further consideration due to cost, risk, and feasibility concerns.

3.2.3. MCDA

In this section, the results are shown of the proposed method in Section 2.2.3 to determine the most promising location that would align as much as possible with the likely interests of the various identified stakeholders and to meet the requirements determined in the boundary conditions (Section 2.1).

In Section 2.2.3, first, the performance scoring per proposed criterion is evaluated and given a qualitative score. This is followed by showing the resulting weights. Consequently, the final MCDA results are shown by multiplying the weights and the qualitative scores per criterion.

Criteria

The qualitative scores per criterion per location are determined in this section. The criteria include: Costs, Protectiveness (Residential area, Port area and Ecological habitats), Accessibility, and Technical feasibility.

Costs

To qualitatively express the performance of all locations, the cross-sectional area of location 4 is assumed to be moderate (0), as it has the median value. All other locations are scored with respect to this median. As shown in Table 3.2, Location 7 obtains the highest qualitative score thanks to the lower wet cross-sectional area required and therefore lower associated costs.

Table 3.2: Qualitative scoring of the costs using the performance scores of each location on the wet cross-sectional area required. The wet cross-sectional area estimates per location originate from Table 3.1.

Location	4	5a	5b	6	7	Ref (Sum)
Wet area [m^2]	311585	543800	474770	406400	141725	1878280
% Wet Area	16.6	29.0	25.3	21.6	7.5	100
Qualitative score	0	−−	−−	-	++	*n.a.*

Protectiveness

Residential Area

Figure 3.4 shows the additional protected area for each location. The protected areas above 90 %, 80 % and 70 % are scored respectively with '++', '+' and '0'.

Figure 3.4: Potential flood area, adapted from Google Earth (Google, 2025).

Table 3.3: Qualitative scoring of the protected residential area using the performance scores of each location on the protected residential area in comparison to the maximum protected residential area by a location (here Location 4)

Location	4	5a	5b	6	7	Ref
Residential area [km^2]	565	525	525	485	435	565
% *Protected residential area*	100	93	93	86	77	100
Qualitative score	++	++	++	+	0	*n.a.*

Port area

The protected port areas for the different barrier locations can be found in Figure 3.5, in which it can be seen that out of the 5 selected locations, Location 4 protects the largest port area. Based on this, the scores are given as shown in Table 3.4, Location 4 is given the highest score (++), whereas Location 7 protects only a part of Tokyo Port and therefore receives the lowest score (-).

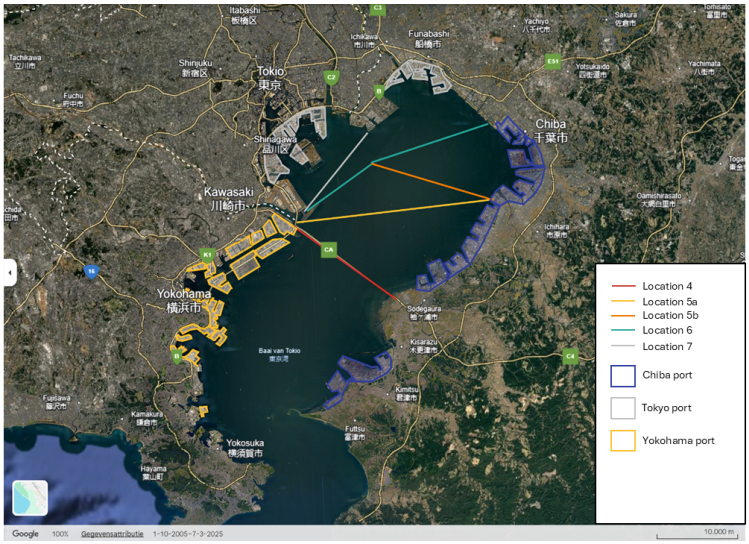

Figure 3.5: Port areas surrounding Tokyo Bay and Location barriers, adapted from Google Earth.

Table 3.4: Qualitative scoring of the protected port area using the performance scores of each location on the protected port area in comparison to the **maximum protected port area**.

Location	4	5a	5b	6	7	Ref
Port area [km^2]	80	58	58	31	20	138
% *Protected port area*	58	42	42	22	15	100
Qualitative score	++	+	+	0	-	*n.a.*

Ecological habitats

In addition to the performance scores following Equation D.4, the following considerations were used to assign the final qualitative scores visible in Table 3.5. Location 4 has the largest basin and thus affects a large ecological area. Therefore it receives a score of $--$. Location 5a and b have a much smaller storage capacity, however affect the same amount of tidal flats as Location 4 (see Figure 3.2). Therefore, they are assigned a score of $-$. Location 6 affects 1 tidal flat less (0), and 7 one less than 6 (+).

Table 3.5: Qualitative scoring of the affected ecological habitats using the performance scores of each location on total storage area in comparison to the total surface area of Tokyo Bay estimated with Google Earth (Google, 2025).

Location	4	5a	5b	6	7	Ref
Storage area [km^2]	495	345	315	155	80	1142
% $Affected\ ecological\ area$	43.3	30.2	27.6	13.6	7.0	100
Qualitative score	$--$	-	-	0	+	*n.a.*

Accessibility

Table 3.6 shows the storage capacity of each potential barrier location and their performance score obtained with Equation D.5. In addition to the performance scores in Table 3.6, locations 4, 5a, and 5b divide major fishing zones and are rated $--$, $-$ and $-$ respectively. Location 7 does not seem to intervene to much with the fishing routes (+). Consequently, location 6 receives a neutral (0) score.

Table 3.6: Qualitative scoring of the accessibility for fishing activities using the performance scores of each location on total storage area in comparison to the total surface area of Tokyo Bay estimated with Google Earth (Google, 2025).

Location	4	5a	5b	6	7	Ref
Storage area [km^2]	495	345	315	155	80	1142
% $Accessible\ fishing\ area$	43.3	30.2	27.6	13.6	7.0	100
Qualitative score	$--$	-	-	0	+	*n.a.*

Technical feasibility

In correspondence with Table 3.1, the locations 4, 5a, 5b, 6 and 7 score −−, −, +, +, ++ respectively as visible in Table 3.7, based on the maximum depth associated with each location. According to Table 3.7, Location 7 obtains the highest score thanks to its shallow depth relative to the other locations.

Table 3.7: Qualitative scoring of the technical feasibility using the performance scores of each location on the maximum depth at their designated location. The maximum depth estimates originate from Table 3.1.

Location	4	5a	5b	6	7	Ref (Sum)
Average depth [m]	19	18	15	13	12	*n.a.*
Qualitative score	−−	-	+	+	++	*n.a.*

Finally, an overview of all qualitative scores per criterion for each location is shown in Table 3.8.

Table 3.8: Qualitative assessment of criteria across possible locations.

Criteria	**4**	**5a**	**5b**	**6**	**7**
Wet cross sectional area	0	−−	−−	-	++
Residential area	++	++	++	+	0
Port area	++	+	+	0	-
Ecological habitats	−−	-	-	0	+
Obstruction of fishing grounds	−−	-	-	0	+
Maximum depth	−−	-	+	+	++

Weights

The results of the pairwise comparison, as explained in Section 2.2.3 are shown in Tables 3.9 and 3.10. Tables 3.9 and 3.10 present the final weights for all criteria used in the MCDA. These weights reflect the relative importance of each criterion, ensuring that both economic and social considerations are properly balanced with ecological and technical aspects. From the tables, it becomes clear that protectiveness and cost are the most important criteria to be taken into account.

Table 3.9: Pairwise comparison and derived weights for main criteria.

Criteria	**Cost**	**Protectiveness**	**Accessibility**	**Technical Feasibility**	**Total**	**Double**	**Weights**
Cost	x	0	1	1	2	4	0.31
Protectiveness	1	x	1	1	3	6	0.46
Accessibility	0	0	x	0	0	1	0.08
Technical feasibility	0	0	1	x	1	2	0.15
						Total	1.00

Table 3.10: Pairwise comparison and derived weights for subcriteria protection.

Subcriteria	**Residential area**	**Port area**	**Ecological habitats**	**Total**	**Double**	**Weights**	**Subweights**	
Residential area	x	1	1	2	4	0.57	0.26	
Port area	0	x	1	1	2	0.29	0.13	
Ecological habitats	0	0	x	0	1	0.14	0.07	
					Total	1.00	0.46	

Final MCDA results

Table 3.11: The table shows the final result of the MCDA combining the qualitative scores per criterion with their associated weight for each location.

Criteria	4		5a		5b		6		7	
	S	S*W	S	S*W	S	S*W	S	S*W	S	S*W
Costs	3	0.92	1	0.31	1	0.31	2	0.62	5	1.54
Protectiveness - Residential	4	1.05	5	1.32	5	1.32	4	1.05	3	0.79
Protectiveness - Ports	5	0.66	4	0.53	4	0.53	3	0.40	2	0.26
Protectiveness - Ecological	1	0.07	2	0.13	2	0.13	3	0.20	4	0.26
Accessibility	1	0.08	2	0.15	2	0.15	3	0.23	4	0.31
Technical feasibility	1	0.15	2	0.31	4	0.62	4	0.62	5	0.77
Total		3.20		2.75		3.05		3.11		3.93

Table 3.11 shows the weighted performance of each location on the criteria.

Location 7 obtains the highest overall score, indicating it is the most favorable location to further investigate for a SSB in Tokyo Bay. It has a small wet cross-sectional area, shallow depth, and limited interference with existing activities, which make it the most viable and cost-efficient option. Although its storage capacity is smaller than other alternatives and it does not protect the entire Tokyo Prefecture, it effectively safeguards the most densely populated and vulnerable low-lying zones. Additionally, its relatively simple construction is likely to result in lower costs and reduced governmental and public resistance. Further analysis is required to assess the required storage area and overall hydraulic performance.

3.2.4. Validation: Cost-property value analysis

The results from the weighted MCDA are validated by a cost-property value analysis as proposed in Section 2.2.4. In this section the results of the cost-property value analysis are shown and compared to the results of the weighted MCDA.

Costs

It is estimated that a total length of 41.2 $[km]$ of levees needs to be reinforced for Location 7, based on Google Earth. This estimate is based on the assumption that the levees alongside the Edo and Tama rivers must be raised up to the first watergate in each river. The additional costs are estimated to be 19 billion yen based on the height increase and costs found in the methodology.

Table 3.12 shows the cost estimation for each location based on what was described in Appendix G. From this, it becomes clear that the absolute costs associated with Location 7 are significantly lower than those associated with the other locations.

Table 3.12: Costs per location (incl. inflation).

Location	4	5a	5b	6	7
Barrier costs [Billion ¥]	3264.92	2261.06	2060.29	989.51	487.58
Additional costs [Billion ¥]	0	0	0	0	19
Total costs [Billion €]	18.98	13.15	11.98	5.75	2.95
Total costs [Billion $]	22.21	15.38	14.02	6.73	3.45
Total costs [Billion ¥]	3264.92	2261.06	2060.29	989.51	506.84

Property value

Table 3.13 shows the key parameters and the property value estimation for each location. From the table, it becomes clear that the costs associated with damage do not significantly differ between the different locations using the method proposed in Section 2.2.4.

Table 3.13: Calculation of property value of each SSB location, based on example calculation for Edogawa.

Zone	Affected area [m^2]	Population density [$\#/km^2$]	Property value (2015) [Billion ¥]	Property value 2025 [Billion ¥]
Edogawa (example)	49.9	13987	234.29	267.09
Location 7	435	15510	2264.80	2581.87
Location 6	485	7036	2382.89	2716.49
Location 5a & b	525	3587	2431.05	2771.40
Location 4	565	703	2440.48	2782.15

Cost-property value ratio

Table 3.13 presents the resulting property value-cost ratio for each location. From Table 3.13, it can be concluded that the property value-cost ratio > 1 for every location except for Location 4. This indicates that, based on the estimated costs and property value, the construction of the barrier at Location 4 would be more costly than the property value it protects. Location 7 provides the highest property value-cost ratio. Compared to locations 4, 5a, 5b, and 6, Location 7 is approximately 6.6, 4.6, 4.2, and 2 times more economically beneficial, respectively.

Table 3.14: Cost-value property analysis ratio.

Location	4	5a	5b	6	7
Property value-cost ratio	0.86	1.24	1.37	2.84	5.69

Consequently, Location 7 is the most favorable based on the outcomes of the MCDA and the cost-property value analysis. Therefore, Location 7 will be further investigated as it forms a promising location for the construction of a SSB in order to prevent typhoon-induced flooding in Tokyo. In the next sections the selected location will be further evaluated to determine whether the location offers enough storage capacity and what the dimensions should be for a typhoon occurring every 200 years.

3.3. Design typhoon for Tokyo

The following section discusses the resulting parameters describing the design typhoon for Tokyo. The methods in order to derive these design parameters are presented in Section 2.3. First, the results of Method 1 are outlined in Section 3.3.1 describing the parameters related to the surge and in Section 3.3.2 the precipitation is determined during the design typhoon is determined for different return periods, and finally in Section 3.3.3 the resulting design values for the design typhoon are determined via a joint probability distribution.

3.3.1. Method 1: Resulting design storm surge variables

Data to determine surge

As a result, the method described in Section 2.3.1, data is obtained for a larger area than Tokyo. The area of interest is increased to 10°N–50°N and 120°E–180°E, which leads to a larger number of typhoons. The database used was NOAA's International Best Track Archive for Climate Stewardship (IBTrACS) (Gahtan et al., 2024; Knapp et al., 2010). From IBTrACS, the following columns were used NAME, ISO TIME, LAT, LON, LANDFALL, TOKYO WIND, and TOKYO PRES. For TOKYO WIND, the values are replaced by the values measured by the Japan Meteorological Institute (JMA), because JMA measures the 10-minute sustained wind speeds whereas NOAA measures the 1-minute sustained wind speeds. The 10-minute sustained wind speed is assumed to more reliably indicate what the driving wind speed is behind the storm surge (Typhoon, n.d.-a). Additionally, only data from 1984 onward is used, as records prior to this year are considered less reliable due to a change in measurement technique (Knapp & Kruk, 2010).

After filtering the database to include only typhoons that made landfall at least once within the area of interest, and saving the wind speeds 18-hour prior to each landfall event by using the LANDFALL column in the IBTrACS database which indicates the moment of landfall of typhoons (as explained in Section 2.3.1), the resulting set of typhoons is shown in Figure 3.6. This database is referred to as $Database_{T,NWP}$ as explained in Section 2.3.1.

It should be noted that the values for the wind speed in the IBTrACS database, the wind speeds measured by JMA, are rounded to 0, 3, 5, and 8 knots. This points to a large error in the measurements, therefore uncertainty in the data and in the model, and therefore unwanted effects during data analysis.

As explained in Section 2.3.1, a Tokyo specific database is created for typhoons that made landfall in Tokyo in the direction to create a surge in Tokyo Bay, also referred to as $Database_{T,T}$. This is done by filtering the 18-hour wind speed prior to landfall derived dataset ($Database_{T,NWP}$) by selecting typhoons that pass Tokyo in a radius of 150 $[km]$, and using the specific typhoon data of Tokyo obtained from the Digital Typhoon Database composed by the Kitamoto Laboratory of the National Institute of Informatics (Typhoon, n.d.-a). Additionally, the resulting list was manually filtered to ensure that it only includes typhoons that made landfall near Tokyo in the direction to create a surge in Tokyo Bay. This step was necessary because some typhoons can pass within the 150 $[km]$ radius while making landfall farther away, whereas in this database, only landfall events specific to the Tokyo area are of interest in the direction to create a surge. The direction to create a surge in Tokyo Bay means that the typhoons need to make landfall on the southern coast of Tokyo. The surge will be minimal if present in Tokyo Bay if typhoons make landfall on the Eastern coast of Tokyo.

The typhoon tracks and 18-hour before landfall moments of the selected typhoons of both filtered databases are shown in Figure 3.6.

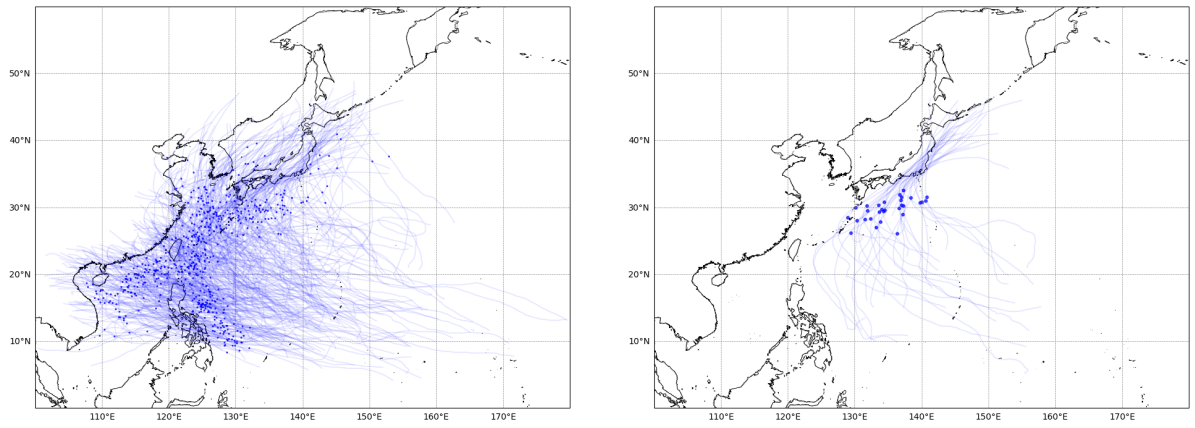

(a) $Database_{T,NWP}$ (b) $Database_{T,T}$

Figure 3.6: The plots show the included typhoons per database, of which the track (line) and location of the typhoon eye 18-hour before landfall is shown (dot).

Wind speed 18-hour before landfall

The POT is performed on the $Database_{NWP,T}$ as described in Section 2.3.1. The database includes the 18-hour wind speed prior to landfall of typhoons in the Northwestern Pacific between 1984 and 2024 as shown in Figure 3.7. As visible in Figure 3.7, the data are rounded to 0, 3, 5, 8 knots, explaining the vertical pattern visible in the figure.

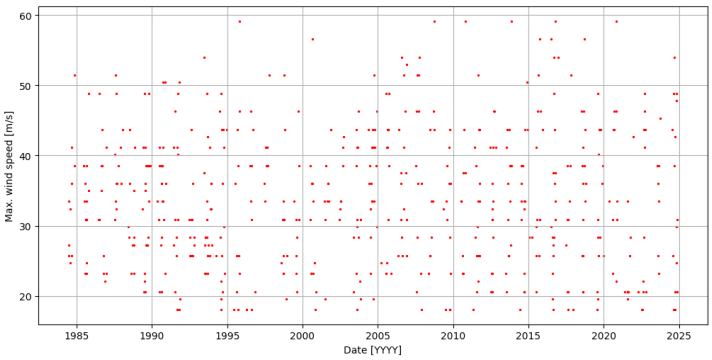

Figure 3.7: The maximum winds of a typhoon measured over a 10-minute period 18-hour prior to landfall in the Northwestern Pacific from the $Database_{NWP,T}$.

As explained in Section 2.3.1, a moving window of 21 years is used to determine if there is a noticeable change in wind speed 18 hours prior to landfall in time. Per window, a GPD is fitted after a threshold value is chosen per window using threshold stability plots. The threshold c is chosen to be 37 $[m/s]$ for each window as from Figure H.1 in Appendix H it appears that for 37 $[m/s]$ all have reasonable confidence bounds until then. This means that enough data is left in order to obtain a relatively reliable fit of the GPD. Furthermore, choosing the same c enhances interpretability.

The resulting fitted distributions are shown in Figure 3.8, from which it can be concluded that over time, the probability of more extreme wind speeds 18 hours prior to landfall increases in the Northwestern Pacific in the previously set area of interest. This could be attributed to numerous causes such as climate change (Hoshino et al., 2016a), inter-annual climate oscillations (Kang et al., 2019), etc. However, due to the relatively short time span of this research, the distribution explaining the most recent period has been used without determining the actual cause of the change in probability.

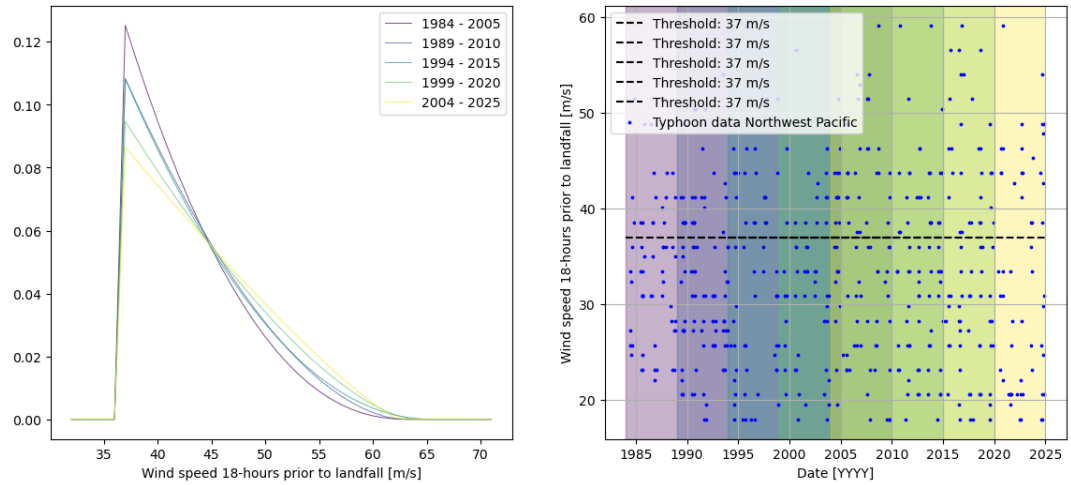

Figure 3.8: The left-hand plot shows the probability density function ($P[W \leq x \mid x > c]$) of the GPD distribution of typhoons over the Northwest Pacific fitted for each of the moving windows through time. The right-hand plot shows wind speed of typhoons 18 hours prior to landfall in the Northwest Pacific between 1984 and 2024, including the moving time window of 21 years for which a GPD is fitted for every increment in time of 5 years.

As the GPD represents the conditional probability $P[W > w \mid W > c]$, the unconditional probability is obtained by multiplying the conditional probability by the exceedance probability $P[W > c] = 40.7\%$.

Eventually the design values were obtained using Equation 2.5, with $\lambda = \frac{30}{41}$ using Equation 2.4 as explained in Section 2.3.1. In the equation 30 represents the number of typhoons making landfall in Tokyo in the direction to cause a surge between 1984 and 2024 (Typhoon, n.d.-a). The resulting

$W_{design,RT}$ values for different RT are stated in Table 3.15 and illustrated in Figure 3.9. Included in both the table and the figure are the 95% confidence intervals, which widen for larger values of wind speed. This stems from the fact that wind speeds in the extreme tail occur inherently less frequently. extreme wind speed the less it occurs. Fewer extreme observations increase the sampling variability of the extreme observations, leading to greater variation among the extreme observations between the bootstrapped samples. Consequently, the confidence intervals widen for higher wind speeds, reflecting this increased uncertainty.

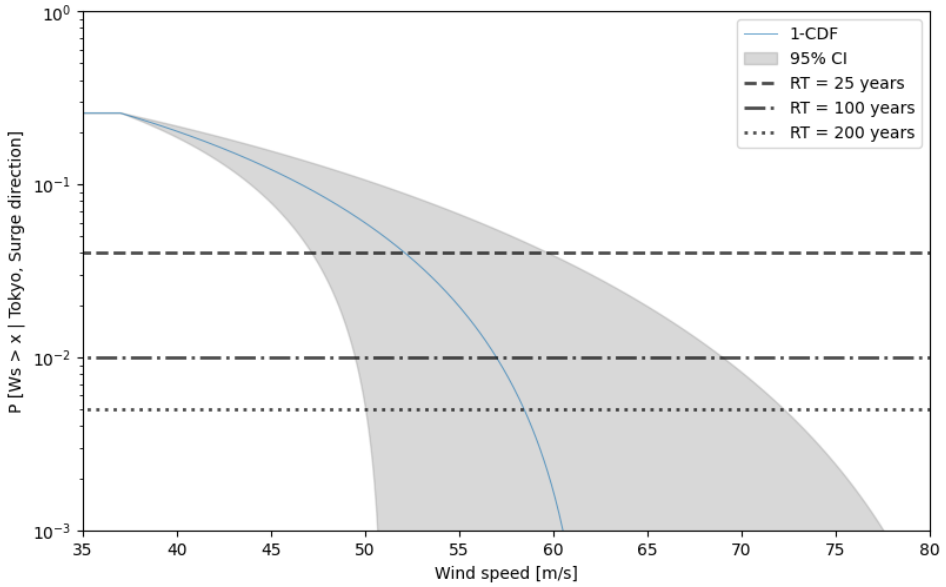

Figure 3.9: Probability per year of a typhoon exceeding a certain extreme wind speed that makes landfall in Tokyo and has the right direction to cause a storm surge, including the 95% bootstrapped confidence intervals by bootstrapping $n = 1000$ times.

Table 3.15: Design wind speeds 18-hour prior to landfall for different return periods, including their corresponding bootstrapped 95% confidence bounds by bootstrapping $n = 1000$ times.

RT [years]	Wind speed [m/s]	95% Confidence Bounds [m/s]
25	52.1	[47.2, 59.7]
100	57.0	[49.5, 69.0]
200	58.4	[50.0, 72.3]

Atmospheric pressure 18-hour prior to landfall

As explained in Section 2.3.1, a relationship is explored between the atmospheric pressure and wind speed during a typhoon 18-hour prior to landfall. The atmospheric pressure data is again obtained 18-hour prior to landfall, similar to the wind speed. This report assumes that the atmospheric pressure 18-hour prior to landfall is best correlated with the observed storm surge height based on the relationship between storm surge height and wind speed found by Needham & Keim (Needham & Keim, 2013). Here a first, second, third, and fourth order polynomials are fitted to the wind and atmospheric pressure data as shown in Figure I.1 in Appendix I, where their fit is evaluated using the Overall Model Test and compared to each other using Alternative Hypothesis testing.

However, as shown in the captions of each plot in Figure I.1 in Appendix I, all of the hypotheses are rejected according to the Overall Model Test using a false alarm probability of 5%. Furthermore, each time a higher-order polynomial is chosen as an alternative hypothesis, the Generalized Likelihood Ratio Test accepts the alternative hypothesis. This could imply that a higher order polynomial is required to describe the relationship between atmospheric pressure and wind than the already hypothesized order polynomials. However, currently, the standard deviation belonging to the atmospheric pressure is set

equal to 1 as the standard deviation remains unknown. Furthermore, the wind speed itself is rounded to 0, 3, 5, 8 knots, resulting in ambiguity by itself, even without taking into account the measurement precision. If a variance higher than 1 would be taken into account, the OMT and GLRT would quicker sustain a null hypothesis. In addition, a higher-order polynomial would possibly lead to overfitting the data. As a result, preferably a lower-order polynomial is selected to prevent overfitting the data, which could lead to unwanted and unreliable effects if extrapolation is necessary.

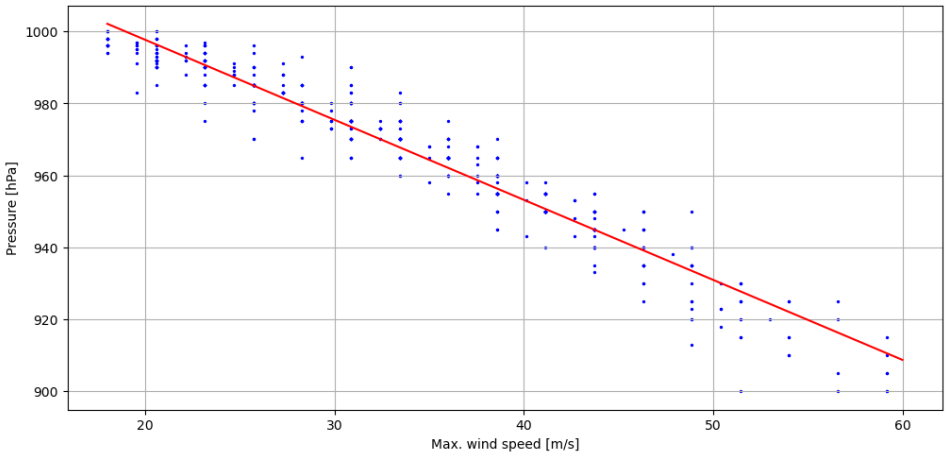

Figure 3.10: The figure shows the first-order polynomial selected to describe the correlation between the wind speed and atmospheric pressure data 18 $[h]$ to landfall.

Following the previous reasoning steps, for now, a first-order polynomial is selected, visualized in Figure 3.10, as it describes the data best. However, it is preferred to enhance the selection process by incorporating the uncertainty and ambiguity in the OMT and GLRT. A higher order polynomial would have been preferred if extrapolation were not required to reach the atmospheric pressures associated with design wind speeds following from Table 3.15 exceeding the observed wind speeds. A higher-order polynomial can lead to highly biased results when extrapolation is required. In this case, the confidence bounds for the design wind speed with a return period of 100 and 200 years, according to Table 3.15 exceed the observed wind speeds in Figure 3.10, meaning that extrapolation is required. Consequently, a first-order polynomial is best to describe the relationship between atmospheric pressure and wind speed. The first-order polynomial will lead to a higher variance, but a relatively unbiased fit (also during extrapolation).

Wind direction at landfall

For this simple first model, the actual wind direction of the design typhoon is assumed to have the ideal wind direction to create a surge. According to Md. Rezuanul Islam (2020), the ideal wind direction to create a surge is parallel to the longitudinal axis of the bay. This means that under the assumption that the maximum wind speed and storm track are parallel, the storm track and wind direction are equal is estimated to be 195° using Google Earth (Google, 2025).

In conclusion of Section 3.3.1, the resulting fitted distribution for wind speed intensity 18-hour prior to landfall, the relationship between wind speed and atmospheric pressure, and the determined wind direction can be used in the 1D-model to evaluate the storage capacity of Location 7 and determine important design parameters for dimensioning the barrier.

3.3.2. Method 1: Resulting design precipitation during typhoons

Precipitation data

Precipitation data used originate from the Tokyo weather station (35°41”5, 139°45”0) of the Japan Meteorological Agency (JMA, 2025a), which measures hourly rainfall at an elevation of 25.2 [m]. Since the typhoon dataset described in Section 2.3.1 only consists of data from 1984 onward, the precipitation

data is also extracted from this year onward. As explained in Section 2.3.2, the 6-hour cumulative precipitation until the moment of landfall ($Database_{6hr}$) and the 10-hour cumulative precipitation ($Database_{10hr}$) following the moment of landfall are found for the typhoons in $Database_{T,T}$. The resulting precipitation amounts in the $Database_{6hr}$ and $Database_{10hr}$ are shown in Figure 3.11a and 3.11b respectively.

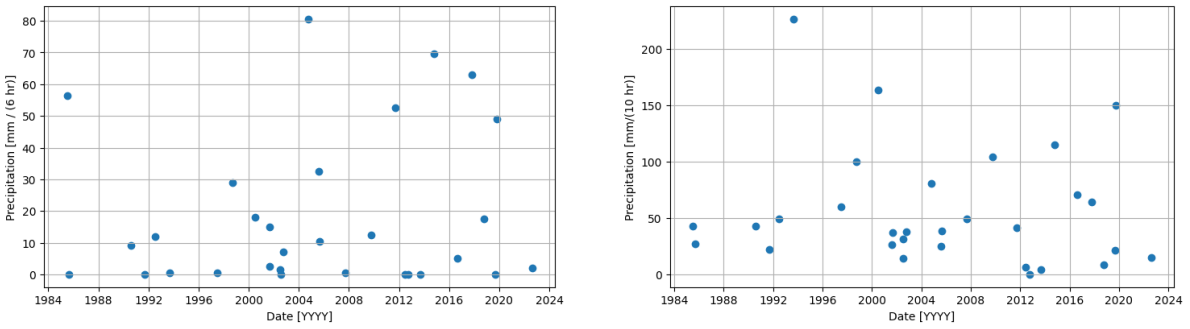

(a) (b)

Figure 3.11: The plots show the retrieved cumulative precipitation from 6 hours before landfall until the moment of landfall and from the moment of landfall until 10 hours later, respectively of historic typhoons making landfall in Tokyo and creating a significant surge since 1984.

Possible correlations

Using the methods described in Section 2.3.2 possible relationships are explored between the variables of interest. As visible in Figure 3.12, no clear relationship can be found between the precipitation amount before landfall and wind speed intensity 18-hour prior to landfall. In addition, no clear relationship can be found between the precipitation amount during landfall and wind speed intensity 18 hours prior to landfall. This result is substantiated by Um et al. (2017), who found similar results when trying to establish a relationship between horizontal wind speed intensity and precipitation amounts for typhoons in the Northwestern Pacific at the Jeju weather station in South Korea. According to the study, both low and high precipitation amounts could occur during high wind speeds. Furthermore, according to the article, hydrological statistics does not yet well understand the relationship between horizontal wind speed intensity and precipitation amounts of typhoons (Um et al., 2017). As a result, precipitation amount during the design typhoon can be modeled independently of storm surge height, validating the approach used in Method 1.

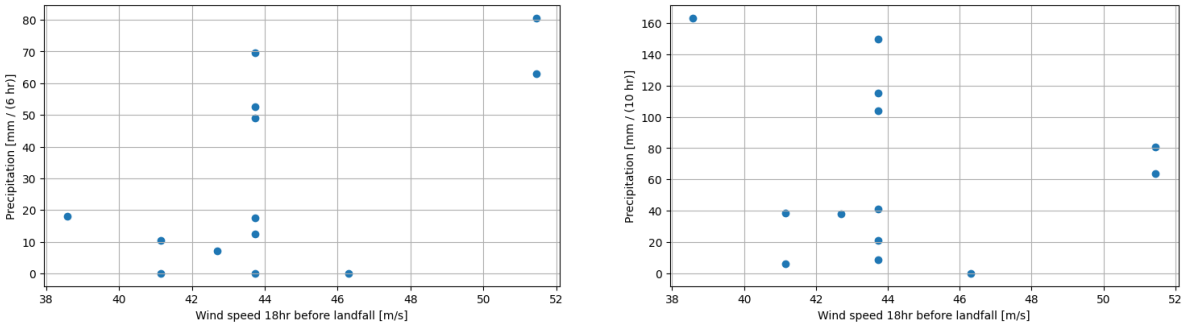

(a) 6-hour cumulative precipitation **(b)** 10-hour cumulative precipitation

Figure 3.12: The plots show that no clear relationship can be found between the wind speed intensity 18-hour prior to landfall and both of the cumulative precipitation amounts of historic typhoon events in Tokyo that created a significant surge.

In addition, the relationship between the precipitation amounts prior to landfall and the precipitation amounts following landfall. Figure 3.13 shows that no clear relationship can be found between the 6-hour cumulative precipitation amounts prior to landfall and 10-hour cumulative precipitation amounts

following landfall. However, the inability to find a relationship could stem from a lack of data points or the incorrect classification of landfall events. In this report, these potential causes are not further investigated due to the time frame in which the research had to be performed. Consequently, precipitation before landfall and the precipitation following landfall are considered independent processes and can therefore be modeled separately.

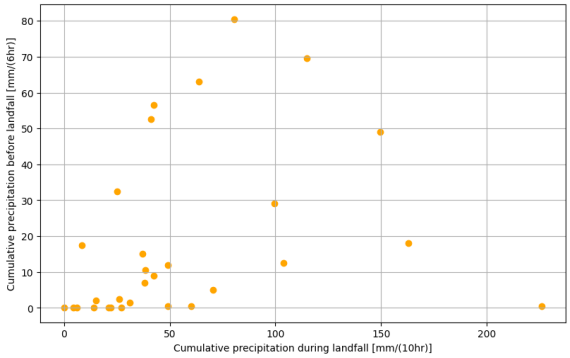

Figure 3.13: The plot shows that no clear relationship can be found between the 6-hour cumulative rainfall until landfall and the 10-hour cumulative rainfall from landfall of typhoon events in Tokyo that created a significant surge.

Fitted precipitation distributions

The resulting distribution for both the 6-hour and 10-hour precipitation as defined in Section 2.3.2 is an exponential distribution. The fitted exponential distributions are visualized in Figure 3.14 where the observed values are also visible.

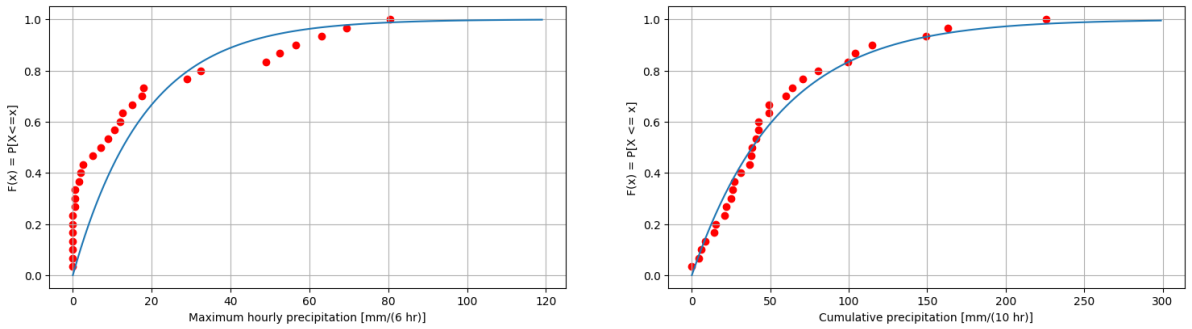

(a) (b)

Figure 3.14: The cumulative density functions of both exponential distributions fitted to the 6-hour and 10-hour cumulative precipitation during historical typhoons in Tokyo that made landfall between 1984-2024.

From Figure 3.14 it already becomes clear that the exponential distribution does not represent the 6-hour precipitation data well. This is acknowledged by the evaluation of the goodness of fit using a QQ-plot and Logscale-plots as visualized in Figure 3.15a. However, after having fitted numerous distributions, such as the Lognormal and the Right-handed Gumbel distribution, the exponential distribution appeared to give the least bad fit. Due to the time frame in which the report is written, this distribution is assumed to represent the 6-hour cumulative precipitation despite the failed diagnostic tests.

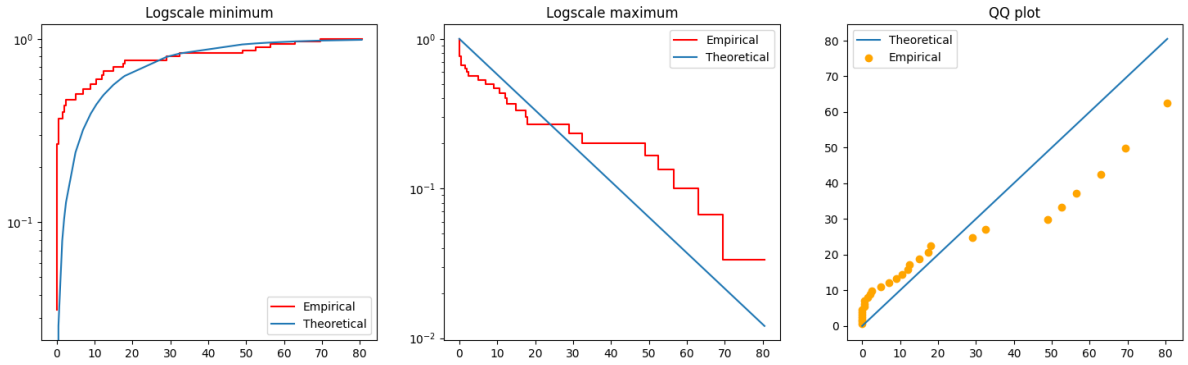

(a) Graphical diagnostics: 6-hour cumulative precipitation.

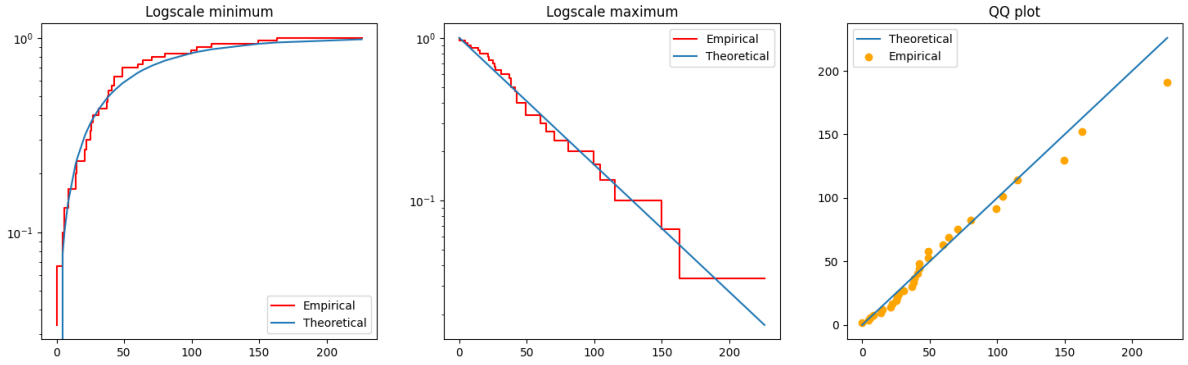

(b) Graphical diagnostics: 10-hour cumulative precipitation.

Figure 3.15: The figures illustrate the goodness of fit for the two exponential distributions. The exponential model representing the 6-hour cumulative precipitation fails all graphical diagnostic tests, indicating that it does not adequately capture the lower tail, main body, or upper tail of the observed data. In contrast, the exponential model for the 10-hour cumulative precipitation provides a satisfactory fit for both the lower tail and central portion of the distribution, although the upper tail is less accurately represented, as visible by deviations in the log-scale maxima- and QQ-plots.

An exponential distribution does seem to represent the 10-hour cumulative precipitation well, according to Figure 3.15b. Only the upper tail is not perfectly captured by the distribution as visible in the QQ-plot and Logscale maxima-plot. However, for precipitation, not only the upper tail is of interest, as low precipitation can also occur during a high storm surge. As a result, the exponential distribution is considered in this report to represent the 10-hour precipitation data well.

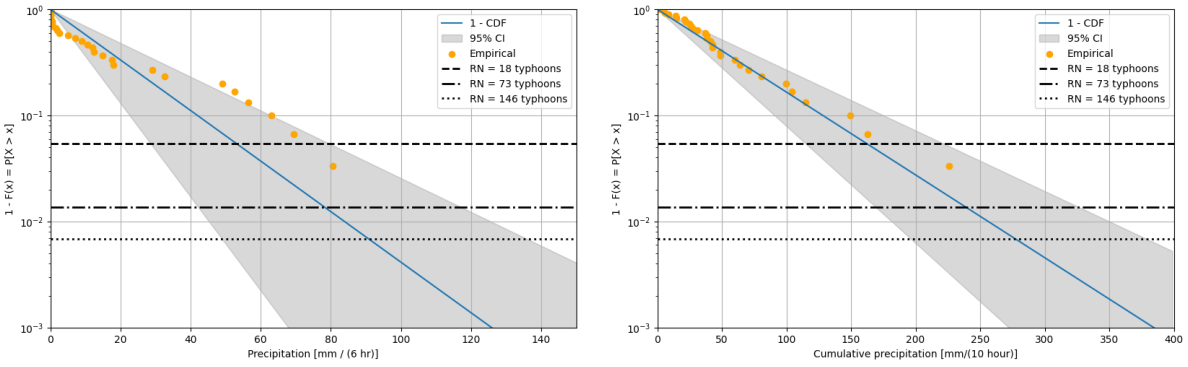

(a) **(b)**

Figure 3.16: The figure shows the exceedance probability functions of both exponential distributions fitted to the 6-hour and 10-hour cumulative precipitation during historical typhoons in Tokyo that made landfall between 1984-2024, including the 95% bootstrapped confidence intervals by bootstrapping $n = 1000$ times. In addition, the return levels considered to determine the design precipitation values are plotted, specified in RN (return number of typhoons).

Figure 3.16 shows the exceedance probability functions from which the design values for cumulative precipitation can be determined for each return period. The figure also includes the 95% confidence intervals, which become wider for higher cumulative precipitation values. This occurs because fewer data points are available in the extreme tail, as such events are inherently rare. With fewer extreme observations, the sampling variability of the extreme observations increases, leading to greater variation among the extreme observations between the bootstrapped samples. Consequently, the confidence intervals widen for larger cumulative precipitation values, reflecting this increased uncertainty.

The design cumulative precipitation until landfall is determined from the 6-hour cumulative precipitation exceedance plot and the design cumulative precipitation from the moment of landfall is determined from the 10-hour cumulative precipitation exceedance plot. Note that the return periods considered are 25, 100, and 200 years. However, as the distributions describe the probability per typhoon, these return periods are first converted using $\lambda = \frac{30}{41}$ using Equation 2.4 as explained in Section 3.3.1 to return the number of typhoons (RN). The resulting design values are summarized in Table 3.16 for the 6-hour cumulative precipitation and in Table 3.17 for the 10-hour cumulative precipitation. In addition to the return periods and corresponding design values stated in Tables 3.16 and 3.17, the fitted distributions can be used in the 1D-model to evaluate the storage capacity of Location 7 and determine design values for dimensioning the barrier.

Table 3.16: Design cumulative precipitation amounts including their bootstrapped 95% confidence bounds for different return numbers by bootstrapping $n = 1000$ times, where the 6-hour cumulative precipitation represents the rainfall until landfall.

RN [typhoons]	Precipitation [mm/(6 hr)]	6-hour 95% CI [mm/(6 hr)]
18	52.9	[28.6, 79.2]
78	78.2	[42.2, 117.0]
156	90.8	[49.0, 135.9]

Table 3.17: Design cumulative precipitation amounts including their bootstrapped 95% confidence bounds for different return numbers by bootstrapping $n = 1000$ times, where the 10-hour cumulative precipitation represents the rainfall from the moment of landfall.

RN [typhoons]	Precipitation [mm/(10 hr)]	10-hour 95% CI [mm/(10 hr)]
18	161.7	[114.5, 220.8]
73	238.9	[169.1, 326.0]
146	277.5	[196.4, 378.7]

However, the results should be interpreted with caution, as the resulting design amounts in Tables 3.16 and 3.17 may be optimistically low, because both distributions underestimate the extremes (Figure 3.16).

3.3.3. Method 2: Resulting joint probability distribution between surge and precipitation

As mentioned in Section 2.3.3, the $DatabaseT, T$ is filtered further to only include wind speed events higher than the threshold $c = 37$ $[m/s]$. Consequently, the size of the resulting database $N_{JP,data}$ for wind speed 18 hours prior to landfall, and the corresponding values for precipitation 6 hours until landfall, and 10 hours following landfall is equal to $N_{JP,data} = 13$.

Despite the lack of data, the Frank copula is fitted using the parameters of the previously fitted exponential distributions describing precipitation and the parameters of the previously fitted Generalized Pareto distribution describing wind speed 18 hours prior to landfall. The resulting θ parameter of the Frank copula is equal to 2 for both distributions. In this report, the resulting θ parameter is not further investigated due to time constraints. The only validation performed is by comparing the resulting values of wind speed and precipitation amounts with those obtained from Method 1. Consequently, the proposed fitting method cannot be considered validated, and the fitted parameter could be biased, potentially resulting in misleading conclusions. However, in this report, θ is treated as an unbiased

estimate, such that Method 2 can be used in this report to obtain preliminary results and give an indication of how the wind speed in combination with precipitation can be obtained.

Table 3.18: The resulting θ parameter of the fitted copula for both joint probability distributions.

Frank Parameter	Estimated Value
$\theta_{w,6hr}$	2.0
$\theta_{w,10hr}$	2.0

The θ parameter describes the dependence of the data that are fitted. Here, a θ equal to 2 means that the wind and precipitation for both durations are slightly positively correlated. However, the upper tails remain independent as the Frank copula can inherently not model tail dependence well (Gopinath, 2025). The resulting relationship, described by θ, is assumed to represent the actual relationship. When observing the data in Figure 3.17, it also shows that the data seem independent or slightly positively correlated, which is also mentioned in Section 2.3.2 despite using the entire $Database_{T,T}$. Furthermore, the same θ for both of the joint probability distributions seems logical, as Figure 3.17 shows that the 6-hour cumulative precipitation and wind speed 18-hour before landfall, and the 10-hour cumulative precipitation and wind speed 18-hour before landfall have a similar dependence structure.

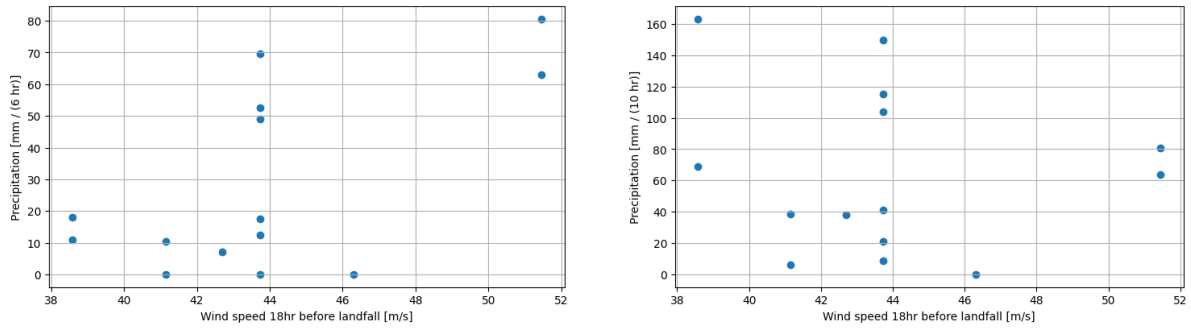

(a) Wind speed & 6-hour cumulative precipitation

(b) Wind speed & 10-hour cumulative precipitation

Figure 3.17: Both figures show an independent or slightly positive dependence structure using only the data pairs with wind speeds larger than 37 [m/s].

Using the fitted copula and the previously named input parameters, a Monte Carlo simulation of the fitted joint distribution can be applied using $N_{MC} = 10000$ samples. From the Monte Carlo simulation, a probability pair is obtained with each a probability for a wind speed and an amount of precipitation per typhoon. Using Equations 2.13 and 2.14 as explained in Section 2.3.3 respectively, the probabilities obtained from the Monte Carlo simulation can be transformed into wind speeds 18-hour before landfall, and their corresponding cumulative precipitation (either 6 hours until landfall or 10 hours after landfall). The resulting generated typhoon events, including a wind speed and precipitation amount are plotted in Figure 3.18.

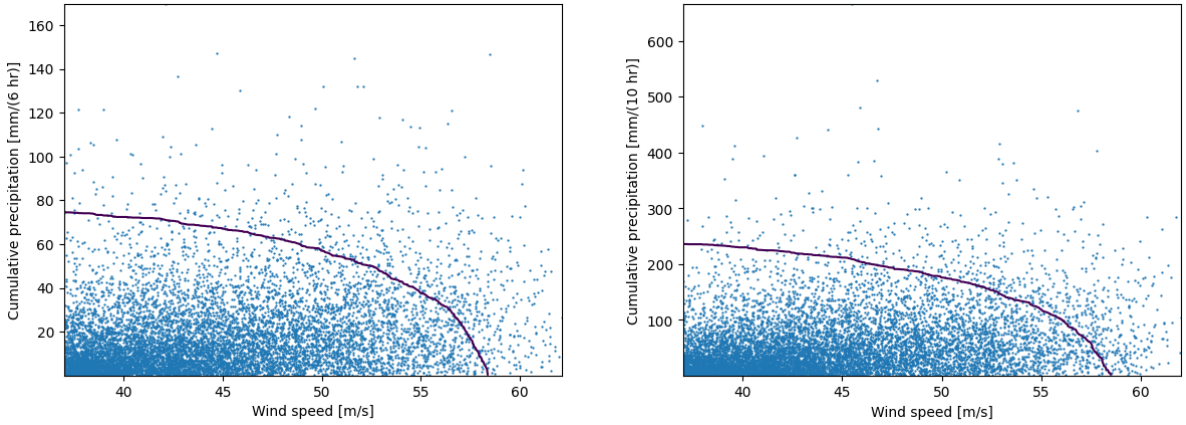

(a) Wind speed & 6-hour cumulative precipitation

(b) Wind speed & 10-hour cumulative precipitation

Figure 3.18: The figure shows the Monte Carlo simulation of $N_{MC} = 10000$ samples of both fitted joint probability distributions using the Frank copula. In addition, the return level curve for a design return period of 200 years is included.

In Figure 3.18, the return level curve for a design return period for a typhoon of 200 years is included. However, as the generated probabilities using the Monte Carlo simulation are per typhoon, the probability following from the design period should be transformed to p using Equation 2.12. Here, $\lambda_{q,Tokyo}$ is equal to $\frac{13}{41}$ typhoons with a wind speed 18-hour prior to landfall exceeding 37 $[m/s]$, making landfall in Tokyo with the direction to cause a surge per year. The resulting p is equal to 0.015.

The resulting return level curve represents the possible combinations between wind speed intensity 18-hour prior to landfall and precipitation amounts before and during landfall for a typhoon that occurs once every 200 years. This means that the typhoon occurring once every 200 years can have a wind speed 18-hour prior to landfall of 58 $[m/s]$ and at the same time almost no precipitation. Yet, at the same time, the typhoon can have a wind speed 18-hour prior to landfall of 40 $[m/s]$ and around 70 $[mm/(6hr)]$ cumulative precipitation until landfall and 230 $[mm/(10hr)]$ cumulative precipitation following landfall.

However, as explained in Section 2.3.3, the wind speeds obtained from both distributions in Figure 3.18 do not match up perfectly. Consequently, a polynomial is fitted, where in contrast to the atmospheric pressure, a high-order polynomial is preferred as no extrapolation is required. A fifth-order polynomial passed the Overall Model Test with a false alarm rate of 5% for the bivariate distribution describing wind speed and 6-hour cumulative precipitation as visible in Figure 3.19.

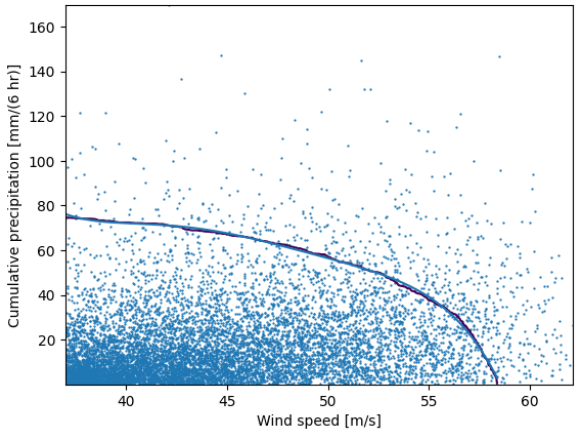

Figure 3.19: The figure shows the Monte Carlo simulation of $N_{MC} = 10000$ samples of the joint probability distribution describing the 18-hour prior to landfall wind speed and the 6-hour cumulative precipitation until landfall using the Frank copula. In addition, the return level curve for a design return period of 200 years is included in red, and the 5th order polynomial describing the return level curve is added in blue.

Consequently, the resulting Figures 3.18 and 3.19 shows the 6-hour and 10-hour cumulative precipitation amounts corresponding to wind speeds that are likely to occur simultaneously during a 200-year design typhoon. These curves can be used in the 1D-model to assess whether Location 7 has sufficient storage capacity to withstand the critical combination of wind speed and precipitation to be derived from the curves. In addition, the curves can support the determination of key design parameters by identifying critical combinations of wind speed and/or precipitation relevant for the barrier's dimensioning.

3.3.4. Proxy storm

Typhoon Hagibis was selected for analysis as it was classified as a Super Typhoon and recognized as the strongest typhoon to strike Japan in several decades. The event caused extensive damage, primarily due to its significant storm surge and high precipitation intensity, as discussed in Section 1.2.2. The proxy storm gives a combination of wind speed and precipitation based on the observations during Typhoon Hagibis. The recorded wind speed 18 hours prior to landfall was 43.7 $[m/s]$ with an atmospheric pressure of 945 $[hpa]$ 18 hours prior to landfall as recorded by JMA. The measured precipitation 6 hours prior to and 10 hours after landfall are determined by the JMA, 2025a and are found to be 49.0 $[mm/(6hr)]$ and 149.5 $[mm/(10hr)]$, respectively.

3.4. 1D-model

In this section, the results of the 1D-model are presented, describing the water levels behind and in front of the barrier positioned at Location 7. It is divided into four subsections. Section 3.4.1 addresses the resulting values for the boundary conditions, Section 3.4.2 discusses the resulting input parameters of the 1D-model which are related to a typhoon, Section 3.4.3 discusses the combinations following from the design typhoon of Method 1 and Method 2 evaluated in the 1D-model, and Section 3.4.4 determines the critical combinations resulting in the critical water levels behind and in front of the potential SSB for the evaluation of the storage capacity and for the determination of the hydraulic load required in the dimensioning of the barrier.

3.4.1. Boundary conditions 1D-model

As mentioned, the most important boundary conditions considered for the 1D-model are sea level rise, subsidence, tides, storage capacity, barrier closure time, and the normal river discharge of which the resulting values are discussed in this section.

Sea level rise h_{slr}

As described in the methodology, sea level rise (SLR) projections are obtained using NASA's projection tool (NASA, 2025). The conservative middle scenario (SSP3-7.0) is selected as explained in Section 2.4.1, as there is a considerable gap visible in Table 3.19 between SSP2-4.5 and SSP3-7.0.

Table 3.19: SLR projections until 2150 under different SSP scenarios (NASA, 2025).

Scenario	SLR in 2150 [m]
SSP1-1.9	0.35
SSP1-2.6	0.50
SSP2-4.5	0.77
SSP3-7.0	1.11
SSP5-8.5	1.27

The estimate for the year 2200 is provided in Table 3.19 (NASA, 2025). The corresponding SLR value of 1.6 $[m]$ from this table is included in the 1D-model.

Table 3.20: SLR projections until 2200 under SSP3-7.0 (NASA, 2025).

Scenario	SLR in 2200 [m]
SSP3-7.0	1.6

Subsidence

Subsidence is an important factor to include in an analysis to ensure sufficient water storage and prevent flooding when the barrier is closed. Historically, groundwater extraction caused rapid subsidence in Tokyo, but industrial pumping was halted in the late 1900s, so current subsidence from this source is negligible, as described by Nishi et al. (2023) and Erkens et al. (2015).

Furthermore, major earthquakes, such as the 2011 magnitude 9.0 event, caused significant subsidence, particularly in reclaimed land and Holocene deposits (Yasuda et al., 2012). A next point to consider is that minor earthquakes occur frequently, but little research exists on their contribution to subsidence. A key question could be whether individual minor earthquakes cause significant cumulative subsidence over time. While Interferometric Synthetic Aperture Radar data could help to address this question, the data remained unavailable during the development of this report. Besides, existing literature suggests that under normal circumstances, subsidence rates currently remain insignificant in Tokyo. As a result, this report assumes that subsidence can be neglected as an input parameter in the 1D-model.

Tides h_{tide}

The tidal range (TR) is estimated based on the hourly tide level graph from the Tide Observation data Tokyo provided by JMA (JMA, 2025b) for October 2024 in Tokyo. This results in a spring high tide of $+1.2$ $[m]$ T.P. and a spring low tide of about -1.2 $[m]$ T.P. (JMA, 2025b). This means the spring TR can be estimated to be 2.4 $[m]$.

The period Ttide of the tide is assumed to be equal to 12 hours and 25 minutes, referring to the semidiurnal tide. The resulting tidal scenarios taken into account in the 1D-model are spring low tide, mid tide, and spring high tide of the semidiurnal tidal cycle.

The key results from the analysis of the decrease in tidal range (TR) are summarized as follows. Firstly, the equilibrium cross-sectional area of the inlet is estimated based on the navigational gates determined in Section 3.6.1 and the flow inlet gates determined in Section 3.6.2. This is filled into Equation 2.16. This gives: $A_{eq} = 350 \times 19.75 + 780 \times 15 = 18617$ $[m^2]$. Then, using Equation 2.15, the corresponding tidal prism is $P = 172 \times 10^6$ $[m^3]$.

Based on measurements from Google Earth, the basin area is estimated as $A_{\text{basin}} = 80$ $[km^2]$, which, from Equation 2.17, provides an average tidal amplitude of ($H = 2.15$ $[m]$.

These results indicate an estimated reduction in tidal range of approximately 10.5%. This represents a significant decrease, and therefore, potential negative environmental impacts cannot be ruled out. However, for the purpose of this study, it is decided to exclude this in the 1D model, as these results are extremely preliminary following a rough estimation. Besides a reduction in tidal amplitude, the restricted flow area will also result in a tidal phase-lag over the barrier, not further researched in this study. Yet, in reality, it is likely that the tidal flow will be affected by the SSB.

Storage capacity in basin V_0

The surface area enclosed by the barrier is estimated using Google Earth and is approximately equal to 80 $[km^2]$.

Besides the area, the current and future levee heights are important for determining the storage capacity in the basin. The Tokyo Bay Coastal Conservation Master Plan by the Tokyo Metropolitan Government in 2019 determined the current and future levee heights, and which areas are heightened (Government, 2019).

According to this, the lowest levee height is currently +4.6 $[m]$ $A.P.$, and it is going to be heightened to +5.6 $[m]$ $A.P.$ by 2100 (Government, 2019). In the 1D-model, it is assumed that by the time the barrier is constructed, the lowest dikes will already be raised, ensuring a minimum dike height of +5.6 $[m]$ $A.P.$ at the time of construction.

The report by Government (2019) uses A.P., which stands for Arakawa Peil. To convert this to T.P. (Tokyo Peil), the following conversion is applied: 0.0 $[m]$ $T.P.$ = 0.0 $[m]$ $A.P + 1.134$ $[m]$ (K. R. O. MILT, n.d.).

Storage capacity Arakawa River

For the barrier positioned at Location 7, the Arakawa River is considered to be the only large river discharging behind the barrier. The storage volumes of the Arakawa River and its catchment area are determined via the method proposed in Section 2.4.1. The storage volumes along the Arakawa River are presented in Table 3.21 following literature research. In addition, the storage on land in the city is assumed to be an impervious surface, resulting in a storage depth equal to 1.5 $[mm]$ in the whole catchment area (Lyu et al., 2019).

Table 3.21: Storage facilities and volumes along the Arakawa River [1] (Information, n.d.), [2] (MLIT, n.d.-a), [3] (MLIT, n.d.-b), [4] (City, 2023), [5] (Prefecture, 2023), [6] (of Waterworks, n.d.), [7] (K. R. D. B. MILT, n.d.).

Storage facility	**Volume million [m³]**
Takizawa dam	58 [1]
Urayama dam	56 [1]
Futase dam	21.8 [2]
Mid-river regulating reservoir	39 [3]
Arima dam	4.4 [4]
Kakkaku dam	9.25 [5]
Sayama lake	19.5 [6]
Tama lake	58.6 [6]
Arakawa second and third retention ponds	51 [7]
Volume inside the river	75.9
Total storage volume	**393.45**

The calculation of the storage volume of the Arakawa River is shown in Table 3.22, which is based on Equation 2.18, resulting in 75.9 *million* $[m^3]$ storage. In this calculation, the allowable increase in water depth is assumed uniform along the entire river course, with a value of 4.4 $[m]$ (Chiyoda City, 2025).

Table 3.22: Arakawa River storage volume inside of the river calculation.

Measurement Point (Google Earth)	Width [m]	Length of Section [km]	Surface [m^2]
A-river upstream 4.0	18	22.7	408,600
Upstream 3.0	30.4	38.3	1,164,320
Upstream 2.0	72	38.7	2,786,400
Upstream 1.0	109	28.9	3,150,100
Downstream	431.66	11.6	5,007,256
Downstream 2.0	315	9	2,835,000
Mouth	760	2.5	1,900,000
Total Surface			17,251,676
Height			4.4 [m]
Total Volume			75.9 million [m^3]

The location of the measurement points used in Google Earth is displayed in Figure 3.20.

Figure 3.20: Arakawa measurement points, obtained from Google Earth (Earth, n.d.).

Barrier closure time

From the reference projects, the Maeslant Barrier requires approximately 2 hours to close (Rijkswaterstaat, 2023), while the MOSE Barrier takes about 30 minutes to close and 15 minutes to open (Wikipedia, 2025). In the model, a closure time of 3 hours will be included based on the maximum time it takes an existing reference barrier to close. Herein, the report assumes that the barrier will take longer to close than the Maeslant Barrier it as the gate size is assumed to be larger. Furthermore, in the 1D-model it is assumed that during the time it takes the barrier to close, no inflow or outflow through the gate is possible, whilst in reality, a reduced inflow or outflow would be present during the time it takes the gates to close. The consequence of this assumption is that, depending on the eventually selected gate type and the amount of precipitation during a typhoon, the water level inside the basin could in reality be higher than following from the 1D-model results.

In addition to the time it takes for a gate to close, which influences the moment of closure, the ability to forecast a storm surge is evaluated as explained in Section 2.4.1. A storm surge can be predicted 72 to 132 hours before reaching the bay, so this is not a critical factor for determining the moment a barrier should be closed (Hasegawa et al., 2023).

Furthermore, the time a storm surge is present in Tokyo Bay is evaluated to understand how long the barrier should be closed. It is found that a storm surge can remain in Tokyo Bay for up to 10 hours (Kawai & Takemura, 2003). As a result, in the 1D-model, it is assumed that from the moment the storm surge arrives, the storm surge will hold on for a duration of 10 hours.

Base river discharge $Q_{r,base}$

The base river discharge is determined by the discharge of the Arakawa River belonging to the period where surges have the highest likelihood to occur, as proposed by this report in Section 2.4.1. The result from the typhoon–storm surge analysis is presented in Figure 3.21, where the storm surge height data were obtained from the Japan Meteorological Agency database (JMA, 2025b) and the number of typhoons from the $Database_{T,T}$. From this graph can be derived that the relevant months for which the normal discharge of the Arakawa River should be accounted for are September and October as typhoons most often induce a storm surge during these months.

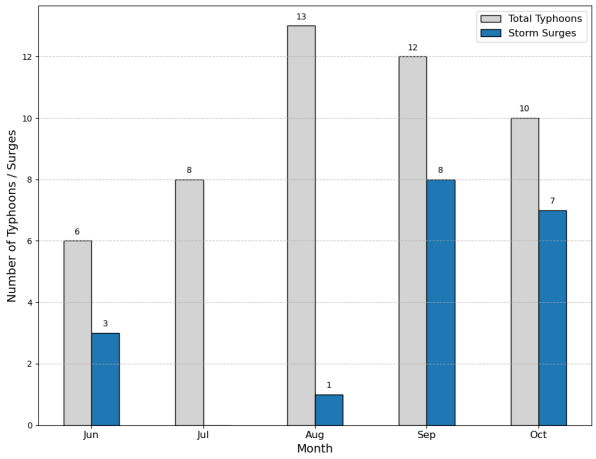

Figure 3.21: Typhoons vs storm surge around Tokyo by month.

From the literature review and available data, the base flow for September and October specifically could not be determined. Therefore, the average base flow of the Arakawa River was taken from the Arakawa Upper Reaches River Maintenance and Management Plan by MLIT. This gives a base discharge of 8.92 $[m^3/s]$ for the Arakawa River, approximated as $Qr, base \approx 9\ [m^3/s]$ (K. R. D. B. MILT, 2017).

As seen in Tokyo Bay, the base discharge is negligibly small compared to the peak discharge and can therefore be neglected in the 1D-model, as demonstrated in the following section.

3.4.2. Input parameters related to the typhoon of the 1D-model

An indication of the values of the input parameters of the 1D-model related to the typhoon is shown in this section.

Storm surge h_{ss}

This section provides an indication of the magnitude of the storm surges when applying the method to derive the storm surge height as described in Section 2.4.2 that will be used in the 1D-model. Figure 3.22 shows the resulting storm surge heights for different return periods when using Method 1 and a benchmark by including the observed storm surge height during the proxy storm Hagibis. From the figure, it can be concluded that the simulated storm surge height using the proposed method in Section 2.4.2 might be conservative relative to the observed value of the proxy storm. The return periods included have simulated wind speeds 18 hours prior to landfall equal to 52.1, 57.0, and 58.4 $[m/s]$, all exceeding the observed 18-hour wind speed prior to landfall of 43.7 $[m/s]$ of Hagibis. Yet, the other input parameters (atmospheric pressure and wind direction) could also influence the resulting storm surge height. However, the results of the simulated storm surge height are in the same order of magnitude as historically observed storm surge values. Therefore, the method proposed in Section 2.4.2 is considered a reasonable approach for application in the 1D-model.

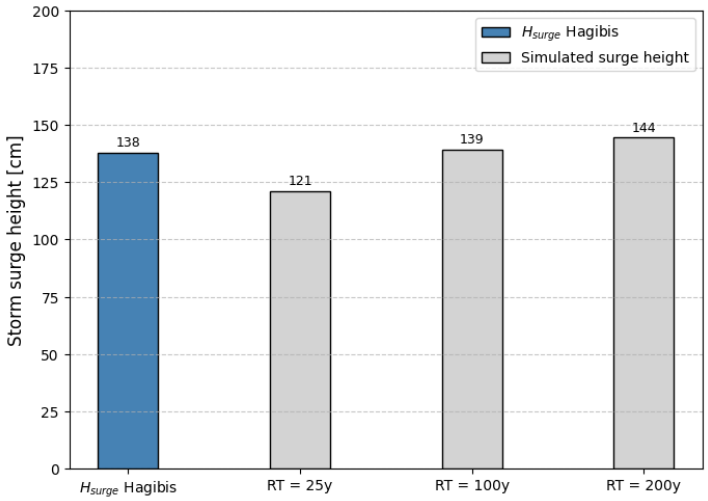

Figure 3.22: Indicative values for storm surge height using Method 1 to derive the wind speed, atmospheric pressure, and wind direction. The observed storm surge height of the proxy storm Hagibis is included to provide a benchmark.

Peak river discharge $Q_{r,peak}$

This section provides an indication of the peak discharge in the Arakawa River using the proposed approach described in Section 2.4.2, which will be applied in the 1D-model. Figure 3.23 shows the resulting discharge for different return periods when using Method 1 and the observed peak discharge during the proxy storm Hagibis, which is included as a benchmark. As explained in Section 2.4.2, the discharge amounts are obtained by multiplying the cumulative precipitation by the catchment area of the rivers discharging behind the barrier. At the barrier Location 7, the Arakawa River is considered to be the only large river discharging behind the barrier with a catchment area equal to $2,940$ $[km^2]$ (K. R. D. B. MILT, 2017).

Figure 3.23 shows that the simulated peak discharge always exceeds the observed peak discharge during Hagibis, which can be attributed to a number of causes. First, the 6-hour and 10-hour cumulative precipitation obtained using Method 1 for different return periods, respectively 52.9, 78.2, and 90.8 $[mm/(6hr)]$, and 161.7, 238.9, and 277.5 $[mm/(10hr)]$, exceed the 6-hour and 10-hour cumulative precipitation of Hagibis, which are equal to 49.0 $[mm/(6hr)]$ and 149.5 $[mm/(10hr)]$. Second, a simple hydrological model is used to determine the discharge, namely the precipitation times catchment area. In addition to other simplifications introduced by this simple hydrological model, this simple model assumes that there is no delay between precipitation and river run-off, which can result in larger peak discharge values. However, the method proposed in Section 2.4.2 is still considered a reasonable approach for application in the 1D-model, despite the larger simulated discharge values, as other historic events do have higher cumulative precipitation amounts, as visible in Figures 3.14, which could have lead to larger discharges.

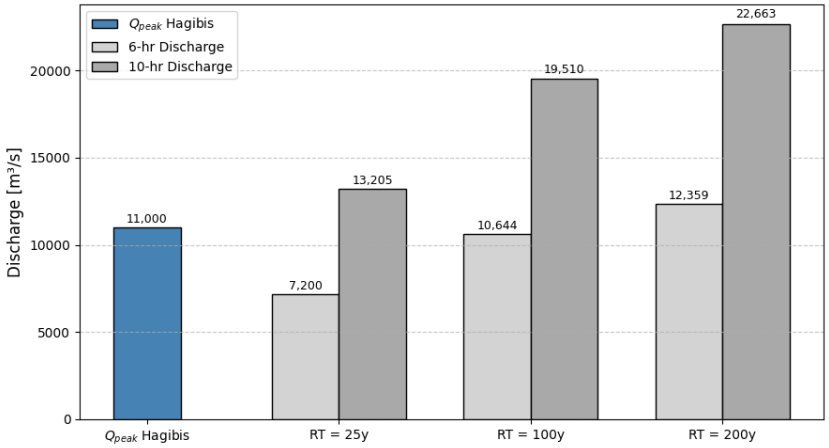

Figure 3.23: Indicative values for discharge of the Arakawa River following the 6-hour and 10-hour cumulative precipitation using Method 1 to derive the precipitation. The observed peak discharge of the proxy storm Hagibis is included to provide a benchmark.

Waves, h_{wave}

Winds associated with typhoons can lead to waves, which could lead to a higher water level in front of and/or behind the barrier. However, this report assumes that waves do not influence the water levels behind the barrier and in front of the opened gates during a storm surge event at Location 7 for the barrier. Consequently, the 1D-model does not consider the influence of waves on the water level behind and in front of the barrier. However, it should be noted that during the dimensioning of the barrier, waves are considered as a dynamic load on the barrier. The following assumptions lead to the neglect of waves in the 1D-model:

- Due to the shape of the bay and its geographical location, swell waves are not considered a major influence in the Bay compared to other factors such as storm surge and locally generated wind waves.
- When the barrier is closed, only locally generated wind waves occur within the basin. Since the available fetch is limited, these waves are assumed not to pose a significant threat to Tokyo.
- The presence of the barrier is assumed to influence wave behavior. When the gate is open, lower wave heights are expected inside the basin because of wave dissipation and diffraction, compared to a situation without the barrier.
- The report assumes that when the gates are opened during a storm surge and the water is flowing from behind the barrier through the gates to the bay, that the wave height will strongly decrease in front of the gate. The report assumes that this process can be compared to what happens to wave height during rip currents, in which the wave height decreases significantly **SOURCE**.

3.4.3. Wind speed & precipitation combinations

In this section, the resulting combinations per method are shown as described in Section 2.4.3, to evaluate the storage capacity of the barrier at Location 7 and determine the hydraulic load on the barrier at Location 7 for a typhoon with a design return period of 200 years.

Method 1

As mentioned in the methodology in Section 2.4.3, the combinations of $w_{RT,w}$ and $r_{RT,r}$ follow from the return period for wind speed and cumulative precipitation, respectively. The resulting combinations between return periods are shown in Table 3.23 to evaluate the storage capacity and in Table 3.24 to determine the hydraulic load using Method 1.

Table 3.23: Return period combinations for wind speed and cumulative precipitation using Method 1 to evaluate the storage capacity of Location 7 for a typhoon occurring once every 200 years.

Event	Wind RT (years)	Cumulative precipitation RT (years)
1	50	4
2	25	8
3	8	25
4	4	50

Table 3.24: Return period combinations for wind speed and cumulative precipitation using Method 1 to determine the hydraulic load at Location 7 for a typhoon occurring once every 200 years.

Event	Wind RT (years)	Cumulative precipitation RT (years)
1	200	1
2	1	200

Method 2

As outlined in the methodology for Method 2 in Section 2.4.3, Method 2 already describes the design typhoon with a design return period of 200 years in combinations between wind speed and cumulative precipitation as outlined in Section 2.3.3. For the storage capacity evaluation, combinations between wind speed and cumulative precipitation that could lead to relatively large values for both components are obtained from Figure 3.18. For the determination of the hydraulic load, combinations are selected that include either an extreme wind speed and negligible precipitation, or vice versa from Figure 3.18.

Proxy storm

The observed values are used for the input parameters of the 1D-model corresponding to the proxy storm. These include a storm surge height of 138 $[cm]$, a 6-hour cumulative precipitation of 49.0 $[mm/(6hr)]$, a 10-hour cumulative precipitation of 149.5 $[mm/(10hr)]$, and a peak discharge of $11,000$ $[m^3/s]$ (Ministry of Land, Infrastructure, Transport and Tourism (MLIT), Water Management and National Land Conservation Bureau, 2024).

3.4.4. Results of the 1D-model

The results of the 1D-model are split into two sections. Section 3.4.4 evaluates whether Location 7 has enough storage capacity to withstand the design typhoon with a return period of 200 years, and Section 3.4.4 determines the maximum water difference between the water level behind and in front of the barrier for the design typhoon with a return period of 200 years. Each section results in the critical combination of the design typhoon, which can be different per section. For a return period of 200 years, different combinations of wind speeds and precipitation can occur, potentially resulting in a critical combination that defines the design typhoon. In each section, the method (Method 1 or Method 2) that leads to the most critical values is discussed.

In the 1D-model, it is assumed that the barrier closes 3 hours before the moment of landfall. In addition, the water level in the basin and in the bay is the same at the moment of closure. However, the 1D-model evaluating the storage capacity immediately subtracts the storage volume of the Arakawa River and catchment area $h_{r,storage}$. This explains the initial difference in water level height between $H_{basin}(t_0)$ and $H_{bay}(t_0)$. For both 1D-models the simulations of the 1D-model are halted at the end of the storm surge duration.

It should be noted that the backwater curve determining the water level of the Arakawa River as a result of the water level inside the basin is not considered. Consequently, the resulting water levels of the basin do not reflect whether the water level of the Arakawa River remains below its levees. Additionally, a potential wind-induced gradient in the water level behind the barrier, caused by typhoon-related winds, has not been investigated. This effect could lead to higher water levels at certain locations around the basin than those predicted by the model, potentially exceeding the levees. Yet, it could also result in lower water levels at the gate behind the barrier, potentially reducing the outflow.

Storage capacity evaluation

The possible combinations of wind speed and precipitation resulting from Table 3.23 for Method 1, the possible combinations of wind speed and precipitation for Method 2, and the observed combination of wind speed and precipitation during the proxy storm, Typhoon Hagibis (2019) are used as input in the 1D-model as as discussed in Section 3.4.3 to evaluate the storage capacity. As discussed in Section 2.4.3, each combination is evaluated for when the barrier closes at low, mid, and high tide. The resulting combination originating either from Method 1 or 2, leading to the highest water level behind the barrier during closure of the barrier and/or after it is opened again, results in the critical combination of a design typhoon when evaluating the storage capacity. The proxy storm is used to compare the resulting water levels of the critical combination with what the water levels would have looked like according to the 1D-model during the proxy storm.

Method 2 results in the highest water levels behind the barrier when comparing Figures 3.24 and 3.25. Consequently, a typhoon with a wind speed of 53.6 $[m/s]$ (95% CI: $[48.0, 56.1]$ $[m/s]$) and precipitation amounts of 45.9 $[mm/(6hr)]$ (95% CI: $[27.0, 71.1]$ $[mm/(6hr)]$) and 137.4 $[mm/(10hr)]$ (95% CI: $[121.1, 148.0]$ $[mm/(10hr)]$), as derived from Method 2, results in a peak discharge of the Arakawa River of 11221 $[m^3/s]$ (95% CI: [9890, 12087] $[m^3/s]$) and a storm surge height of 1.3 $[m]$ (95% CI: $[1.1, 1.4]$ $[m]$). This combination produces the highest water level behind the barrier during closure and independent of closure, reaching 4.1 $[m]$ and 4.3 $[m]$ respectively above T.P. when the barrier closes at high tide. This typhoon is therefore referred to as the critical combination of the design typhoon for evaluating the storage capacity at Location 7.

The levees will have a height of 6.73 $[m]$ above T.P. when the barrier is finished, as assumed in this report. From Figure 3.25, it can be concluded that the water level (including the 95% confidence bounds) stays well underneath the levees for the design typhoon under the design scenario of closing the barrier at high tide. Consequently, the 1D-model results suggest that Location 7 results in enough storage space such that the water level does not exceed the levees surrounding the basin during a design typhoon with a return period of 200 years. However, as the backwater curve is not considered, it remains uncertain whether the maximum water level in the basin will not cause the water level of the Arakawa River to exceed its levees.

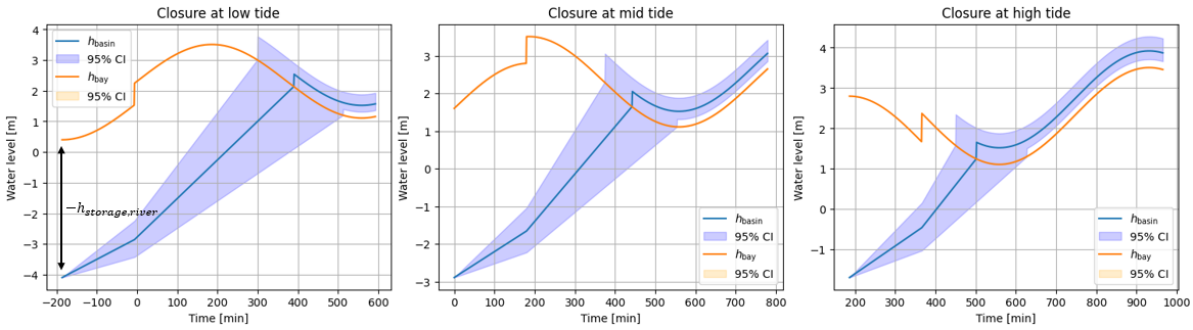

Figure 3.24: The critical combination following Method 1 leading to the largest water level according to the 1D-model, including its 95% confidence interval using $n = 1000$ bootstraps. In the model, the storage capacity of the river is subtracted from the water level in the basin at the start, as illustrated by $-h_{storage,river}$. As a result, the river storage is incorporated in the h_{basin} expressed in [m]. The water levels are shown in T.P.

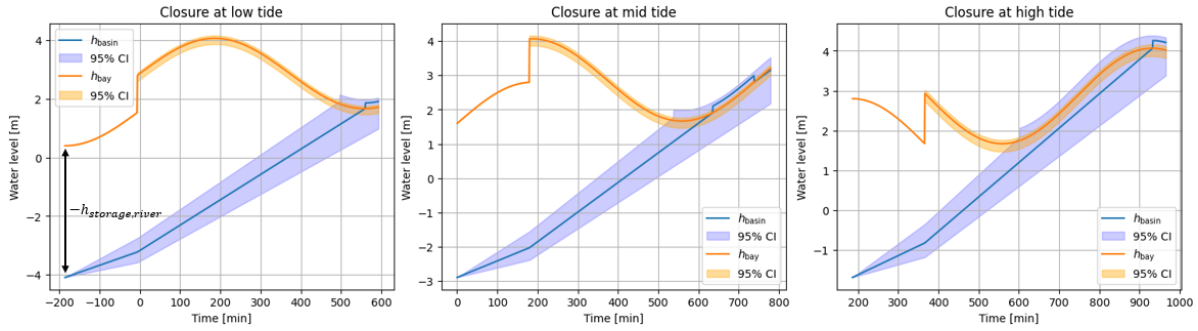

Figure 3.25: The critical combination following Method 2 leading to the largest water level according to the 1D-model, including its 95% confidence interval using $n = 100$ bootstraps. In the model, the storage capacity of the river is subtracted from the water level in the basin at the start, as illustrated by $-h_{storage,river}$. As a result, the river storage is incorporated in the h_{basin} expressed in [m]. The water levels are shown in T.P.

Proxy storm

According to the 1D-model in Figure 3.26, the water levels during typhoon Hagibis would have stayed underneath the levees with a height of 6.73 $[m]$ above T.P. when the barrier is finished, as assumed in this report. The scenario where the barrier is closed at high tide appears to be the critical scenario where the water level reaches 4.4 $[m]$ above T.P. in the basin. However, whether this is the critical scenario can be debated, as when closure would have occurred during the surge at low tide, the resulting water level inside the basin could have been lower during the closure period.

Note that the model run in Figure 3.26 consists of a jump just after the moment it passes mid tide. This jump stems from the simplicity of the model and is not representative of reality. The model tests whether $h_{basin,closed\ barrier}$ exceeds h_{bay} where after the gates can be opened. This occurs just after 600 minutes where Δh is added to $h_{basin,closed\ barrier}$ resulting in $h_{basin,open\ barrier}$ as explained in Section 2.4.4. Now the barrier can close again when h_{bay} exceeds $h_{basin,closed\ barrier}$, which happens just after mid tide. Moments later, $h_{basin,closed\ barrier}$ exceeds h_{bay}, such that the barrier closes again. The subsequent subtraction and addition of Δh is unrealistic, as the water level will not drop with Δh once the gates close. Furthermore, this scenario might be unrealistic due to the instant opening and closing of the gates, as in reality it likely takes longer. However, in this simple 1D-model, the barrier would never be able to close again once opened if $h_{basin,open\ barrier} \leq h_{bay}$ needs to be met, as $h_{basin,open\ barrier}$ always exceeds h_{bay} by Δh. Although this is not ideal, the approach is assumed reasonable in this report for a simple 1D-model providing preliminary insights in the water levels in front of and behind the barrier.

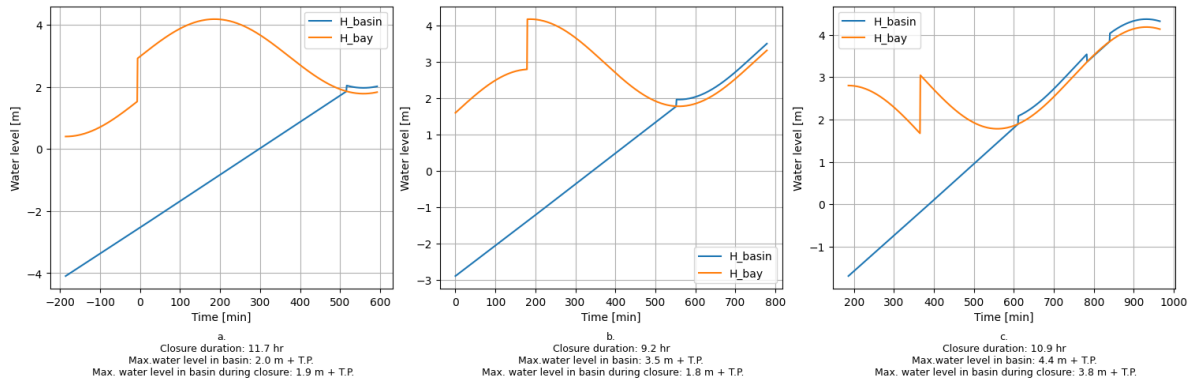

Figure 3.26: The 1D-model results for (a) closure at low tide, (b) closure at mid tide, and (c) closure at high tide for the proxy storm: Typhoon Hagibis. The water levels are shown in T.P.

In general, the scenario under which the gates close at high tide, 3 hours before landfall, appears to be the most important design scenario as it results in the highest water levels in the basin. However, this

should be interpreted with caution, as it can be debated whether the barrier should close 3 hours before landfall, as the tide is still in decline. Consequently, initiating closure at a later stage may result in substantially lower water levels within the basin, indicating that the scenario involving closure at high tide is of reduced significance.

Additionally, the maximum water level during the proxy storm exceeds the maximum water level resulting from the critical combination. This indicates that the storm surge relationship used in the model underestimates the storm surge height and likely results in too optimistic water levels following the design typhoon. Still, the water level during the closure period following the critical combination of the design typhoon does exceed the water level during closure of the proxy storm.

Maximum hydraulic load

To determine the maximum hydraulic load, the maximum water level difference between the water level in front of the barrier and behind the barrier should be found using the method for the 1D-model derived in Section 2.4.4 for determining the hydraulic load. Similar to Section 3.4.4, the possible combinations of wind speed and precipitation resulting from Table 3.24 for Method 1 and the possible combinations of wind speed and precipitation for Method 2 as discussed in Section 3.4.3 are used as input in the 1D-model. In addition, the observed storm surge and discharge during the proxy storm are used to determine what the hydraulic load would have been during that historic event. The resulting combination originating either from Method 1 or 2, leading to the highest water level difference between the water level behind the barrier and in front of the barrier or vice versa, results in the maximum hydraulic load and the corresponding critical combination of a design typhoon.

Method 1 gives the critical combinations when evaluating the hydraulic load. Event 1 in Table 3.24 considers the situation when the water level at the bay side is larger than at the basin side, $h_{basin,max} << h_{bay,max}$. In this scenario, the occurring wind speed is 58.4 $[m/s]$ (95% CI: $[50.0, 72.3]$ $[m/s]$) derived from Method 1, resulting in a storm surge height of 1.4 $[m]$ (95% CI: $[1.1, 2.0]$ $[m]$) with negligible precipitation. When the barrier closes at low tide, the head difference is equal to $\Delta h = 3.8$ $[m]$ (95% CI: $[3.5, 4.4]$ $[m]$).
Event 2 in Table 3.24 considers $h_{basin,max} >> h_{bay,max}$. Based on precipitation rates of 90.8 $[mm/(6hr)]$ (95% CI: $[49.0, 135.9]$ $[mm/(6hr)]$) and 277.5 $[mm/(10hr)]$ (95% CI: $[196.4, 378.7]$ $[mm/(10hr)]$), derived from Method 1, the peak river discharge of Arakawa River is equal to 22663 $[m^3/s]$ (95% CI: [16039, 30927] $[m^3/s]$) which results in a head difference of $\Delta h = 0.8$ $[m]$ (95% CI: $[0.4, 1.5]$ $[m]$).
Therefore, Event 1 gives the largest water level difference of all possible combinations evaluated, thereby producing the maximum hydraulic load on the barrier. Additionally, this combination between wind speed and precipitation is now referred to as the critical combination of the design typhoon when evaluating the maximum hydraulic load at Location 7

It should be noted that the resulting water level difference does not yet incorporate waves which can be of interest when dimensioning the barrier. Section 2.5 is about the dimensioning of the barrier, in this section the effect of waves on the maximum water level difference will be considered when designing components of the barrier.

Proxy storm

During the proxy storm, the observed storm surge and peak discharge would have resulted in the following hydraulic load when applying the method proposed in Section 2.4.4. The resulting hydraulic load when $h_{basin,max} >> h_{bay,max}$ equals $\Delta h = 0.8$ $[m]$ for a peak discharge of $11,000$ $[m^3/s]$. Additionally, the resulting hydraulic load when $h_{basin,max} << h_{bay,max}$ equals $h_{tidal\ range} + h_{surge} = 2.4 + 1.38 = 3.78$ $[m]$ when the barrier would have closed at low tide. Consequently, the largest hydraulic load on the barrier equals 3.78 $[m]$ when using the proxy storm.

Compared to the maximum hydraulic load derived using Methods 1 and 2, the proxy storm produces approximately the same hydraulic load, despite having a lower wind speed, higher atmospheric pressure, and a non-ideal wind direction as assumed in this report. These conditions would normally be expected to result in a smaller hydraulic head than that obtained from the critical combination of the

design typhoon. Consequently, the used relationship to estimate the storm surge in this report could be optimistically low.

For the preliminary design of the SSB, only the deterministic values will be considered due to time constraints. However, the results for the design typhoon and the 1D-model give an indication of the uncertainty inherent to determining what a typhoon, and consequent river run-off and storm surge, might look like in Tokyo Bay.

3.5. System design storm surge barrier

In this section, the results of the system design of the SSB are presented, corresponding to the methodology described in Section 2.5. Firstly, the obtained main system components and their functions are given. Secondly, the defined design parameters and navigational requirements are shown. Subsequently, the design of the navigational opening is presented. Finally, the suitable locations of the various barrier components are illustrated.

3.5.1. Main system components and functions

The SSB system is designed as a multifunctional hydraulic structure consisting of the following primary components:

- Movable (gated) barrier: Allows tidal exchange and navigation under normal conditions and closes during storm surges to prevent flooding.
- Fixed (ungated) barrier: Provides permanent resistance against high storm surges and wave forces.
- Environmental and ecological facilities: Maintain habitat connectivity and minimize environmental impacts.
- Supporting structures: Transfer loads from barrier components to the foundation, ensuring structural stability.
- Control and operating systems: Manage gate operations while monitoring structural and mechanical performance.
- Scour protection: Prevents erosion of the seabed and foundations caused by strong currents and turbulence.
- Access and maintenance facilities: Provide safe access for inspection, repair, and operational activities.

The results of the 1D show that the storage basin provides enough capacity for the inflow of the river discharge, hence, no additional pumps are required, see Section 2.4.

3.5.2. Design parameters

It is concluded that the highest hydraulic loads act on the barrier when the largest head difference exists across the barrier, hence when the water level in Tokyo Bay is at its maximum and the water level in the basin is at its minimum, as discussed in Section 3.4.4. The design condition with the highest head difference between the two sides of the barrier is the one with a 1/200 [year] wind speed and 1/1 [year] precipitation, and thus, 1/200 [year] storm surge.

Table 3.1 shows that Location 7 has a maximum depth of 18 $[m]$ and an average depth of 12 $[m]$. For the calculations of the dimensions of the structural components, it is assumed that the seabed is located at a depth of 15 m.

In Table 3.25, the design parameters as well as the results of the significant wave height (Equation 2.39), peak wave period (Equation 2.39), and maximum wave height (Equation 2.40) are presented.

Parameter	Symbol	Value	Unit
Highest astronomical tide	HAT	1.2	$+m$ T.P.
Lowest astronomical tide	LAT	-1.2	$+m$ T.P.
Depth of sea bed w.r.t. T.P.	d_{sb}	15	m
Storm surge	SS	1.4	m
Sea level rise	SLR	1.6	m
Wind speed	U_{10}	58.4	m/s
Maximum fetch length	X	21	km
Significant wave height	H_s	4.38	m
Peak period	T_p	7.19	s
Maximum wave height	H_{max}	7.02	m
Design water level	DWL	4.3	$+m$ T.P.
Design low water level	DLWL	0.4	$+m$ T.P.

Table 3.25: Design parameters.

The peak tidal discharge is determined using Equation 2.41 with the following input parameters for Location 7: a period of 6 $[hr]$, a storage area of 80 $[km^2]$ and a a tide of 2.4 $[m]$ (found in Section 3.4.1). This results in a tidal volume of 192 $[hm^3]$ and a peak tidal discharge of 27925.27 $[m^3/s]$ according to Equation 2.41.

3.5.3. Navigational requirements

Accordingly to Section 2.5.3, the navigational requirements for future shipping are determined.

Current and future shipping activities

Currently, according to of Port and Harbor (2020) the Y2 berth at the outer central breakwater terminal has a depth of 16 $[m]$ and a length of 400 $[m]$, these are the specifications of a megamax-23 ship. Berth Y3 is still undergoing construction, and no information on its dimensions could be found (Tokyo Port Terminal Co., 2024).

Looking ahead, vessel dimensions are expected to increase. Ueda et al. (2025) projects that the maximum container ship size will likely reach the 27,000 TEU class. To account for this, the navigational gate and waterway are designed to accommodate future Gigamax-25 vessels with a length L_s of 425 $[m]$, beam width W_s of 63 $[m]$, and draft D_s of 17 $[m]$ (Ueda et al., 2025). The assumption is made that ships will be traveling at a speed of 7 $knots$, which is slow according to PIANC – The World Association for Waterborne Transport Infrastructure (2014).

It is estimated that approximately 500 ships transit Tokyo Bay each day (Tokyo Bay Waterway Office, 2015). For the purpose of this analysis, it is assumed that a third of this number also passes through Tokyo Harbor, corresponding to about 170 vessel movements in total and 85 in each direction (coming in and going out) per day. This number is likely an overestimation but provides a conservative basis for planning. The location of the gates in the barrier is planned to be in the center of the current navigation channel.

Navigation depth

The minimum required channel depth d_{nav} follows from Equation 2.42 with the following input parameters:

$$\begin{aligned} \zeta_{tide} &= 0 \ [m] \text{(assumption)} \\ s_{max} &= 0.085 \ [m] \\ \zeta_m &\approx 2 \cdot H_s = 1.5 \ [\text{m}] \ ^1 \\ s_s &= 1.15 \ [m] \text{(assumption)} \end{aligned}$$

s_{max} is found using Equation 2.43 with the following parameters:

$$\begin{aligned} C_B &= 0.69 \text{ from [1] follows for Gigamax-25} \\ K &= 1 \text{ unrestricted channel is assumed} \\ V &= 7\ [kn] \text{ assumed vessel speed} \end{aligned}$$

[1]: PIANC – The World Association for Waterborne Transport Infrastructure, 2014.
This results in a sinkage due to squat S_{max} of 0.085 $[m]$.

To conclude, the required navigational depth is 19.75 $[m]$. Since this condition must be satisfied during low water tide as well, the required depth for the sill of the gates d_{sill} is 20.95 $[m]$.

Navigation width

The minimum required span of the gates (W_{min}) is calculated using the equations mentioned in section 2.5.3.

To determine the "W-factors", it is assumed that the prevailing cross-winds, prevailing cross-currents and prevailing longitudinal currents are mild, negligible and low, respectively. Besides, a slow ship speed is considered, as mentioned in Section 3.5.3. This results in the "W factors"that are presented in Table 3.26.

Table 3.26: Width components and amplification factors.

Width component	**Condition**	**Amplification**
Basic width for maneuverability W_{BM}	Good maneuverability	1.3
additional Width W_i		
Ship speed	Slow	0.0
Prevailing cross-wind	Mild	0.3
Prevailing cross-current	Negligible	0.0
Prevailing longitudinal current	low	0.0
Prevailing wave height	<1 m	0.0
Aids to navigation	Excellent	0.0
Bottom surface	$< 1.5 \cdot D_s$, and rough/hard	0.2
Depth waterway	$< 1.25 \cdot D_s$	0.2
Cargo hazard	High	1.0
Width for passing distance W_p		
Vessel speed	Slow	1.2
Encounter traffic density	Heavy	0.5
Bank clearance $W_{BR} = W_{BG}$	Steep and hard structures	0.5

Applying these factors in Equation 2.44 and in Equation 2.45 results in a width of 236 $[m]$ for two smaller openings with one shipping lane each (one opening for incoming vessels and one opening for outgoing vessels), or one big single opening of 548 $[m]$ with two shipping lanes (one lane for incoming vessels and one lane for outgoing vessels), respectively. This result is unexpectedly large and seems to provide very conservative widths. Therefore, it is assumed that a width of 4 to 6 times the width of the design vessel for a single gate with a two way channel leads to more realistic numbers. Accordingly, this results in a navigational width of 252 to 378 $[m]$. It is decided to design a gate of 350 $[m]$ wide, which is closer to the higher end of the gate width range.

Verification of shipping intensity

It is assumed that a service day is 24 hours and all boat movement is spaced equally over time, and over both lanes. As mentioned in Section 3.5.3, 85 vessels in each direction are expected per day. The assumption was made that the ships would be sailing at 7 $[knots]$ (3.61 [m/s]). This results in an available spacing distance $L_{available}$ of 3715 $[m]$ (Eqaution 2.47).

As mentioned, L_s is defined as 425 $[m]$, providing a minimum required distance of 1040 $[m]$ between the fronts of two vessels using Equation 2.48. From Equation 2.46 it can be concluded that the capacity of the navigation channel is more than sufficient to handle the traffic intensity.

3.5.4. Suitable locations of the barrier components

The barrier alignment is located between Haneda Airport and the residential area near Disneyland Tokyo. This location provides the shortest feasible span (11,750 $[m]$) while maximizing the storage capacity behind the barrier to store river discharge from the Sumida, Arakawa, and Kyuedo Rivers.

The location avoids direct interference with the tidal flats in the northeastern part of Tokyo Bay and allows reinforcement of unprotected waterlines with embankments (indicated by green lines in Figure 3.27).

To minimize disruption to existing ferry and cargo routes, the navigational gates are positioned slightly south of the centerline (red dashed line in Figure 3.27). The flow inlets are evenly distributed over the ungated barrier to maximize tidal exchange throughout the whole storage basin.

Figure 3.27: Indicative map of Tokyo Bay near Tokyo City.

3.6. Component design storm surge barrier

In this section the conceptual design for the navigational gate design is presented, as well as the key dimensions for the gated flow inlets and ungated barrier.

3.6.1. Gate design

This subsection presents the results of the methodology for establishing the gate design as described in Section 2.6.1.

Gate type

Section 3.5.3 shows that the span of the navigational opening needs to be 350 $[m]$. From Section 3.6.1, a required gate height of 32 $[m]$ is found. The assumption is made that the requirement can be met by all selected gate types, even though it's significantly higher than current real-world examples of said types. The following gate types from Mooyaart and Jonkman (2017) meet the requirements established in Section 3.1.4. High priority was given to navigation.

- Sector gate
- Flap gate
- Inflatable gate
- Rotary Segment gate

The characteristics of these gate types are presented in Appendix L.

MCDA

Table 3.27 presents the final weighted MCDA results.

Table 3.27: Final result of the MCDA for the gate type of the SSB, combining the qualitative scores per criterion with their associated weight.

Criteria	Sector Gate		Flap Gate		Inflatable Gate		Rotary Segment Gate	
	S	S*W	S	S*W	S	S*W	S	S*W
Ease of construction	4	1.2308	2	0.6154	2	0.6154	1	0.3077
Required space [m^2]	1	0.0833	5	0.4167	5	0.4167	3	0.2500
Ease of maintenance	4	1.0000	1	0.2500	1	0.2500	4	1.0000
Adaptability	2	0.3333	4	0.6667	3	0.5000	1	0.1667
Operation Time	2	0.3333	5	0.8333	1	0.1667	3	0.5000
Total		3.3077		3.4615		1.6154		3.0000

The flap gate ranks as the most favorable option overall, offering a balance between constructability, spatial efficiency, and adaptability. Its main drawbacks include the need for underwater maintenance and potential sediment buildup. Future work should investigate its durability and maintenance strategy under Tokyo Bay conditions. The detailed explanation of the MCDA can be found in Appendix K

Dimensions gate

Figure 3.28 presents an illustration of a possible gate design of the flap gate and the different water depths with respect to the sill level. The different water levels considered in the design are summarized in Table 3.28. Each level is expressed relative to both the sill level and Tokyo Peil (T.P.).

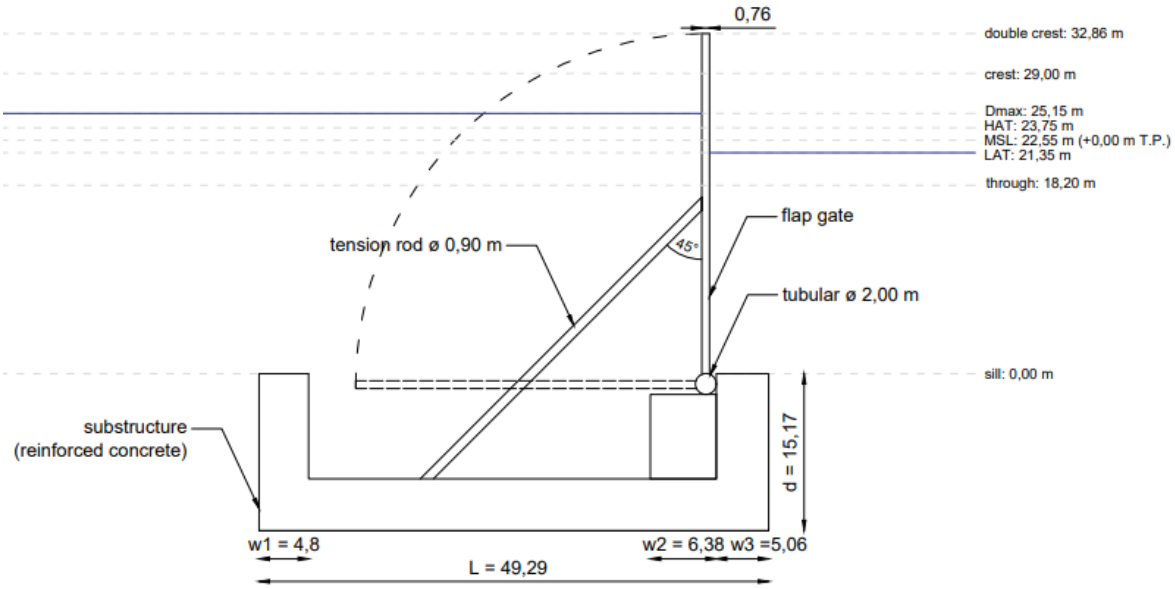

Figure 3.28: A possible gate design of the flap gate (side view).

Table 3.28: Water levels relative to sill level and Tokyo Peil.

Water level description	**Water level** $[m]$ **+T.P.**	**Depth w.r.t. sill level** $[m]$
MSL	0.00	20.95
Sill level	-20.95	0.00
Wave trough level	-4.35	16.60
LAT	-1.20	19.75
HAT	1.20	22.15
DWL/D_{max}	4.30	25.15
DWL/D_{max} + Crest	8.15	29.00
DWL/D_{max} + 2 × Crest	12.01	32.86

Below, the obtained dimensions of the main components are explained. The remaining dimensions were assumed based on the height-to-width ratios of the Kanadevia flap gate design (Coastal Technology Research Center, 2020). All ratios and calculations are presented in Appendix M. For a preliminary estimate of the gate's plan dimensions, the height-to-width ratio of 1.625 of the Kanadevia flap gate is adopted. Applying this ratio to the design length of 32.86 $[m]$, obtained in Section 3.5.2, yields an estimated width of 20.22 $[m]$. Over the total navigational opening length of 350 $[m]$, this corresponds to 17.3 gates, which is rounded up to 18, resulting in a total navigational width of 363.96 $[m]$.

For a first estimate of the flap gate design, the entire gate span is divided into individual flap gates with dimensions of 32.86 $[m]$ in height and 20.22 $[m]$ in width. Each flap gate consists of a skin plate that serves to retain the water. The load transfer occurs through three main circular vertical beams, positioned at both sides and in the center of the gate. Between these circular vertical beams, circular horizontal sub-beams are installed to transfer the forces from the skin plate to the main beams. Vertical girders are placed between the horizontal sub-beams to act as stiffeners and increase the local rigidity of the structure. Between each pair of circular vertical main beams, two tension rods are installed at an angle of 45°, connected to a circular horizontal sub-beam located at mid-height of the flap gate. This circular horizontal sub-beam should be designed with sufficient strength to transfer and resist the forces induced by the tension rods. A horizontal tubular beam with a diameter of 2 $[m]$ is assumed as the main beam connecting the gate to the hinges on the substructure. For a preliminary design, rough estimations of the dimensions are given to the four main components.

Main beam

Three vertical circular main beams, each with a length of 32.86 $[m]$ are used in the design of the flap gate. Using Equations 2.49 and 2.50, the diameter and thickness of the circular main beams are, respectively, 0.75 $[m]$ and 0.03 $[m]$.

Sub beam

Ten horizontal circular sub beams, each with a length of 20.22 $[m]$ are used in the design of the flap gate. Using Equation 2.49, the diameter of the circular sub beams is 0.24 $[m]$. Using Equation 2.50, the calculated thickness is 0.01 $[m]$.

Girder

Eight vertical circular girders, each with a total length of 32.86 $[m]$ are used in the design of the flap gate. The girders are connected to the horizontal circular sub beams and therefore not entirely continuous, however, this can be seen as a system of sub girders. The length of each sub girder is equal to the spacing of the sub beams, 2.022 $[m]$. Using Equation 2.49, the diameter of the circular sub beams is 0.08 $[m]$. Based on Equation 2.50, the calculated thickness is 0.003 $[m]$.

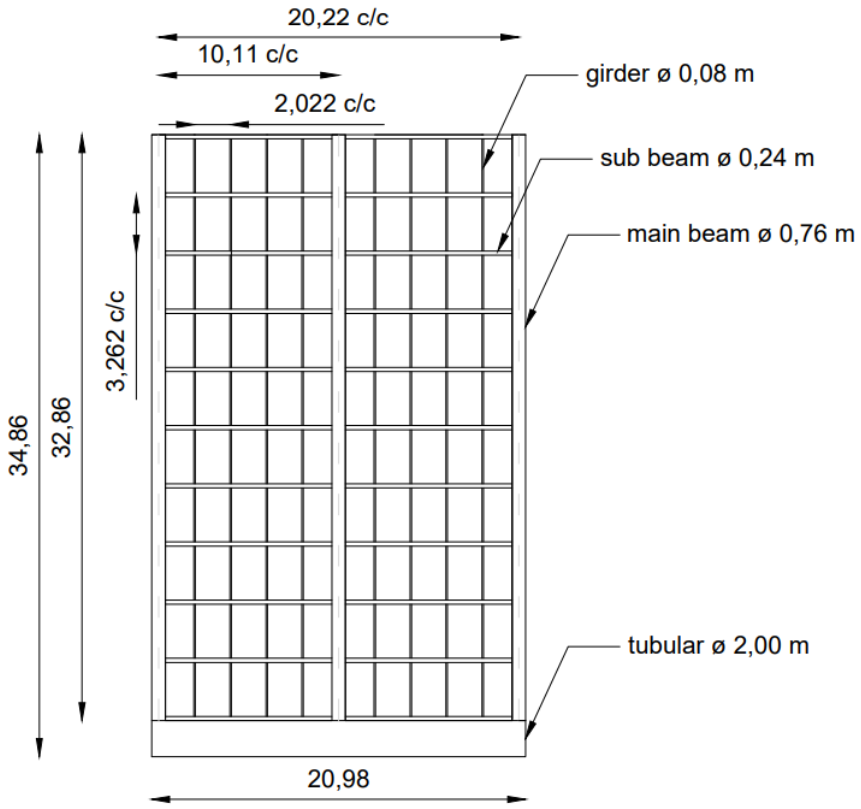

Figure 3.29: A possible gate design of the flap gate (front view).

Skin plate

A thickness of 0.025 $[m]$ is assumed for a first design of the skin plate. This is slightly larger than a thickness of 0.019 $[m]$ which is used for the skin plate at the current Kanadevia flap gate. The skin plate has a total area of 664.4 $[m^2]$.

Table 3.29 presents, for each flap gate component, the total length, outer diameter, and thickness.

Table 3.29: Summary of gate component dimensions.

Component	Length [m]	D_{out} [m]	Thickness [m]
Main beam	98.58	0.76	0.03
Sub beam	202.21	0.24	0.02
Girder	230.01	0.08	0.003
Skin plate	-	-	0.025

Substructure

The guiding example substructure of the Kanadevia flap gate has a height and depth of 19.5 $[m]$ and 6 $[m]$, respectively, for a gate height of 13 $[m]$. For a first estimation of the substructure length for the Tokyo Bay barrier, the ratio between gate height and substructure length is assumed to be similar. This assumption may result in either an over- or under-dimensioning of the substructure. The ratio is 0.67. The length of the substructure of the Tokyo Bay flap gate is estimated as 49.29 $[m]$.

The length-to-depth ratio of the substructure of the Kanadevia flap gate is 0.31. The depth of the Tokyo Bay gate is estimated to be 15.17 $[m]$, accordingly.

Other horizontal dimensions are obtained via the same length ratio approach of the substructure. These horizontal dimensions are calculated in Appendix M, and are shown in Figure 3.28.

Loads on gate

Using the design parameters defined in Table 3.25, and obtained preliminary dimensions of the flap gate, the applied loads are estimated. The loads are projected in the coordinate system, where positive horizontal forces act to the right, vertical forces act upward, and positive moments act counterclockwise. Figure 3.30 shows all the applied loads on the gate and the substructure.

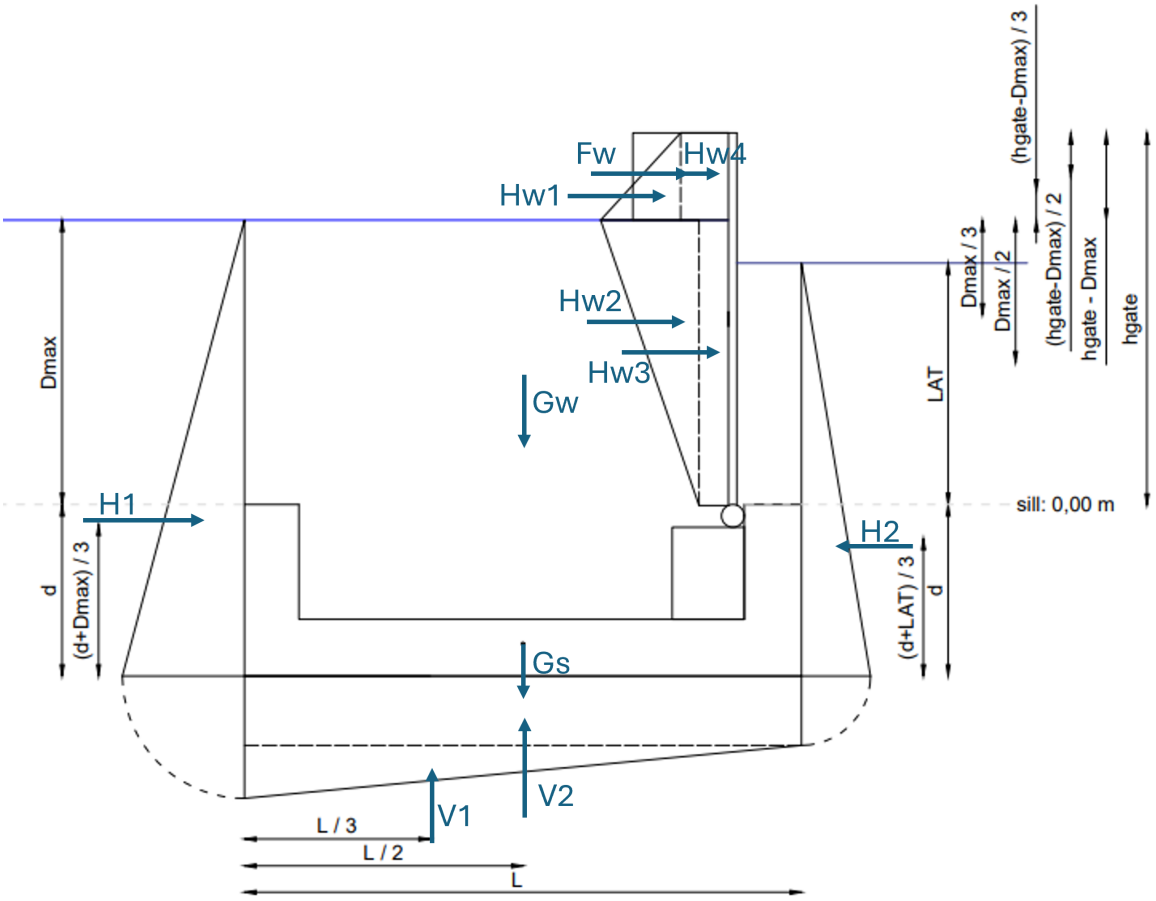

Figure 3.30: Acting loads on the gate.

Table 3.30 and 3.31 present an overview of the magnitude of respectively the different horizontal and vertical loads. All load calculation are presented in Appendix M.

The largest horizontal loads are the hydrostatic pressures acting on both sides of the gate. The contribution of the total wave load, amounting to 917 $[kN]$, is approximately half of the total resulting horizontal load. The wind load contributes significantly less to the total resulting horizontal load in respect to the other horizontal loads. In determining the horizontal loads, the friction force is not taken into account. If the friction force is larger than the resulting horizontal load, the structure refrains from moving. The friction force should be larger than the total horizontal load of 2394 $[kN]$ to prevent the structure from moving.

The largest vertical load is the total hydrostatic vertical load (19039 $[kN]$), followed by the weight of the water above the substructure (-12464 $[kN]$) and the self-weight of the substructure (-9431 $[kN]$). The total vertical force is negative, meaning that the self-weights keeping the structure in place are larger than the uplifting forces.

Table 3.30: Horizontal loads for SLR = 1.6 [m].

Load component	Symbol	Magnitude [kN/m]
Hydrostatic pressure for depth $D_{\max}$	H_1	8172
Hydrostatic pressure for depth LAT	H_2	−6704
Wind load (crest to double crest)	F_w	8.1
Wave load – surface component	H_{w1}	95
Wave load – intermediate component	H_{w2}	441
Wave load – bottom component	H_{w3}	338
Wave load – top component	H_{w4}	43
Total horizontal load	$\mathbf{H_{tot}}$	**2394**

Table 3.31: Vertical loads, self-weight, and buoyancy for SLR = 1.6 [m].

Load component	Symbol	Magnitude [kN/m]
Hydrostatic vertical component (upper)	V_1	942
Hydrostatic vertical component (lower/LAT)	V_2	18097
Weight of flap gate (averaged over width)	G_{flap}	−229
Weight of water above substructure	G_{w}	−12464
Weight of substructure	G_{s}	−9431
Buoyancy of flap gate (averaged over width)	V_b	35
Total vertical load	$\mathbf{V_{tot}}$	−3051

3.6.2. Flow inlets

In this preliminary design, the gate type for the flow gate follows from the navigational gate type, which is a flap gate. All flow inlets are assumed to have a depth of -15 $[m]$ T.P. to simplify calculations.

Using the method described in Section 2.6.2 and the peak tidal discharge equal to 27925.27 $\left[\text{m}^3/\text{s}\right]$ from Section 3.5.2 the required cross-sectional area is calculated to be 18616.85 $\left[m^2\right]$. The cross-sectional area of the navigation gate (6912.5 $\left[m^2\right]$) found by multiplying the span (350 $[m]$) and depth of the navigation gate (19.75 $[m]$) from Section 3.5.3 and Section 3.5.3 respectively is subtracted from this required cross-sectional area. The resulting area (11704.35 $\left[m^2\right]$) is divided by the depth of the gate (15 $[m]$). The resulting length of 780 $[m]$ is the required length of 15 $[m]$ deep flow inlets to allow shipping for Location 7. The flow inlets are assumed to have the same individual flap width as the navigational gate flaps (20.22$[m]$). The gate of the flow inlet is assumed to reach the same level of +12.01 $[m]$ T.P. from Section 3.6.1, resulting in a total height of 27.01 $[m]$

3.6.3. Ungated barrier

This subsection presents the geometrical results of the horizontally composite caisson. Figure 3.31 shows the key dimensions of the ungated barrier.

Armour unit body

The freeboard crest height R_c is 6.53 $[m]$ and the wave angle influence factor γ_b is 0.81, resulting in a crest level h_{crest} of $10.73 \approx 11.0[m]$. The armour unit body base width B_{aub} is 43.5 $[m]$.

Caisson

The crest level of the caisson equals the crest level of the armour unit body, hence 11 $[m]$.

From the rotational stability, it is found that the minimum width is 3.48 $[m]$; from the rotational stability, a minimum width of 11.70 $[m]$ is found, and from the vertical stability, it is concluded that the caisson can not be wider than 30.53 $[m]$. Taking into account that secondary functions are desired to be implemented into the design, a caisson of 30 $[m]$ is chosen for this preliminary design.

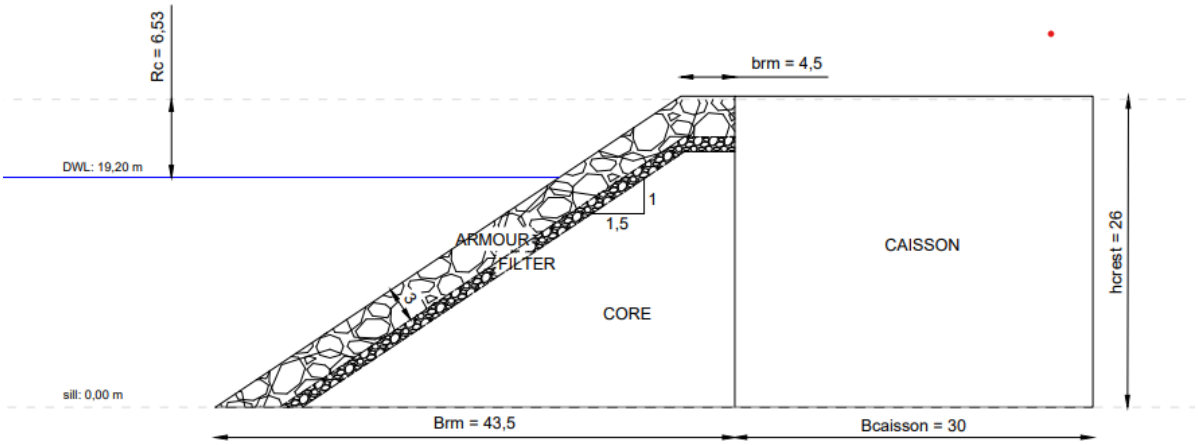

Figure 3.31: Dimensions of ungated barrier (horizontally composite caisson).

The design of the armour unit body requires further verification against key geotechnical and hydraulic failure modes, including armour layer stability under design wave loading, proper filter layer gradation and permeability, and toe stability. Additionally, the availability of armour rock near Tokyo should be confirmed to validate the constructability and cost assumptions of the proposed design.

Regarding the required crest height of the ungated barrier, results show that the required freeboard crest height is of great influence compared to storm surge. The calculated freeboard height of 6.53 $[m]$ is substantially larger than the storm surge level of 1.4 $[m]$, indicating that the crest height is highly sensitive to the local wave conditions associated with the 200-year return period wind speed U_{10}. This suggests that the influence of wind-generated basin waves is dominant in calculating the required crest height. It is recommended to perform a sensitivity analysis of overtopping discharge limits, wave boundary conditions, geometrical design choices, and design return periods to confirm that this crest height is reasonable.

The caisson design also requires further exploration. The friction coefficient at the caisson-foundation interface and bearing capacity of the soil are currently based on limited soil information. A detailed site investigation is required to acquire reliable horizontal and vertical stability assessments. Besides, the settlement of the soil should also be researched. Furthermore, currently, a caisson width of almost twice the minimum required width is chosen. A smaller width could be chosen, resulting in less required material, lower costs, and likely making the caisson easier to construct.

3.7. Design overview and adaptation

This section describes the design configuration of the proposed SSB. Besides, possibilities of secondary functions are given and, finally, it is explored how the design could be adapted to account for uncertainties in predictions of climate change.

3.7.1. Design overview

In Figure 3.32, the results of the system and component design are visualized. The navigational gate is located where the current left navigational channel is located. The flow inlets are dispersed across the barrier length in groups of four.

Because multiple parallel flap gates are used for both the navigational opening and the flow inlets, partial redundancy is incorporated into the design, but full redundancy is not achieved. This is in line with other existing barrier systems since most only have one navigational opening. Should one or several gates malfunction, the impact is assumed to remain limited, as the other flaps are assumed not to be impacted by this malfunction, and any flow through partially open gaps is assumed to be small. If some gates fail to open again after being closed, navigation is assumed to still be possible around

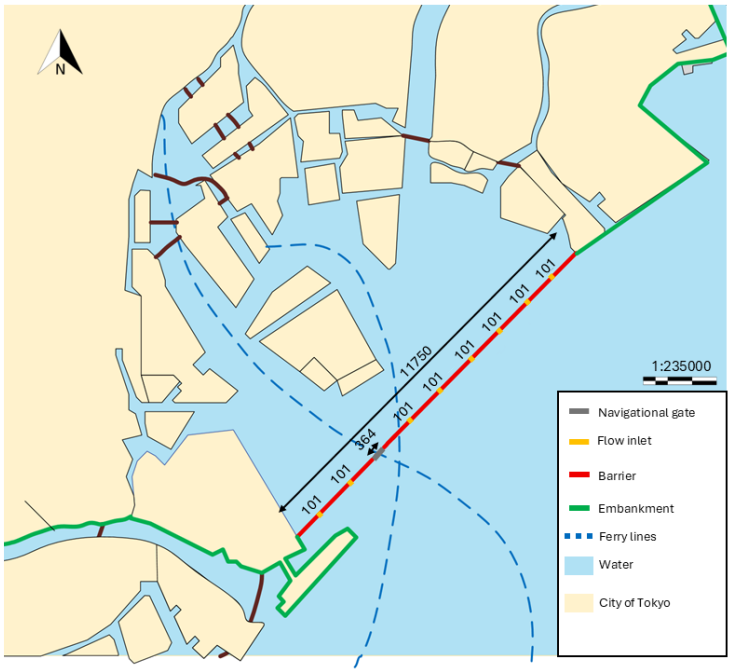

Figure 3.32: Overview design of the barrier for Tokyo Bay.

them. No further considerations regarding redundancy are made since this is out of the scope of this preliminary design.

3.7.2. Secondary functions

In order to derive the secondary functions, the Afsluitdijk and Eastern Scheldt barrier situated in the Netherlands are used as reference projects. In addition, exploratory ideas of stakeholders and Japanese scholars, and emerging technologies are used as inspiration for possible functions.

In well-known engineering works like the Afsluitdijk and Eastern Scheldt barrier in the Netherlands, the barrier is not exclusively used to hold back water, but also as a transport link. The Eastern Scheldt barrier is a 9 $[km]$ long barrier that connects two islands in Zeeland, the Netherlands, by a two-way road for vehicles (Rijkswaterstaat, 2025b). In addition to its infrastructure function, the Eastern Scheldt barrier also generated renewable energy, since five turbines were installed within the structure that produced electricity from tidal currents between 2015 and 2023 (Rijkswaterstaat, 2015).

The Afsluitdijk is a dam in the north of the Netherlands. With a length of 32 $[km]$, it connects two provinces in the Netherlands (Rijkswaterstaat, 2025b). The link consists of four lanes designated for vehicles and a separate lane designated for bikes. Besides serving as a transportation link, the Afsluitdijk minimizes ecological damage by incorporating a sluice designated for fish. The sluice allows fish to travel safely between the ocean and the basin (Rijkswaterstaat, 2025a).

Secondary functions explored by Japanese scholars are focused on urban development. Tsuchiya (2024) proposed a storm surge levee for Tokyo that creates a maritime city, as the “International Urban Area of Tokyo”. Additionally, the embankment of the storm surge levee could serve as a garbage disposal site (Tsuchiya, 2024)(Daily, 2024). Another proposition for a barrier for Tokyo Bay, by Ohta (2024), consists of residential areas, expressways, high-speed rail, subway lines, 50 $[m]$ wind turbines, and a hydroelectric power plant (Ohta, 2024).

The idea of creating a marine city with a residential area is also explored for Jakarta by the NCICD program. This plan consists of a sea dike located 50 to 100 $[m]$ from the mainland. The space between the sea dike and mainland will be nourished with sand to accommodate public infrastructure and residential areas for fishing communities. The seaside of the barrier will include mangroves to push ecological conditions (Suprayogi et al., 2018).

The preliminary design of the SSB, as proposed by this report, can include infrastructural, ecological, residential, and energy generation components as secondary functions similar to the ideas and reference projects mentioned above. However, as the current design consists of a caisson in combination with flap gates, the solution space for secondary functions is reduced. As an example, a flap gate limits the possibilities for a transportation link via the surface of the barrier. An alternative could be the construction of a tunnel or a bridge.

The barrier proposed by this report could include residential areas, predominantly constructed behind the barrier. Forms of residential areas can include floating cities. Additionally, ecological opportunities include the development of an artificial reef on both sides of the barrier and tidal flats within the basin, thereby replacing current tidal flats potentially lost under SLR.

Other secondary functions can include port expansion, as the vertical wall of the caisson can be designed to fit the purpose of a berth and, at the same time, convert wave energy, a design proposed by Wavenergy.it S.r.l., 2014. Opportunities for energy generation can also be found by the inclusion of ocean current turbines like those designed by Equinox, which can produce tidal energy at low flow speeds (Equinox Ocean Turbines, 2025).

3.7.3. Adaptation

The SSB is proposed for a design life of 150 years. However, the next decades pose large uncertainties due to climate change. This preliminary design does not incorporate climate change effects on typhoons, and assumes a deterministic value for sea level rise. To cope with these uncertainties, an adaptable design is proposed for the barrier.

To obtain a modular design, the substructure of the gate can be designed such that multiple gate sizes can fit and be installed. Sea level rise may be larger than forecasted by the SSP3-7.0 & 1.6 scenario, and larger gates may be needed to withstand future typhoon events. Additionally, the foundation for the caisson can be constructed such that in case the barrier height needs to increase, the foundation is able to hold the extra force applied. Another option is to include adjustable or extendable segments in the caisson that can be raised in case typhoons intensify in the future which could lead to higher storm surges.

Furthermore, the increase of rainfall intensity during typhoons should be considered which could results in higher water levels inside the basin. An adaptable solution could be to keep space available in the system design for drainage systems or pumps. This could lower the water levels in the basin if the storage capacity appears insufficient in case of high river discharges and a high storm surge.

As mentioned in Section 3.1.4, the design should include measures to improve the ecology in the basin and on the seaside of the barrier. Artificial reefs can help reduce wave impact if waves during typhoons increase in size due to more intense typhoons induced by climate change (Xu et al., 2025). Consequently, an artificial reef can reduce the storm surge whilst simultaneously improve the ecology of Tokyo Bay.

Adaptability should not only be included in the barrier, but also in the city development. The large river discharges in the Tokyo Bay are a result of intense rainfall, but also the result of large run-off rates within the City of Tokyo. The surface is highly paved, and little green spaces are found within the city, which means that most water is discharged directly into the river via the surface or drainage systems, and little can infiltrate into the soil. If more water would infiltrate into the soil, the run-off rates and consequent river discharge levels would decrease. A more integrated urban approach can increase green areas and, consequently, enhance infiltration rates. This can be achieved through measures such as green roofs, additional green spaces like rain gardens, trees in the streetscape, and rainwater storage systems. The first three measures also help mitigate the urban heat island effect, as green spaces provide measurable cooling effects on average temperatures. An example of how to increase rainwater storage using an integral approach can be found in Sumida City, which began rethinking the use and storage of water in 1982. By installation of rainwater storage tanks in government buildings and private residences the water storage was increased whilst it could simultaneously be used for fire-fighting and daily life (Hori, 2024).

4

Discussion

In this chapter the results are interpreted in the context of the project objectives, and potential implications and limitations of the findings are identified.

The main objective of this report is to provide preliminary recommendations for a SSB to protect Tokyo Bay, and specifically the city of Tokyo, from flooding associated with typhoons. These recommendations are based on an analysis of the bay's boundary conditions, an assessment of the most promising location for the barrier, and a probabilistic analysis to determine the design typhoon, resulting in the modeling of the expected water levels in the basin, which allowed for a preliminary dimensioning of the barrier.

The boundary condition analysis resulted in the functional requirements used throughout the research. However, only high-over analyses were performed, and only a limited number of interviews were conducted. Consequently, the boundary conditions and functional requirements only give an indication of what important functional requirements might be.

Following the boundary conditions and functional requirements, a MCDA is conducted. The MCDA results in the most promising location for the SSB at Location 7, connecting Haneda Airport and the Tokyo Disneyland area. The chosen location is supported by a simplistic additional cost-property value analysis that is based on a rough estimation of the possible barrier costs and the property values of the protected areas. However, the established relationships used to score the locations on different criteria were highly simplistic and based on a lot of assumptions. The pairwise ranking to weigh the different criteria could still include some degree of subjectivity. Besides, including more or different criteria could lead to different outcomes of the MCDA. As a result, the applied method and resulting location of the barrier only give a suggestion of what a promising location could be. Furthermore, political considerations were not included in the criteria, which could favor a different barrier location.

The design typhoon is estimated using two methods, both leading to slightly different combinations of typhoon parameters, such as wind speed and precipitation, for a return period of 200 years. However, the wind speed is modeled on rounded data, which could lead to biased results. Moreover, Method 2 only considers 13 data points, which could result in a bad fit of the copula. Furthermore, the fit is not validated using official metrics, as such the resulting combinations of typhoon parameters following Method 2 could be biased. Yet, the resulting values of Method 1 are comparable to the obtained values from Method 2, substantiating the findings. The lack of data originates from using the GPD of the POT to model extremes. By not only considering typhoons that made landfall in Tokyo with wind speeds 18 hours prior to landfall exceeding 37 $[m/s]$, more data points can be included, which can result in a better fit.

The analysis of the storage capacity using the 1D-model suggests that the barrier could provide effective protection for Tokyo under the critical combination, including its 95% confidence interval, following the design typhoon from Method 2, as the water levels in the basin would remain below the levees. Next to that, the maximum hydraulic load is found under the critical combination following the design typhoon derived in Method 1.

However, the water level results of the model are very preliminary. Firstly, the backwater curve of the Arakawa River is not considered. Consequently, the water levels inside the Arakawa River could exceed its levees, whilst the model shows that the water levels in the basin do not exceed its levees. Secondly, a very simplistic hydrological model is used to determine the river discharge during a typhoon. As a result, the credibility of the derived discharges remains uncertain. Thirdly, the Horikawa relationship used to determine the storm surge appears to be too optimistic, resulting in an optimistically low storm surge when comparing the critical combination results with the observed storm surge during the proxy typhoon.

Besides the backwater curve, hydrological model, and the storm surge relationship, the model does not account for complex river-sea interactions, multidimensional hydrodynamic phenomena, tidal reduction effects, detailed barrier design, including the selected flap gate mechanism, the existence of the flow inlets, the closure timing, and trigger mechanisms. In conclusion, the 1D-model could result in biased results for the water levels behind and in front of the barrier, however the water levels can serve as a preliminary indication.

Additionally, climate scenarios have only been considered in the evaluation of sea level rise, so the impact on typhoons and related processes is not included.

Furthermore, given the preliminary indication of the SSB's protective potential, initial dimensions for the main barrier components are developed, and a conceptual overview of the overall barrier system is established. However, this represents a very simplified preliminary design, based on numerous assumptions and without detailed modeling. As such, it should be considered a first-order estimate of the potential configuration of the barrier components and the overall system.

Firstly, the subsoil conditions at the proposed location have not been investigated thoroughly, which limits the reliability of conclusions related to the optimal gate location and stability of the structural components. Besides, potential long-term settlements must be quantified and be taken into account while determining the required gate and crest height of the barrier.

Furthermore, the design does not consider dynamic forcing or other natural hazards such as tsunamis and earthquakes, which are highly relevant for Tokyo. These hazards could compromise the barrier's functionality before or during a storm surge event if not properly accounted for in the design. Including these aspects in the design could lead to different required dimensions to sustain the accompanying forces.

With respect to navigational requirements, assumptions have been made about future shipping characteristics. While historical trends suggest growth in vessel dimension, technological and political developments tend to imply that it is likely that more investments will be done on electrical-powered shipping and less manpower it is probable that investments will be done in electrically powered and autonomous shipping, likely resulting in smaller vessel size, but more frequent shipping. This influences the required navigational dimensions, hence, also the suitable gate types.

Since the barrier is located in a delta area, where big rivers discharge into Tokyo Bay, large sediment quantities are likely to be disposed of near the proposed barrier location. Since the chosen flap gates lie on the seabed in regular conditions, sediment could accumulate on the gates and hinder gate operations, requiring mitigation measures.

The significant wave height, obtained by Carter formulas, greatly influences the required gate heights of the navigational and flow inlet gates, and the crest height of the ungated barrier. However, other approaches to determine the significant wave height could lead to better results or substantiate the obtained values for the significant wave height, peak wave period, and maximum wave height.

Constructability of the proposed design is not considered while establishing the location for the barrier components. The ungated barrier is fragmented by flow inlets and one navigational opening, hence, only the outer sections of the ungated barrier seem to be accessible for trucks and land-based equipment. It should be explored whether water-based equipment is suitable for the site conditions.

Concerning the gate design, it should be noted that the resulting flap gate design is preliminary. The dimensions of the gate and its substructure are based on simplified rules of thumb and ratios derived from a comparable design. The presented concept is therefore intended only to provide a rough indication

and a starting point for a possible gate configuration. It is assumed that the ratios of the Kanadevia gate are applicable to the Tokyo Bay flap gate design. In the gate design, operational systems and the components to provide the necessary buoyancy are left out of the preliminary design.

The loads on the gate are estimated to obtain a first impression of the order of magnitude of the acting forces. Furthermore, the buoyancy and self-weight are assumed to be evenly distributed across the width of the structure, and material properties are taken as constant. The structural components are not assessed for potential failure mechanisms. Including this in the research could lead to different dimensions.

Regarding the design of the ungated barrier, design conditions such as armour layer stability, filter layer stability and toe stability are not taken into account. By analyzing these conditions, outer geometrical dimensions might be different, and internal geometries can be obtained. Moreover, material availability in Tokyo is not considered, which could exclude certain design choices that were made.

Comparing the required freeboard height with the expected storm surge, the influence of wind-generated basin waves appears to be dominant in the calculation of the required crest height of the ungated barrier. However, several assumptions were done related to the discharge overtopping equations. First, the selected discharge overtopping does not correspond with the obtained significant wave height, leading to inconsistency. Second, the significant wave height might not be reliable as discussed above. Thirdly, the angle of wave attack is assumed to be 30 degrees based on the typhoon characteristics. However, due to the rotational wind direction of the typhoon, it can be discussed whether this is a correct assumption. Differing the slope and permeability of the rubble mound would change the friction factor and therefore the freeboard height.

However, the resulting design of the SSB does not fulfill one of the functional requirements, because the tidal flat at the Edo river mout is likely to disappear due to the effects of climate change as the determined SLR of 1.6 $[m]$ by 2200 will surpass the tidal range of the bay and the SSB does not decrease the amount of SLR.

5

Conclusions and recommendations

In this chapter, the most important findings are summarized to draw conclusions regarding the formulated main research question. Furthermore, recommendations for further analysis are provided.

5.1. Conclusion

The aim of this report is to provide preliminary insights for a SSB protecting Tokyo Bay, and specifically Tokyo against flooding associated with typhoons. As a result, the main research question addressed in this report is defined as follows.

> *What could be a preliminary design of a storm surge barrier that protects Tokyo Bay and specifically Tokyo from severe flooding during an extreme storm surge in combination with heavy precipitation resulting from a typhoon?*

To address the main research question, the following sub-questions are answered:

> *a. What are the boundary conditions and functional requirements for designing a possible storm surge barrier protecting Tokyo Bay, and specifically Tokyo?*

The boundary conditions for the SSB in Tokyo Bay are defined by geological, environmental, and economic factors, as well as the stakeholder analysis, which together inform the functional requirements. The design life of the SSB is specified to be 150 years, providing protection against an extreme typhoon event with a return period of 200 years. The barrier should facilitate storage capacity behind the structure to accommodate river inflows while minimizing ecological impacts through adequate flow exchange at the inlets. In addition, the design must provide navigational access for existing and future shipping activities. Adaptability to future climate scenarios and associated uncertainties should be incorporated, along with the addition of value for the Tokyo Metropolitan Area through secondary functions. Furthermore, the remaining natural tidal flat at the Edo River mouth should be preserved, and sufficient redundancy must be included to ensure operational safety in the event of component failure.

> *b. What is a viable location for a storm surge barrier protecting Tokyo Bay, and specifically Tokyo?*

A promising location for a SSB in Tokyo Bay, identified through the MCDA and validated by the cost-property value analysis, is Location 7. This location, which lies closest to Tokyo and connects Haneda Airport with Tokyo Disneyland, achieved the highest overall score, making it the most favorable option for further investigation. Its small wet cross-sectional area, shallow depth, and minimal interference with existing activities enhance its viability and cost-efficiency. While its storage capacity is smaller than other alternatives and it does not protect the entire Tokyo Prefecture, it effectively safeguards the most densely populated and vulnerable low-lying areas. In addition, the location offers the shallowest bathymetry and smallest span, and therefore, it is likely that the costs for the construction of the SSB on this location are comparatively low and less governmental and public resistance is faced. Given these

factors, Location 7 is further evaluated to assess whether it provides sufficient storage capacity and to determine the preliminary dimensions of a barrier designed to withstand a 200-year typhoon event.

c. For what typhoon should the storm surge barrier protect Tokyo Bay, and specifically Tokyo?

Both Method 1 and Method 2 applied in the report result in a design typhoon. A design typhoon consists of many combinations between wind speed and its corresponding pressure and wind direction, and precipitation, which yield a return period of 200 years. The combinations between wind speed and precipitation leading to the maximum water level behind the barrier or the maximum hydraulic load are the critical combinations.

Regarding the evaluation of the storage capacity behind the barrier, Method 2 yields the critical combination of the design typhoon for evaluating the storage capacity at Location 7. Consequently, a typhoon with a wind speed of 53.6 $[m/s]$ and precipitation amounts of 45.9 $[mm/(6hr)]$ and 137.4 $[mm/(10hr)]$, as derived from Method 2, results in a peak discharge of the Arakawa River of 11221 $[m^3/s]$ and a storm surge height of 1.3 $[m]$.

The highest hydraulic load on the barrier occurs when the head difference over the barrier is the largest, while taking into account the typhoon return period, and thus, when the water level in Tokyo Bay is at its maximum and the water level in the basin is at its minimum. This design typhoon has a wind speed of 58.4 $[m/s]$ and negligible precipitation following Method 1, resulting in a storm surge height of 1.4 $[m]$.

d. How sufficient is the storage capacity at the selected barrier location to accommodate river discharge to protect Tokyo Bay, and specifically Tokyo, during a storm surge induced by a typhoon?

As mentioned above, Method 2 identifies the critical design typhoon for evaluating the storage capacity behind the barrier at Location 7. This design typhoon produces the highest water levels behind the barrier, both during and independent of closure, reaching 4.1 $[+m]$ T.P. and 4.3 $[+m]$ T.P., respectively, when the barrier closes at high tide and including a SLR of 1.6 $[m]$ by 2200.

The levees are assumed to have a height of 6.73 $[+m]$ T.P. upon completion of the barrier, as considered in this report. Therefore, it can be concluded that the water level, including the 95% confidence bounds, remains well below the levee crest for the design typhoon under the scenario of barrier closure at high tide. Consequently, the results of the 1D-model indicate that Location 7 provides sufficient storage capacity to prevent the water level from exceeding the surrounding levees during a design typhoon with a return period of 200 years.

e. What would be the dimensions of the storm surge barrier to protect Tokyo Bay, and specifically Tokyo, against the design typhoon?

As mentioned in the answer of subquestion c, for the dimensioning of the barrier, the design typhoon follows from Method 1, resulting in a wind speed of 58.4 $[m/s]$ and a hydraulic head difference of 3.8 $[m]$ over the SSB. An overview of the proposed location and dimensions of the main structural components of the SSB have been established using these parameters. The primary components include the navigational opening, flow inlets and ungated barrier.

From navigational requirements, a navigational width of 350 $[m]$ and a navigational depth of 20.95 $[m]$ are required to enable expected future shipping activities. Based on MCDA results, a flap gate was selected for the navigational gates. In conclusion, in 18 flap gates with a gate width of 32.86 $[m]$ and a gate height of 20.22 $[m]$ are required for the navigational gates. In a first design, the flap gate consists of three main beams ($D = 0.76$ $[m]$), ten sub beams ($D = 0.24$ $[m]$), eight girders ($D = 0.08$ $[m]$ and a skin plate ($t = 0.025$). The main beams and girders stretch over the full length of the gate, the sub beams over the full width. The substructure has a length and depth of respectively 49.29 $[m]$ and 15.17 $[m]$.

The flow inlets have a combined span of 780 $[m]$ and a depth of 15 $[m]$, to facilitate sufficient tidal exchange between the storage basin and Tokyo Bay to maintain ecological habitats as much as possible. The gates for the flow inlets hold the same dimensions as for the navigational opening.

A horizontally composite caisson is chosen for the ungated barrier, which consists of a caisson and a rubble mound armour unit body. A crest height of 26 $[m]$ is required for both structural components. The armour unit body has a slope of 1:1.5, a crest width of 4.5 $[m]$, a characteristic revetment stone diameter of 1.5 $[m]$, a permeable core, a filter layer, and a base width of 43.5 $[m]$. Furthermore, the caisson has a width of 30 $[m]$.

In conclusion to the main research question: based on the selected location, the analysis of the design typhoon, and the one-dimensional hydrodynamic simulations of water levels in the bay and basin, the preliminary results indicate that the proposed storm surge barrier design at Location 7 including the flap gates, caisson embankment design and flow inlets could provide effective protection for Tokyo under design typhoon conditions. The simulations show that the water levels within the basin remain below the levee crests, demonstrating the protective potential of the preliminary barrier design. However, this study represents an initial, system-wide assessment in which all major components have been analyzed at a relatively coarse level to obtain an overall understanding of the system. Consequently, the results should be regarded as preliminary and indicative considerations rather than definitive design recommendations.

5.2. Recommendation

As mentioned in the discussion, the boundary condition analysis and the MCDA were conducted high-over. A more detailed and objective approach in future work could yield a different or more substantiated potential barrier location decision analysis. It is recommended to perform a thorough stakeholder analysis to acquire better insight into the socio-economic perspective of all actors. This way, the proposed design of the storm surge barrier could align better with the interests and demands of different stakeholders, which could increase the support of the storm surge barrier.

In this report, a cost-property value analysis is performed. This provides an overview of the costs of the barrier compared to the property value of the area being protected. However, it is advised to perform a cost-benefit analysis based on the decreased flood risk by implementing the storm surge barrier in Tokyo's water defense. A cost-benefit analysis provides insights about the risk reduction benefits of each possible barrier. This way the results of the MCDA can be supported from an economically viable perspective.

Regarding the typhoon data, the derived design typhoons obtained using either Method 1 or Method 2 were based on rounded wind speed data, which may introduce biased results. In addition, the current approach led to a relatively small number of typhoons making landfall near Tokyo, limiting the Tokyo-specific dataset. This, in turn, could again introduce a bias in the design typhoon estimates. Specifically, the fit of the joint probability distribution would likely improve with the inclusion of more data points. Furthermore, the copula fitting method should be carefully evaluated, as its accuracy and validity have not yet been formally verified.

Besides, in determining the design typhoon, the impact of climate change has not been included yet. Evaluating the impact of climate change on typhoons could result in different values for the typhoon-related parameters.

The 1D-model provided the valuable insight the interaction between river run-off and storm surge is of great importance for Tokyo Bay. The results indicate that the barrier should not only be designed to withstand the surge, but also to provide sufficient storage capacity for river discharge, which increases substantially during a typhoon. If the rivers are unable to discharge effectively, flooding may occur in the hinterland. However, the 1D-model presented in this report is very preliminary, offering a significant scope for further research and refinement. Apart from a more detailed analysis of all boundary conditions, the following key components should be improved. First, the accuracy of the simulation of storm surge height in Tokyo Bay should be improved. In this study, the Horikawa relation was applied for this purpose. However, validation results indicate that this relationship does not provide an optimal fit for the specific hydrodynamic conditions of Tokyo Bay. Furthermore, the modeled storm surge heights are optimistically low in comparison to the proxy storm. Future research should therefore aim to develop or calibrate more accurate relationships capable of simulating storm surge height associated with typhoon-induced extreme events in Tokyo Bay.

Second, for the contribution of the rivers to the water levels during a typhoon at Location 7, a very simplistic hydrological model is used in the 1D-model. The hydrological model assumes that all precipitation in the catchment area, directly results in discharge. Moreover, the storage capacity in the hinterland is assumed to be equal to an estimated negative constant water level and fills up completely during every typhoon before the gates are opened. Furthermore, only the Arakawa River is considered, representing a simplification of the actual hydrological system. Numerous smaller tributaries and diversion channels, originating from the Arakawa, Tama, and Edo Rivers, also discharge into Tokyo Bay, which could affect the water levels through time. Consequently, a more complex hydrological model would more reliably determine the river discharge through time during a typhoon event and, as a result, better model the water level behind the barrier in time.

Third, the water level of the Arakawa River is of interest to understand whether the resulting water levels behind the barrier result in floodings higher up in the system. Consequently, the 1D-model should simulate, in addition to the water level behind and in front of the barrier, the water level in the Arakawa River by incorporating a backwater curve.

Next, the current barrier dimensions and component sizing are based on simplified, rule-of-thumb estimates intended to provide a preliminary concept of the SSB. A comprehensive, detailed design study is advised to refine these initial assumptions and the indicative design. Specifically, site-specific analyses, including geotechnical and liquefaction assessments, are recommended to determine design parameters such as peak ground acceleration to account for seismicity. Additionally, research on failure mechanisms is recommended.

Moreover, to obtain more reliable results for the required crest height of the ungated barrier, as well as the required gate heights of the flow inlets, it is advised to perform an in-depth analysis on the design parameters, especially for the wave-height. Additionally , a sensitivity analysis should be performed, for example, to the Carter formulas using Young and Verhagen's equations (Young & Verhagen, 1996).

Finally, an essential consideration involves the long-term management, maintenance, and funding of the proposed system. For a flap gate design, management requirements are minimal, as the system operates automatically in response to changing water levels. In contrast, other gate types would require a trigger and timing mechanism, supported by research to determine the critical water depth at which closure should occur. To address funding challenges, future studies should further investigate potential secondary functions of the barrier in more detail, such as recreation, energy generation, or ecological enhancement, to attract interest and investment from a wider range of stakeholders.

References

Aerts, J. C. J. H., Botzen, W. J. W., de Moel, H., & Bowman, M. (2013). Cost estimates for flood resilience and protection strategies in new york city. *Annals of the New York Academy of Sciences*, *1294*(1), 1–104. https://doi.org/10.1111/nyas.12200

Aquatic creatures in tokyo bay. (2015). Tokyo Metropolitan Government, Bureau of Environment. https://www.kankyo.metro.tokyo.lg.jp/documents/d/kankyo/creature-aquatic_creature-files-27_suiseireport_color_english

Barrass, C. B. (1979). The phenomena of ship squat. *International Shipbuilding Progress*, *26*(294), 44–47. https://doi.org/10.3233/ISP-1979-2629403

Battjes, J. A., & Labeur, R. J. (2017). *Unsteady flow in open channels*. Cambridge University Press. https://doi.org/10.1017/9781316823136

BBC News. (2019). *Typhoon hagibis: Japan suffers deadly floods and landslides from storm*. Retrieved October 20, 2025, from https://www.bbc.com/news/world-asia-50020108

blent-ai (Maxime Jumelle). (2025). Pycopula: Python copulas library.

Bosboom, J., & Stive, M. J. (2023). *Coastal dynamics*. TU Delft OPEN Books. https://doi.org/10.5074/T.2021.001

Bureau of Port and Harbor, Tokyo Metropolitan Government. (2023). Port of tokyo 2023 [Published March 2023]. Retrieved September 8, 2025, from https://www.kouwan.metro.tokyo.lg.jp/documents/d/kouwan/39337_r5_portoftokyo

Cabinet Secretariat, Government of Japan. (2018). *Fundamental plan for national resilience* [Accessed: 2025-09-08]. Cabinet Secretariat, Government of Japan. https://www.cas.go.jp/jp/seisaku/kokudo_kyoujinka/en/fundamental_plan.pdf

Candella, R. (2016). Rogue waves off the south/southeastern brazilian coast. *Natural Hazards*, *83*. https://doi.org/10.1007/s11069-016-2312-2

Carter, D. J. T. (1982). Prediction of wave height and period for a constant wind velocity using the JONSWAP results. *Ocean Engineering*, *9*(1), 17–33. https://doi.org/10.1016/0029-8018(82)90042-7

Chiyoda City. (2025). *Chiyoda city flood hazard map (english, a4)* [Accessed: 2025-10-04]. https://www.city.chiyoda.lg.jp/documents/2086/hazardmap-en-a4-2.pdf

City, H. (2023). *Prefectural yuhazama dam overview*. Retrieved October 3, 2025, from https://www.city.hanno.lg.jp/kurashi_seikatsukankyo/josuido/sankanchiikikyusui_yuhazamadam/4721.html

ClickView. (2017). *Formation of a tropical cyclone* [YouTube video]. Retrieved October 8, 2025, from https://www.youtube.com/watch?v=UKL9NIxLIIE

Coastal Technology Research Center. (2020, January). *Technical manual for flap-gate type movable breakwaters in ports and coasts* [Chairman: Shoichi Miyazaki].

Daily, J. (2024). *How japan waste incineration ash landfill transforms garbage into new land* [Accessed: 2025-10-03]. https://japandaily.jp/how-japan-waste-incineration-ash-landfill-transforms/

Daniel, R., & Paulus, T. (2019). *Lock gates and other closures in hydraulic projects*. Butterworth Heinemann.

Daniel, R., & Leendertz, J. (1994). Hartel canal barrier - the integrated design approach (in dutch), "bouwdienst magazine", no. 3/1994, september 1994. *Bouwdienst Magazine (Civil Engineering Division Magazine)*.

Du, J., Shen, J., Bilkovic, D. M., Hershner, C. H., & Sisson, M. (2016). A numerical modeling approach to predict the effect of a storm surge barrier on hydrodynamics and long-term transport processes in a partially mixed estuary. *Estuaries and Coasts*, *40*(2). https://doi.org/10.1007/s12237-016-0175-0

Earth, G. (n.d.). Arakawa river [Accessed: 2025-10-03].

Equinox Ocean Turbines. (2025). Equinox ocean turbines [Accessed: 2025-10-23]. https://equinoxoceanturbines.com/

Erbisti, P. C. F. (2014). *Design of hydraulic gates*. CRC Press, Taylor & Francis Group.

Erkens, G., Bucx, T., Dam, R., de Lange, G., & Lambert, J. (2015, November). *Sinking coastal cities* (Technical Report) (Also affiliated with Utrecht University and WaterLand Experts. Correspondence: gilles.erkens@deltares.nl). Deltares Research Institute. Utrecht, the Netherlands. https://piahs.copernicus.org/articles/372/189/2015/piahs-372-189-2015.pdf

Esteban, M., Mikami, T., Shibayama, T., Takagi, H., Jonkman, S. N., & van Ledden, M. (2014). Climate change adaptation in tokyo bay: The case for a storm surge barrier. In P. Lynett (Ed.), *Proceedings of 34th conference on coastal engineering* (pp. 1–12). Coastal Engineering Research Council. https://doi.org/10.9753/icce.v34.management.35

EurOtop. (2018). *Manual on wave overtopping of sea defences and related structures* (2nd). www.overtopping-manual.com.

Fuentes, M. J. R. (2014, June). *Storm surge barrier tokyo bay: Analysis on a system level and conceptual design* [Master's Thesis]. Delft University of Technology. Retrieved October 24, 2025, from https://repository.tudelft.nl/islandora/object/uuid:e9f7b5a8-56fb-47d4-8d7c-67b5b51d1e4b

Gahtan, J., Knapp, K. R., Schreck, C. J., Diamond, H. J., Kossin, J. P., & Kruk, M. C. (2024). International best track archive for climate stewardship (ibtracs) project, version 4r01 [[indicate subset used], Accessed: YYYY-MM-DD]. https://doi.org/10.25921/82ty-9e16

Gedda, A. B., Manu, & Rao, S. (2019). A review on stability of caisson breakwater. In M. Rathinasamy, S. Chandramouli, K. Phanindra, & N. Uma Mahesh (Eds.), *Water resources and environmental engineering i: Surface and groundwater* (pp. 83–88). Springer Nature Singapore Pte Ltd. https://doi.org/10.1007/978-981-13-2044-6_8

Google. (2025). *Google earth (version 9.180.0.1)* [[Computer software]]. https://earth.google.com/

Google Maps. (2025). Google maps [Accessed: October 21, 2025].

Gopinath, R. (2025, February). *Key statistics terms # 28: Part 2 — types of copulas* [Medium, 10 min read]. https://medium.com/@mail2rajivgopinath/key-statistics-terms-28-part-2-types-of-copulas-80ba919c336f

Gornitz, V. (2017). *Storm surge encyclopedia of coastal science, encyclopedia of earth sciences series*. Springer, Cham.

Government, T. M. (2019). *Tokyo bay coastal protection plan (tokyo honpen)*. Tokyo Metropolitan Government, Bureau of Port and Harbor. Retrieved October 3, 2025, from https://www.kouwan.metro.tokyo.lg.jp/documents/d/kouwan/24418_tokyowanengan_kaiganhozen_tokyo_honpen_r4d

Groeneveld, R. (2002). Inland waterways: Ports, waterways and inland navigation [Lecture material].

Guide, J. (n.d.). *Typhoons in japan*. Retrieved October 3, 2025, from https://www.japan-guide.com/e/e2117.html

Hasegawa, H., Sugano, J., Fukuura, T., & Higaki, M. (2023). *Upgrade of jma's storm surge prediction for the wmo storm surge watch scheme (ssws) in 2022* (RSMC Tokyo-Typhoon Center Technical Review 25) (Accessed: 2025-10-03). Japan Meteorological Agency, Numerical Prediction Division. https://www.jma.go.jp/jma/jma-eng/jma-center/rsmc-hp-pub-eg/techrev/text25-1.pdf

Hori, Y. (2024, December). *Rainwater utilization as a key to enhancing urban resilience by sumida city, japan* [Published by ICLEI – Local Governments for Sustainability, "Investing in nature for resilient cities" blog series]. Retrieved October 23, 2025, from https://talkofthecities.iclei.org/rainwater-utilization-as-a-key-to-enhancing-urban-resilience-by-sumida-city/?utm_source=chatgpt.com

Horikawa, K. (1978). *An introduction to ocean engineering*. University of Tokyo Press.

Hoshino, S., Shibayama, T., & Yamada, T. T. (2012). Climate change and coastal defences in tokyo bay. *Coastal Engineering Journal*, *54*(4), 1250008. https://doi.org/10.1142/S0578563412500083

Hoshino, S., Esteban, M., Mikami, T., Takagi, H., & Shibayama, T. (2016a). Estimation of increase in storm surge damage due to climate change and sea level rise in the greater tokyo area. *Natural Hazards*.

Hoshino, S., Esteban, M., Mikami, T., Takagi, H., & Shibayama, T. (2016b). Estimation of increase in storm surge damage due to climate change and sea level rise in the greater tokyo area. *Natural Hazards*, *80*(1), 539–565. https://doi.org/10.1007/s11069-015-1983-4

Hoving, J. (2025, March 21). Ciem4120–oe44210 2025: Basis for design (lecture 02) [Course: Design of Offshore Structures (CIEM4120) and Offshore Design Project (OE44210)].

Hunter, P. (2012). *The St Petersburg flood protection barrier: Design and construction* (HRPP569; Presented at CETMEF PIANC, Paris, 2012). https://eprints.hrwallingford.com/858/1/

HRPP569_The_St_Petersburg_Flood_Protection_Barrier_-_Design_and_Construction.pdf

Inflation Tool. (n.d.). *Value of 2015 japanese yen today - inflation calculator* [Accessed: 2025-10-03]. https://www.inflationtool.com/japanese-yen/2015-to-present-value?amount=1&year2=2025&frequency=yearly

Information, S. P. R. D. P. (n.d.). *Dam information overview (alternative site)*. Retrieved October 3, 2025, from https://suibo-river.pref.saitama.lg.jp/sp/damDetail.html?ccd=12330800005&utm

Inoue, O. (2024, March). *Tokyo resilience project*. Retrieved October 24, 2025, from https://sustainable.japantimes.com/magazine/vol34/34-03

Insurance Journal. (2019). *Typhoon hagibis to cost japan's economy $10b, with insured losses in billions: Aon*. Retrieved October 20, 2025, from https://www.insurancejournal.com/news/international/2019/11/08/548005.htm

Invest Tokyo, Tokyo Metropolitan Government. (2018). Tokyo's urban strength [Accessed: 2025-10-27].

Islam, M. R., Lee, C.-Y., et al. (2021). A new tropical cyclone surge index incorporating the effects of coastal geometry, bathymetry and storm information. *Scientific Reports*, *11*(16747).

Japan Oceanographic Data Center. (n.d.). *500 m gridded bathymetry data*. Retrieved September 4, 2025, from https://www.jodc.go.jp/vpage/depth500_file.html

Japan Science and Technology Agency. (2019, December). December 2019 — "flood control in tokyo metropolis" — s&t articles archive [Updated December 2019; Accessed: 2025-10-27].

JMA. (2025a). *Historical weather data download*. Retrieved October 3, 2025, from https://www.data.jma.go.jp/risk/obsdl/

JMA. (2025b). *Tide observation data tokyo (tokyo)*. Retrieved October 2, 2025, from https://www.data.jma.go.jp/kaiyou/db/tide/genbo/genbo.php

Kaizuka, S. (Ed.). (1993). *Tokyo bay's topography, geology, and water* [Originally published in Japanese]. Tsukiji Shokan Publishing.

Kang, N.-Y., Kim, D., & Elsner, J. B. (2019). The contribution of super typhoons to tropical cyclone activity in response to enso. *Scientific Reports*, *9*, 5046. https://doi.org/10.1038/s41598-019-41561-y

Kasai, A., Fuji, T., Suzuki, K. W., & Yamashita, Y. (2018). Partial migration of juvenile temperate seabass lateolabrax japonicus: A versatile survival strategy. *Fisheries Science*, *84*(2), 153–162. https://doi.org/10.1007/s12562-017-1166-1

Kasai, A., Sakamoto, D., Nakagawa, M., et al. (2019). Amphidromous fish migrations in relation to anthropogenic impacts in estuarine and coastal ecosystems. *Estuarine, Coastal and Shelf Science*, *227*, 106325. https://doi.org/10.1016/j.ecss.2019.106325

Kato-sensei, F. (2025, September). Meeting on storm surge barrier tokyo bay [Recording in possession of the MDP team].

Kawai, H., & Takemura, S. (2003). Simultaneity of maximum storm surge and wave caused by typhoon in tokyo bay, japan [Accessed: 2025-10-03]. In E. Unknown (Ed.), *Coastal engineering 2002* (pp. 1216–1228). World Scientific. https://doi.org/10.1142/9789812791306_0103

Knapp, K. R., Kruk, M. C., Levinson, D. H., Diamond, H. J., & Neumann, C. J. (2010). The international best track archive for climate stewardship (ibtracs): Unifying tropical cyclone best track data. *Bulletin of the American Meteorological Society*, *91*, 363–376. https://doi.org/10.1175/2009BAMS2755.1

Knapp, K. R., & Kruk, M. C. (2010). Quantifying interagency differences in tropical cyclone best-track wind speed estimates. *Monthly Weather Review*, *138*(4), 1459–1473. https://doi.org/10.1175/2009MWR3123.1

Kumano, N., TUCHIDA, K., TAMURA, M., Masunaga, E., KUWAHARA, Y., & YOKOKI, H. (2017). Estimating the cost of coastal protection based on socio-economic scenarios in japan. *Journal of Japan Society of Civil Engineers, Ser. B3 (Ocean Engineering)*, *73*, 1007–1012. https://doi.org/10.2208/jscejoe.73.I_1007

Kuramoto, H. (2006). Seismic design codes for buildings in japan. *Journal of Disaster Research*, *1*(3), 341–346. https://doi.org/10.20965/jdr.2006.p0341

Ligteringen, H. (2009). Lecture notes cie4330 and cie5306: Ports and terminals [Lecture notes].

Lloyds Bank Trade – International Trade Portal. (2025). Arrange transport of goods to and from japan [Accessed: 2025-10-27].

Lyu, H. M., Wang, G. F., Shen, J. S., Lu, L. H., & Wang, G. Q. (2019). Inundation analysis of metro systems with swmm — a case study of guangzhou, china [Preprint version (version 5) accessed 2025-10-29]. *Hydrology and Earth System Sciences Discussions*, *hess-2019-28*. https://hess.copernicus.org/preprints/hess-2019-28/hess-2019-28-manuscript-version5.pdf

Manning, D. (2024, March). *Tokyo prioritizes tackling floods before the next big one* [Accessed: 2025-09-08]. https://japan-forward.com/tokyo-prioritizes-tackling-floods-before-the-next-big-one/

McVeigh, K. (2023, June). Before the flood: How much longer will the thames barrier protect london? [Accessed: 2025-10-28].

Md. Rezuanul Islam, H. T. (2020). Typhoon parameter sensitivity of storm surge in the semienclosed tokyo bay. *Frontiers of Earth Science*, *14*(3), 553–567.

MILT, K. R. D. B. (n.d.). *Arakawa second and third flood control reservoirs*. Retrieved October 3, 2025, from https://www.ktr.mlit.go.jp/arajo/arajo00761.html

MILT, K. R. D. B. (2017). *Arakawa upper reaches river maintenance and management plan*. Retrieved October 3, 2025, from https://www.ktr.mlit.go.jp/ktr_content/content/000687781.pdf

MILT, K. R. O., Kanto Regional Development Bureau. (n.d.). *Floodwater level names*. Retrieved October 3, 2025, from https://www.ktr.mlit.go.jp/keihin/keihin00263.html

Ministry of Land, Infrastructure, Transport and Tourism. (2020). Haneda airport for tomorrow: On new flight routes from 29 march 2020 (vol. 2). https://www.mlit.go.jp/koku/haneda/public/pdf/haneda_Pamphlet_english_vol2.pdf

Ministry of Land, Infrastructure, Transport and Tourism (MLIT), Water Management and National Land Conservation Bureau. (2024, October). : (tech. rep.) ( ). Ministry of Land, Infrastructure, Transport and Tourism, Japan. Retrieved October 21, 2025, from https://www.mlit.go.jp/river/

Ministry of the Environment, Government of Japan. (2025). *Ecologically or biologically significant marine areas (ebsas)*. Retrieved September 8, 2025, from https://www.env.go.jp/en/nature/biodic/kaiyo-hozen/kaiiki/index.html

Miyazaki, M. (2003). *Storm surge research- examples and mechanisms*. Seizando-Shoten Publishing.

MLIT, K. R. D. B. (n.d.-a). *Futase dam overview / facility information*. Retrieved October 3, 2025, from https://www.ktr.mlit.go.jp/futase/futase00008.html?utm

MLIT, K. R. D. B. (n.d.-b). *Futase dam report (pdf)*. Retrieved October 3, 2025, from https://www.ktr.mlit.go.jp/ktr_content/content/000700546.pdf

Mooyaart, L., & Jonkman, S. (2017). Overview and design considerations of storm surge barriers. *Journal of Waterway Port Coastal and Ocean Engineering*, *143*(4). https://doi.org/10.1061/(asce)ww.1943-5460.0000383

Mooyaart, L., Jonkman, S., de Vries, P., & Ad Toorn, a. M. L. (2014). Storm surge barrier: Overview and design considerations. *Coastal Engineering Proceedings*, *1*, 45. https://doi.org/10.9753/icce.v34.structures.45

Nakamura, R., Shibayama, T., Esteban, M., Iwamoto, T., & Nishizaki, S. (2020). Simulations of future typhoons and storm surges around tokyo bay using ipcc ar5 rcp 8.5 scenario in multi global climate models. *Coastal Engineering Journal*, *62*(2), 1709014. https://doi.org/10.1080/21664250.2019.1709014

Nakayasu, K. (2024, December 2). *Introduction of flap-gate type flood control technology* [Presentation at Forum with PUB-CFI 2. General Manager, Hydraulic Gate Design Department, Steel Structure & Disaster Prevention Business Unit, Kanadevia Co., Ltd.].

NASA. (2025). *Projected sea level rise*. Retrieved October 2, 2025, from https://sealevel.nasa.gov/ipcc-ar6-sea-level-projection-tool

Needham, H. F., & Keim, B. D. (2013). Correlating storm surge heights with tropical cyclone winds at and before landfall. *Earth Interactions*, *18*(7), 1–26.

Nishi, K., Kawai, M., Cahyono, B. E., Waqar, M. M., Nishi, K., & Sumantyo, J. T. S. (2023). Consecutive dinsar and well based on the law of material conservation between land surface pressure and ground water to observe land subsidence. *Geocarto International*, *38*(1), 2159069. https://doi.org/10.1080/10106049.2022.2159069

NOAA. (2005). *Hurricane basics*. Retrieved October 6, 2025, from https://repository.library.noaa.gov/view/noaa/12828

Ocean Outcomes. (2025). Tokyo bay sea perch fishery improvement project [Accessed: 2025-09-08]. https://www.oceanoutcomes.org/where-we-work/japanese-fisheries-seafood/tokyo-bay-sea-perch/

Oceanic, N., & Administration, A. (2023). *Learning lesson: Quadrophonic wind*. Retrieved October 3, 2025, from https://www.noaa.gov/jetstream/tc-tcm/learning-lesson-quadraphonic-wind#:~:text=The%20strongest%20winds%20are%20nearly,wind%20field%20in%20each%20quadrant.

of Engineers, U. A. C. (1992, August). *Table c-l friction coefficient for concrete cast on soil* (tech. rep. No. ETL 1110-3-446) (Approved for public release; distribution is unlimited). U.S. Army Corps of Engineers, CEMP-ET, Washington, DC.

of Port, B., & Harbor, T. M. G. (2020, January). Inspection cruise ship "tokyo-minato-maru".

of Waterworks, B. (n.d.). *Water source facilities*. Retrieved October 3, 2025, from https://www.waterworks.metro.tokyo.lg.jp/suigen/antei/04?utm

Ohta, H. (2024). Storm surge barrier across tokyo bay (tokyo bay passageway). *World Conference for TOKYO Resilience, Aiming for "Safety for the NExt 100 Years"*, 221–226. Retrieved October 23, 2025, from https://www.tokyo-world-conference.com/index.html

OneOcean Group. (n.d.-a). https://www.findaport.com/port-of-tokyo

OneOcean Group. (n.d.-b). https://www.findaport.com/port-of-yokohama

OneOcean Group. (n.d.-c). https://www.findaport.com/port-of-chiba

PAGASA. (n.d.). *About tropical cyclone*. Retrieved October 3, 2025, from https://www.pagasa.dost.gov.ph/information/about-tropical-cyclone

Parker, C. (2016). *Overview of tokyo's rivers* [Accessed: 2025-10-09]. https://thetokyofilesrivers.wordpress.com/about/

Pascal, B. (1663). *Traité de l'équilibre des liqueurs, et de la pesanteur de la masse de l'air* [Posthumous publication]. Guillaume Desprez. Retrieved October 9, 2025, from https://gallica.bnf.fr/ark:/12148/bpt6k577191.image

Peters, D. J. (2025). Ciem4110 – steel gates: Tutorial, 13 march 2025 [Course: Hydraulic Structures (CIEM4110), Track: Hydraulic and Offshore Structures (HOS)].

PIANC – The World Association for Waterborne Transport Infrastructure. (2014). *Harbour approach channels design guidelines* (Report No. 121) (Permanent International Association of Navigation Congresses). PIANC, MarCom Working Group 121. Brussels, Belgium.

Population, T. B. C. (2022, December). *Japan: Administrative division - population statistics, charts and map* [Accessed: 2025-10-03]. https://www.citypopulation.de/en/japan/admin/

Prefecture, S. (2023). *Dam specifications — gokaku dam*. Retrieved October 3, 2025, from https://www.pref.saitama.lg.jp/b1007/k-dam/k-dam-shogen.html

Profile of yatsu higata [Accessed: 2025-09-08]. (2025). Narashino City Nature Observation Center. https://www.seibu-la.co.jp/yatsuhigata/english.html

Ralston, D. K. (2022). Impacts of storm surge barriers on drag, mixing, and exchange flow in a partially mixed estuary. *Journal of Geophysical Research: Oceans*, *127*(4). https://doi.org/10.1029/2021JC018246

Rijkswaterstaat. (2015, December). *De kunst van het samenwerken* [Zakelijk & Innovatie 04, maandag 21 december 2015]. Retrieved October 23, 2025, from https://www.magazinesrijkswaterstaat.nl/zakelijkeninnovatie/2015/04/de-kunst-van-het-samenwerken

Rijkswaterstaat. (2023). *Maeslant barrier* [Accessed: 2025-10-03]. Retrieved October 3, 2025, from https://www.rijkswaterstaat.nl/en/projects/iconic-structures/maeslant-barrier

Rijkswaterstaat. (2024, May). 6 nieuwe megapompen in de afsluitdijk: Voorbereid op extreem hoogwater [Gepubliceerd op 8 mei 2024, laatste update 10 mei 2024, Rijkswaterstaat]. https://www.rijkswaterstaat.nl/nieuws/archief/2024/05/6-nieuwe-megapompen-in-de-afsluitdijk-voorbereid-op-extreem-hoogwater

Rijkswaterstaat. (2025a). *Afsluitdijk*. Retrieved October 23, 2025, from https://www.rijkswaterstaat.nl/water/waterbeheer/bescherming-tegen-het-water/waterkeringen/dijken/afsluitdijk

Rijkswaterstaat. (2025b). *Oosterscheldekering*. Retrieved October 23, 2025, from https://www.rijkswaterstaat.nl/water/waterbeheer/bescherming-tegen-het-water/waterkeringen/deltawerken/oosterscheldekering

Rijkswaterstaat. (2025c, January). Afsluitdijk. https://www.rijkswaterstaat.nl/water/waterbeheer/bescherming-tegen-het-water/waterkeringen/dijken/afsluitdijk

Sekine, M., Wu, Y., Baba, W., & Ogata, K. (2020). Prediction of urban inundation and flooding of urban rivers caused by heavy rainfall and storm surge in tokyo 23 wards [Using the S-uiPS urban inundation prediction system]. *Proceedings of the 22nd Congress of the International Association for Hydro-Environment Engineering and Research – Asia Pacific Division (IAHR-*

APD 2020). https://waseda.elsevierpure.com/en/publications/prediction-of-urban-inundation-and-flooding-of-urban-rivers-cause/

Shimozono, T., Tajima, Y., Kumagai, K., Arikawa, T., Oda, Y., Shigihara, Y., Mori, N., & Suzuki, T. (2020). Coastal impacts of super typhoon hagibis on greater tokyo and shizuoka areas, japan. *Coastal Engineering Journal*, *62*(2), 129–145. https://doi.org/10.1080/21664250.2020.1744212

Smaal, A., & Nienhuis, P. (1992). The eastern scheldt (the netherlands), from an estuary to a tidal bay: A review of responses at the ecosystem level. *Netherlands Journal of Sea Research*, *30*, 161–173. https://doi.org/10.1016/0077-7579(92)90055-j

Spreadsheets, C. (2025). Typical soil bearing capacity [Accessed: 2025-10-25].

Stalenberg, B., & Vrijling, H. (2009). The battle of tokyo and dhaka against floods ["Tokyo and Dhaka: their battle against floods" (related conference paper, 2007)]. *Built Environment*.

Statistics Bureau of Japan. (2020). Final report on fisheries output value: 2020 fisheries output statistics table 2 – statistical table by major sea areas and prefectures (marine fisheries and aquaculture output values) [Accessed: 2025-09-08]. https://www.e-stat.go.jp/dbview?sid=0002001226

Stein, R. S., Toda, S., Parsons, T., & Grunewald, E. (2006). Probabilistic seismic hazard assessment for greater tokyo: Severe shaking and peak ground acceleration [Accessed: 2025-09-22]. *Philosophical Transactions of the Royal Society A*, *364*(1845). https://doi.org/10.1098/rsta.2006.1808

Suprayogi, H., Rudyanto, A., Bachtiar, H., & Limantara, L. M. (2018). Critical-phase sea dike construction of ncicd program in jakarta as national capital city. *IOP Conference Series: Earth and Environmental Science*, *162*, 012020. https://doi.org/10.1088/1755-1315/162/1/012020

Takagi, H., Cao, A., & Esteban, M. (2023). Cumulative land subsidence in populated asian coastal cities. *Journal of Coastal and Riverine Flood Risk*, *1*. https://doi.org/10.48438/jcrfr.2023.0002

Tanimoto, S., Katsutoshi; Takahashi. (1994). Design and construction of caisson breakwaters - the japanese experience. *Coastal Engineering*.

Tara, R. (2023). Venice's tide barrier has already cost €6 billion — will it work? [Accessed: YYYY-MM-DD]. *Engineering.com*. https://www.engineering.com/venices-tide-barrier-has-already-cost-6-billion-euros-will-it-work/

Tatekoji, A., Nakamura, R., & Shibayama, T. (2016). Influence of historical bathymetric changes due to urbanization on the vulnerability of storm surge in tokyo bay. *Proceedings of the 35th International Conference on Coastal Engineering (ICCE)*. https://doi.org/10.9753/icce.v35.management.22

ThinkHazard! (2025). Earthquake hazard in tokyo, japan [Accessed: 2025-09-22].

Tian, K. (2014, October). *Tokyo bay storm surge barrier: A conceptual design of the moveable barrier* [Master's Thesis]. Delft University of Technology. Retrieved October 24, 2025, from https://repository.tudelft.nl/islandora/object/uuid:7c3c9112-b16a-4b49-b4cb-3d92cb26bff2

Tokyo Bay Waterway Office. (2015). *Tokyo bay in numbers* [Retrieved September 9, 2025]. https://www.pa.ktr.mlit.go.jp/wankou/data/index.htm

Tokyo Metropolitan Government. (2023, April). The front line of the ocean, protecting tokyo against flood damage [Accessed: 2025-10-27].

Tokyo Metropolitan Government. (2025a). Tokyo resilience project [Accessed: 9 October 2025].

Tokyo Metropolitan Government. (2025b, January 22). *Revision of maps of areas expected to be inundated by storm surges* [Category: Wind and flood damage; published on Tokyo Resilience Project website]. Retrieved September 9, 2025, from https://tokyo-resilience.metro.tokyo.lg.jp/en/news/1920/

Tokyo Metropolitan Government, B. o. P., & Harbor. (2023). The front line of the ocean, protecting tokyo against flood damage [Accessed: 2025-10-17].

Tokyo Port Terminal Co., L. (2024). *Fy2024–2028 management strategy (6th mid-term management plan)* [Accessed: 2025-10-03]. https://www.tptc.co.jp/cms/2025/FY2024-2028_Management_Strategy.pdf

Tokyo Port Terminal Corporation. (2024). Management strategy. Retrieved September 8, 2025, from https://www.tptc.co.jp/cms/2025/FY2024-2028_Management_Strategy.pdf

Tsuchiya, N. (2024). Tokyo bay high surge levee concept: How can we protect tokyo from the largest imaginable storm surge. *World Conference for TOKYO Resilience, Aiming for "Safety for the NExt 100 Years"*, 265–275. Retrieved October 23, 2025, from https://www.tokyo-world-conference.com/index.html

Typhoon, D. (n.d.-a). *Digital typhoon*. Retrieved October 15, 2025, from https://agora.ex.nii.ac.jp/digital-typhoon/

Typhoon, D. (n.d.-b). *The intensity and size of typhoons - units of pressure and wind*. Retrieved October 3, 2025, from https://agora.ex.nii.ac.jp/digital-typhoon/help/unit.html.en

Ueda, T., Ogawa, M., Sugimura, Y., Kawasaki, T., & Matsuda, T. (2025). Predicting the maximum size of container vessels in the future. *Research in Transportation Business I& Management*, *61*, 101382. https://doi.org/10.1016/j.rtbm.2025.101382

Um, M. J., Joo, K., Nam, W., & Heo, J. H. (2017). A comparative study to determine the optimal copula model for the wind speed and precipitation of typhoons [© 2016 Royal Meteorological Society]. *International Journal of Climatology*, *37*(4), 2051–2062. https://doi.org/10.1002/joc.4834

Umgiesser, G. (2020). The impact of operating the mobile barriers in venice (mose) under climate change. *Journal for Nature Conservation*, *54*, 125783. https://doi.org/10.1016/j.jnc.2019.125783

Voiland, A. (2019). *Typhoon hagibis brings heavy rains to japan*. Retrieved October 20, 2025, from https://gpm.nasa.gov/applications/weather/typhoon-hagibis-brings-heavy-rains-japan

Voorendt, M. Z. (2022, February). *Manual hydraulic structures* (2022nd ed.) [Lecture notes for the course Hydraulic Structures 1 (CTB3355 / CIE3330)]. Delft University of Technology. https://repository.tudelft.nl/

Wavenergy.it S.r.l. (2014, November). The first worldwide application at full-scale of the rewec3 device in the port of civitavecchia [Accessed: 2025-10-23]. https://www.wavenergy.it/generico/the-first-worldwide-application-at-full-scale-of-the-rewec3-device-in-the-port-of-civitavecchia/

Wikipedia. (2025). *Mose* [Accessed: 2025-10-03]. Retrieved October 3, 2025, from https://en.wikipedia.org/wiki/MOSE

World Meteorological Organization. (2023). *Characteristics of tropical cyclones*. Retrieved October 6, 2025, from https://wmo.int/content/characteristics-of-tropical-cyclones

Wüthrich, D. (2025). Design of hydraulic structures: Weirs & barriers - examples & definitions [Lecture presented at TU Delft for Design of Hydraulic Structures course (CIEM4110) for the Hydraulic and Offshore Structures track, February 17, 2025].

Xu, C., Liu, H., Yao, Y., Zhong, X., & Shi, Q. (2025). Wave attenuation and wave forcing of a modular artificial reef located on a coral reef topography considering coral canopy growth. *Ocean Engineering*, *341*. https://doi.org/10.1016/S0029-8018(25)02268-1

Yamamoto, T. (2019, May). Cooperation among ports within tokyo bay [Online: https://www.iaphworldports.org/n-iaph/wp-content/uploads/2020/12/3.-Taishi-Yamamoto-Cooperation-among-ports-within-Tokyo-Bay.pdf].

Yasuda, S., Harada, K., Ishikawa, K., & Kanemaru, Y. (2012). Characteristics of liquefaction in tokyo bay area by the 2011 great east japan earthquake [Special Issue on Geotechnical Aspects of the 2011 off the Pacific Coast of Tohoku Earthquake]. *Soils and Foundations*, *52*(5), 793–810. https://doi.org/https://doi.org/10.1016/j.sandf.2012.11.004

Young, I., & Verhagen, L. (1996). The growth of fetch limited waves in water of finite depth. part 1. total energy and peak frequency. *Coastal Engineering*.

Zhai, G., Xu, W., Su, P., Qin, L., & Liao, X. (2024). Characteristics of precipitation changes during tropical cyclone processes in china from 1980 to 2019. *Scientific Reports*, *14*, 13654. https://doi.org/10.1038/s41598-024-64252-9

Zhao, Y., Liu, Q., Huang, R., Pan, H., & Xu, M. (2020). Recent evolution of coastal tidal flats and the impacts of intensified human activities in the modern radial sand ridges, east china [Accessed: 2025-10-04]. *International Journal of Environmental Research and Public Health*, *17*(10), 3191. https://doi.org/10.3390/ijerph17103191

Zhong, H., Overloop, P.-J. V., Gelder, P. V., & Rijcken, T. (2012). Influence of a storm surge barrier's operation on the flood frequency in the rhine delta area. *Water*, *4*(2), 474–493. https://doi.org/10.3390/w4020474

A

MDP flow chart

This appendix presents the MDP flow chart. The project team was divided into two sub-teams. Team He + RS consisted of two master's students in Civil Engineering, specializing in Hydraulic Engineering with a focus on Coastal Engineering, and one master's student in Applied Earth Sciences specializing in Remote Sensing. Team HOS comprised three master's students in Hydraulic and Offshore Structures, one specializing in Dams, Dikes, and Breakwaters, one in Marine Renewables, and one in Floating and Submerged Structures.

Figure A illustrates the flow chart used by the team throughout the project. The process was divided into two parallel flows that were interconnected, as the results from one were required as input for the other. The vertical connecting lines indicate these dependencies between the two flows. This flow chart shows the multidisciplinary process of the project.

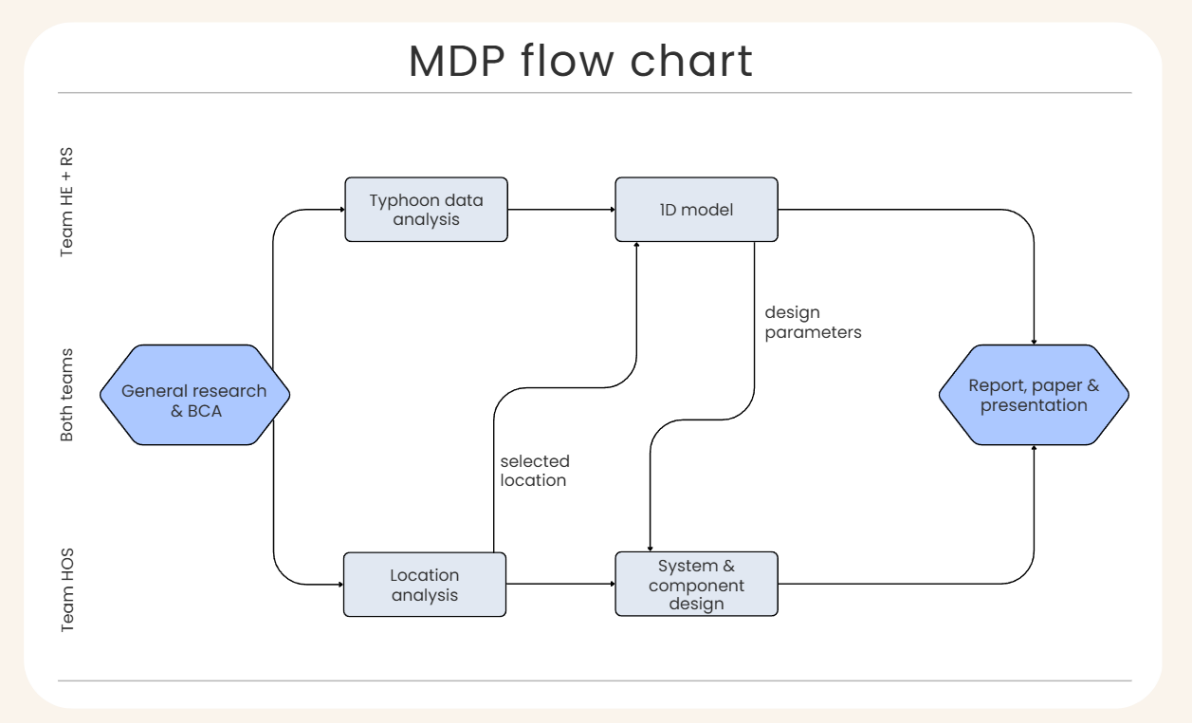

Figure A.1: MDP flow chart.

B

Interview Japan Riverfront Research Center

The meeting with representatives of the Japan Riverfront Research Center focused on storm-surge protection in Tokyo Bay, technical and economic considerations for large barriers, and lessons from international examples such as the Netherlands' Maeslantkering and Venice's MOSE.

B.1. Background and Risk

Tokyo Bay has a long history of storm-surge damage, including the 1917 typhoon, which caused approximately 1,500 fatalities. Modern risks include:

- Sea-level rise, stronger typhoons, and heavier rainfall.
- Concentration of residential, industrial, and port assets along low-lying shores.

B.2. Current Defenses

- Levees stand 8–10 m above sea level, designed for storm surges of 5.1 m AP; future targets are 6.1 m.
- Tokyo Metropolitan Government plans to raise harbor seawalls by 1.4 m (completion by 2040).
- Only the Edo River has a tidal barrier to prevent salinity intrusion into drinking-water intakes.

B.3. Barrier Concepts and Engineering Challenges

Large-scale storm-surge barriers are under consideration, including a 27 km closure near Haneda Airport. Alternatives include segmented or flap-gate systems. Key challenges include:

- **Navigation:** Must allow passage for deep-draft container ships (20 m) and cruise liners (15 m).
- **Hydrology:** Avoid backwater flooding from major rivers (Tama, Sumida, Arakawa, Edo) during heavy rainfall.
- **Ecology and Water Quality:** Limit closure time to prevent stagnation and habitat loss.

B.4. Economic and Governance Considerations

- Ports in Tokyo, Kawasaki, Yokohama, and Chiba handle nearly half of Japan's container throughput.
- Cost–benefit analyses should include avoided losses from port shutdowns and supply-chain disruptions.
- Funding may require public-private partnerships, similar to Venice's MOSE.

- Advocates encourage broader civic and corporate participation in infrastructure investment.

B.5. Climate Scenarios and Design Loads

Future barriers must accommodate:

- Sea-level rise projections through 2100.
- Intensifying typhoons (central pressure 900 hPa; benchmark surge 8 m).
- Increasing annual rainfall (Tokyo 1,700 mm, >2,000 mm in western Japan), which affects river discharge during closures.

B.6. Broader Opportunities and Integration

- Potential integration with new transport corridors (e.g., Haneda–Narita link) or floating urban developments.
- Learning from Dutch and Italian examples: Maeslantkering's sector gates and MOSE's flap gates.
- Modular or staged construction could ease navigation constraints and cost.

B.7. 7. Implementation Path

Tokyo Metropolitan Government has begun independent works such as seawall elevation. A feasibility study is planned to refine:

- Barrier location and gate type.
- Hydraulic performance under extreme events.
- Cooperation with domestic and international experts for design optimization.

B.8. Conclusion

Rising seas, stronger typhoons, and expanding economic assets highlight the need for stronger coastal defenses in Tokyo Bay. A storm-surge barrier, integrated with river management and environmental safeguards, could provide long-term resilience. Success will depend on sound engineering, robust economics, environmental stewardship, and shared public-private responsibility.

C

Interview Ministery of Land, Infrastructure, Transport and Tourism

The meeting with the representative of the Ministery of Land, Infrastructure, Transport and Tourism (MLIT) focused on storm surge protection in Tokyo Bay and whether a large storm surge barrier would be feasible or desirable. Comparisons were drawn between Japan's approach and the Netherlands' approach to long-term coastal defense.

C.1. Current Protection and Risk

Tokyo is considered less vulnerable to climate change at present due to its existing infrastructure compared to the rest of Japan (though it remains at risk). Japan generally does not plan protection measures beyond 2100 because of uncertainties in climate projections. The government focuses on scenarios of up to approximately one meter of sea-level rise this century, unlike the Netherlands, which plans for much longer time horizons (even up to 2200).

C.2. Barrier Options and Challenges

While some argue that a single large barrier might be cost-effective, there are significant drawbacks:

- Environmental impacts on tidal flats, fisheries, seaweed beds, and broader ecological systems.
- Cultural importance of the remaining tidal flats (e.g., Sanbanze area) and their link to Tokyo's fishing traditions and sushi heritage.
- Strong opposition from fishermen and the public due to concerns about livelihoods and cultural identity.
- Industrial and port access must be preserved — Chiba, Yokohama, and Kawasaki are major hubs for cars and imports/exports.
- Stakeholders worry that a barrier would disrupt maritime traffic and fisheries.

C.3. Public Opinion and Politics

- Local fishermen and environmental groups largely oppose the idea of barriers.
- Much of the public supports protection of the bay's ecological and cultural character.
- Industry remains neutral but expresses concern over costs and port access.
- Governmental vision emphasizes an "ecologically friendly Tokyo Bay," a goal shared by Tokyo, Chiba, and Kanagawa prefectures.

C.4. Design Standards and Operation

Japan currently does not apply probabilistic design standards (e.g., 1/10,000-year flood criteria as in the Netherlands). If storm surge barriers were to be built, they would likely operate based on typhoon forecasts and tidal predictions from the Japan Meteorological Agency (24–48 hours in advance). Secondary functions — such as recreation, parks, fishing piers, or public landmarks — could be integrated but remain secondary to flood protection.

C.5. Netherlands vs. Japan Approach

- **Netherlands:** very high safety standards, long-term (multi-century) planning, strong historical motivation, and willingness to invest heavily for security.
- **Japan:** shorter planning horizon, cautious investment due to demographic and fiscal uncertainty, and a focus on balanced, cost-effective protection.

Japanese participants expressed interest in learning from Dutch experience and expertise.

C.6. Closing Notes

Both sides recognized the value of continued collaboration between Japan and the Netherlands. Any decision regarding a Tokyo Bay barrier must balance cost-effectiveness, resilience, environmental preservation, cultural values, and industrial accessibility.

D

Reasoning of criteria for MCDA of location of SSB

In the MCDA to identify the most promising location for the SSB, the performance of each location per criterion is found by establishing a formula per criterion. The derivation of the formulas is explained for each criterion below.

D.1. Costs

From a financial perspective, minimizing costs is preferable. Costs also serve as an indicator of overall project feasibility. In this MCDA, costs are expressed in terms of the wet cross-sectional area of each SSB.

Wet cross-sectional area
The wet cross-sectional area is estimated by integrating the bathymetry along each proposed barrier alignment. The larger the wet cross sectional area, the higher the construction costs, hence the lower the score.

As such, the performance per location can found using Equation D.1 where the larger the share of wet cross sectional area, the lower the score for $location\ [i]$. In the formula n represents the number of locations evaluated, and i the evaluated location.

$$\%\ Wet\ Area\ [i] = \frac{Wet\ Area\ location\ [i]}{Sum(Wet\ Area : location\ [0, ..., n]} \tag{D.1}$$

D.2. Protectiveness

Protectiveness represents the degree to which people, assets, and ecological values are safeguarded. Accordingly, three sub-criteria are considered: protected residential area, protected port area, and preserved ecological habitats.

D.2.1. Residential area

The protected residential area is determined using the elevation map by Tokyo Metropolitan Government (Tokyo Metropolitan Government, 2025b) in combination with the proposed locations. For each location, the extent of the protected area was estimated using Google Earth. Assuming this area primarily represents residential land, the proportion of protected area per location was calculated relative to the total area below sea level. It is assumed that all the areas have an equal population density.

The resulting effectiveness in protecting residential neighborhoods can be evaluated per location by Equation D.2.

$$\%\ Protected\ residential\ area\ [i] = \frac{Protected\ residential\ area : location\ [i]}{Max(protected\ residential\ area : location\ [0, ..., n])} \tag{D.2}$$

Since the effectiveness of each SSB was already considered during the selection of possible barrier locations, the location with the smallest protected area is assigned a moderate baseline score (0). Larger protected residential areas are considered more favorable and therefore receive higher scores.

D.2.2. Port area

The extent of protected port surface area $\left[m^2\right]$ is estimated based on Google Maps. The larger the protected port surface area, the higher the score. The resulting effectiveness in protecting port area can be evaluated per location by Equation D.3. It is assumed that all the port areas are all of equal importance.

$$\%\ Protected\ port\ area\ [i] = \frac{Protected\ port\ area : location\ [i]}{Max(protected\ port\ area : location\ [0, .., n])} \tag{D.3}$$

D.2.3. Ecological habitats

A barrier influences the bay's ecological balance and affects tidal flats by limiting tidal exchange. Consequently, barriers with larger storage basins restrict tidal exchange over a greater portion of the bay and therefore receive lower scores. Besides, construction near ecological hubs is negatively accounted for in the decision analysis. The resulting effectiveness in protecting ecological habitats can be evaluated per location by comparing the storage area per location as formulated in Equation D.4.

$$\%\ Affected\ ecological\ area\ [i] = \frac{Surface\ area\ basin : location\ [i]}{Max(Surface\ area : location[0, ..., n])} \tag{D.4}$$

D.3. Accessibility

Accessibility measures the extent to which the barrier disrupts bay activities. Here primarily fisheries are taken into account to determine accessibility as port activity will not be hindered as that is a design requirement defined in Section 2.1. Consequently, the continuity of fishing grounds is used as the main criterion.

A single, continuous fishing ground supports both efficient fishing operations and ecological connectivity. Therefore, a low fragmentation ratio, defined as the storage basin area of the barrier relative to the total bay surface, is assumed favorable. A larger storage area indicates greater fragmentation of the fishing grounds, leading to increased obstruction for fishermen and consequently a lower score. The resulting accessibility for fishing activities can be evaluated using Equation D.5.

$$\%\ Undisturbed\ fishing\ area\ [i] = \frac{Storage\ area : location\ [i]}{Total\ surface\ area : Tokyo\ Bay} \tag{D.5}$$

D.4. Technical Feasibility

Technical feasibility evaluates the structural practicality of each site. Since construction at great depths is particularly challenging - resulting in higher risks and costs - the maximum depth along each location is used as the main indicator. A greater maximum depth implies greater risk and, consequently, a lower feasibility score. The largest depth is assumed poor and the smallest depth excellent. The other locations are scored respectively. As such, the locations are scored by comparing their absolute maximum depth values.

E

Loads on gate

This appendix shows how the wind load, hydrostatic load and wave load work on the gate, separately.

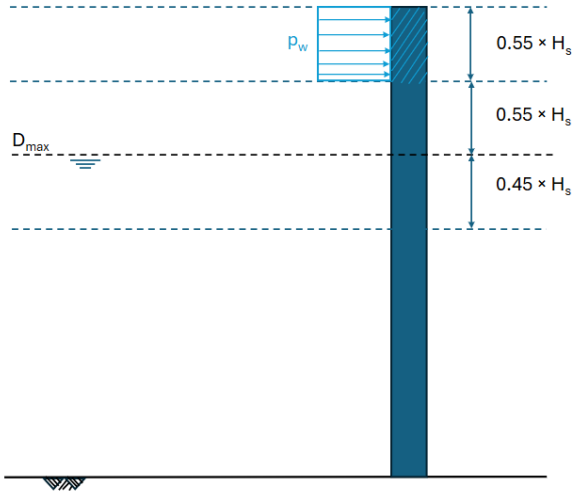

Figure E.1: Wind load on gate.

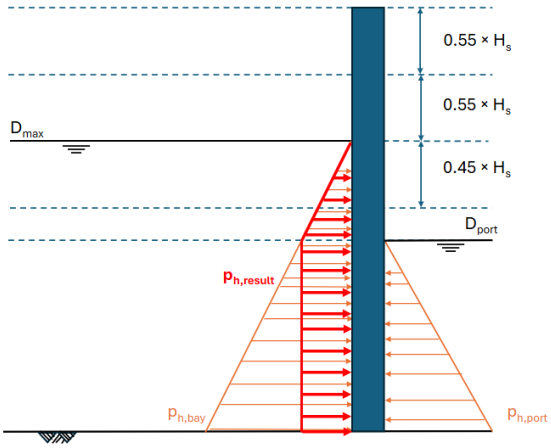

Figure E.2: Hydrostatic load on gate.

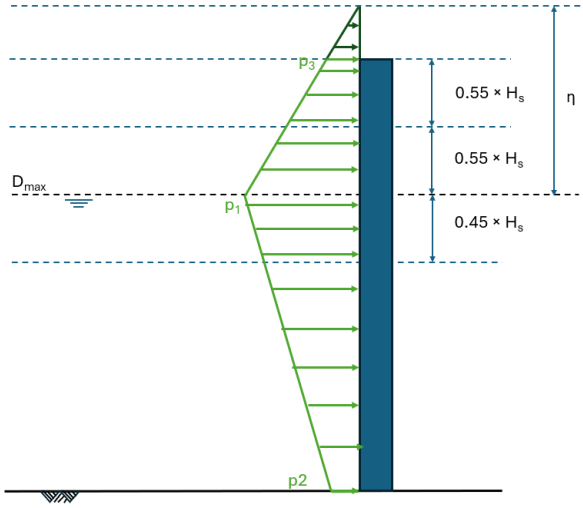

Figure E.3: Wave loads on the gate.

F

Bathymetry per possible location

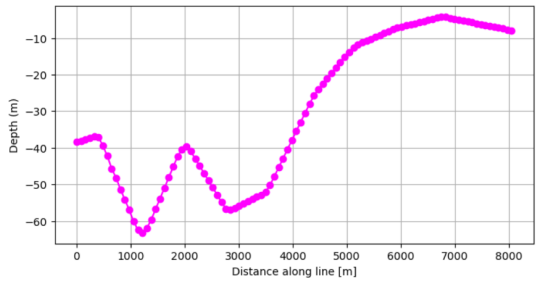

(a) Location 1

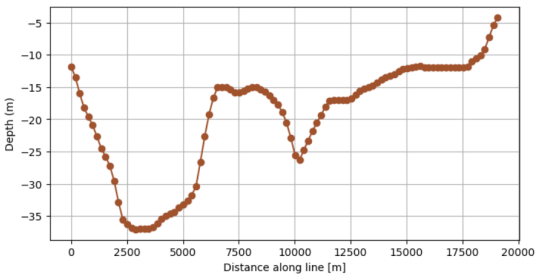

(b) Location 2

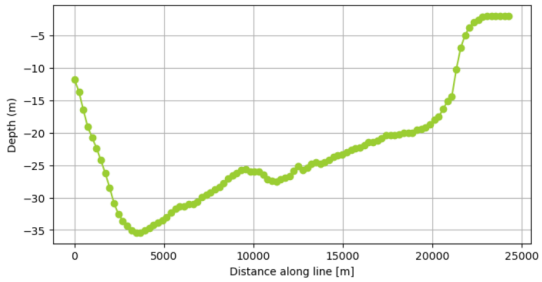

(c) Location 3

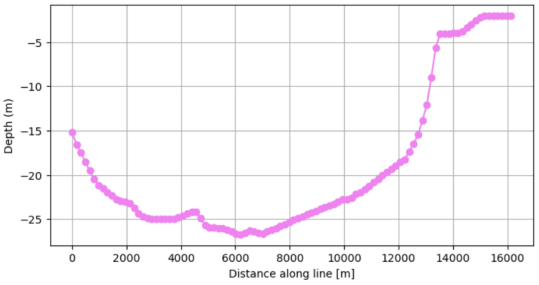

(d) Location 4

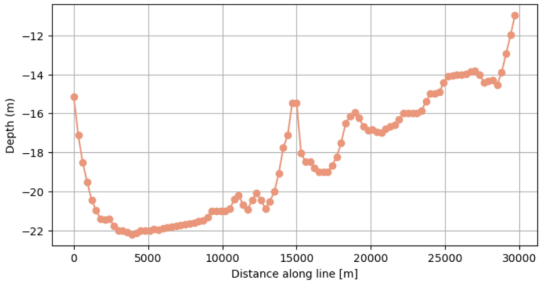

(e) Location 5a

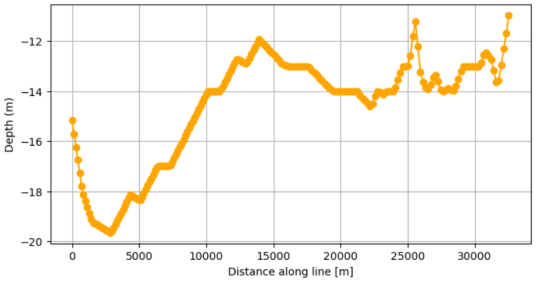

(f) Location 5b

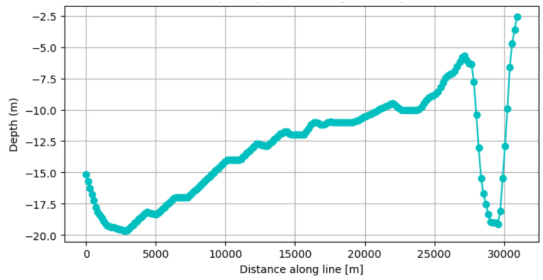

(g) Location 6

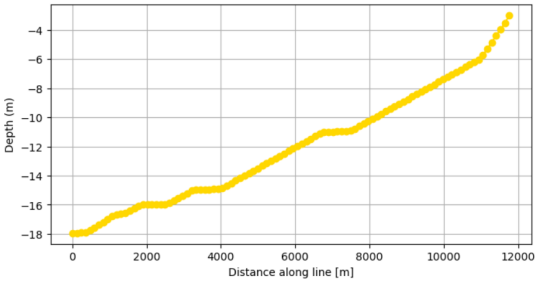

(h) Location 7

Figure F.1: Bathymetry profiles for all considered locations of the SSB in Tokyo Bay.

G

Cost and property value calculation

In this appendix, it is explained how the costs and property value for each proposed barrier location are obtained.

G.1. Costs

The cost of each proposed barrier location is estimated based on the navigational constraint for peak tidal exchange and total gate span, following the approach by Mooyaart et al. (2014). Where an empirical cost formula based on total gate span (Section 2.5.3) plus flow inlet length(Section 2.6.2) is provided:

$$\text{Costs} = 2.2 \cdot L \qquad [\text{million } €] \tag{G.1}$$

An inflation factor of 1.14 is applied for Japan between 2017 and 2025 (Inflation Tool, n.d.), corresponding to a 14% cumulative inflation rate.

Since barrier Location 7 is located near the port of Tokyo, additional measures are needed to protect low-lying areas from high water in the Tama and Edo rivers. Using Google Earth the span of the levees that must be increased is estimated, and it is assumed that the levees must be increased by 3 $[m]$. The total levee cost is calculated by using a cost rate of 0.93 million $[\$/km/m]$ (Kumano et al., 2017). The following exchange rates are used:

$$1 € = 172 ¥, \qquad 1 \$ = 147 ¥.$$

G.2. Property value

Hoshino et al. (2016a) performed research on the economic damage in terms of property value loss to Tokyo in the event of extreme inundations due to extreme storm surge related to a typhoon with a severity similar to that of the Taisho typhoon, while taking into account a sea level rise of 1.9 $[m]$. Following the sample calculation of the economic damage for the Edogawa-ward, the prevented economic damage costs are calculated for each SSB location.

The economic damage in terms of property value to the Edogawa ward is estimated to be 234,29 trillion yen [¥] in 2015 (Hoshino et al., 2016a). Using Population (2022) the area and population density of Edogawa are found in order to obtain compatible damage costs for the different protected areas. By multiplying the damage costs of Edogawa by ratio of the effected area and population density, an estimation of the prevented economic damage costs can be obtained for all locations.

Since the calculation for Edogawa was done in 2015, inflation should be taken into account to acquire representative monetary values. According to Inflation Tool (n.d.) the cumulative inflation rate between 2015 and 2025 is 14.4 %.

In conclusion, Equation G.2 shows how the property value for the protected area of each proposed barrier is obtained.

$$PV_i = \frac{A_i}{A_{Edogawa}} \cdot \frac{P_i}{P_{Edogawa}} \cdot PV_{Edogawa} \cdot I \tag{G.2}$$

Where:

PV_i	Property value of the protected area [¥]
A_i	Surface area of the protected area $\left[m^2\right]$
$A_{Edogawa}$	Surface area of Edogawa $\left[m^2\right]$
P_i	Population density of the protected area $[\#/m^2]$
$P_{Edogawa}$	Population density of Edogawa $[\#/m^2]$
$PV_{Edogawa}$	Property value of Edogawa ¥
I	Factor to account for inflation from 2015 to 2025 [-]

H

Threshold Stability Plots

In this appendix the threshold stability plots are shown, which are used to determine the threshold per window to fit the GPD.

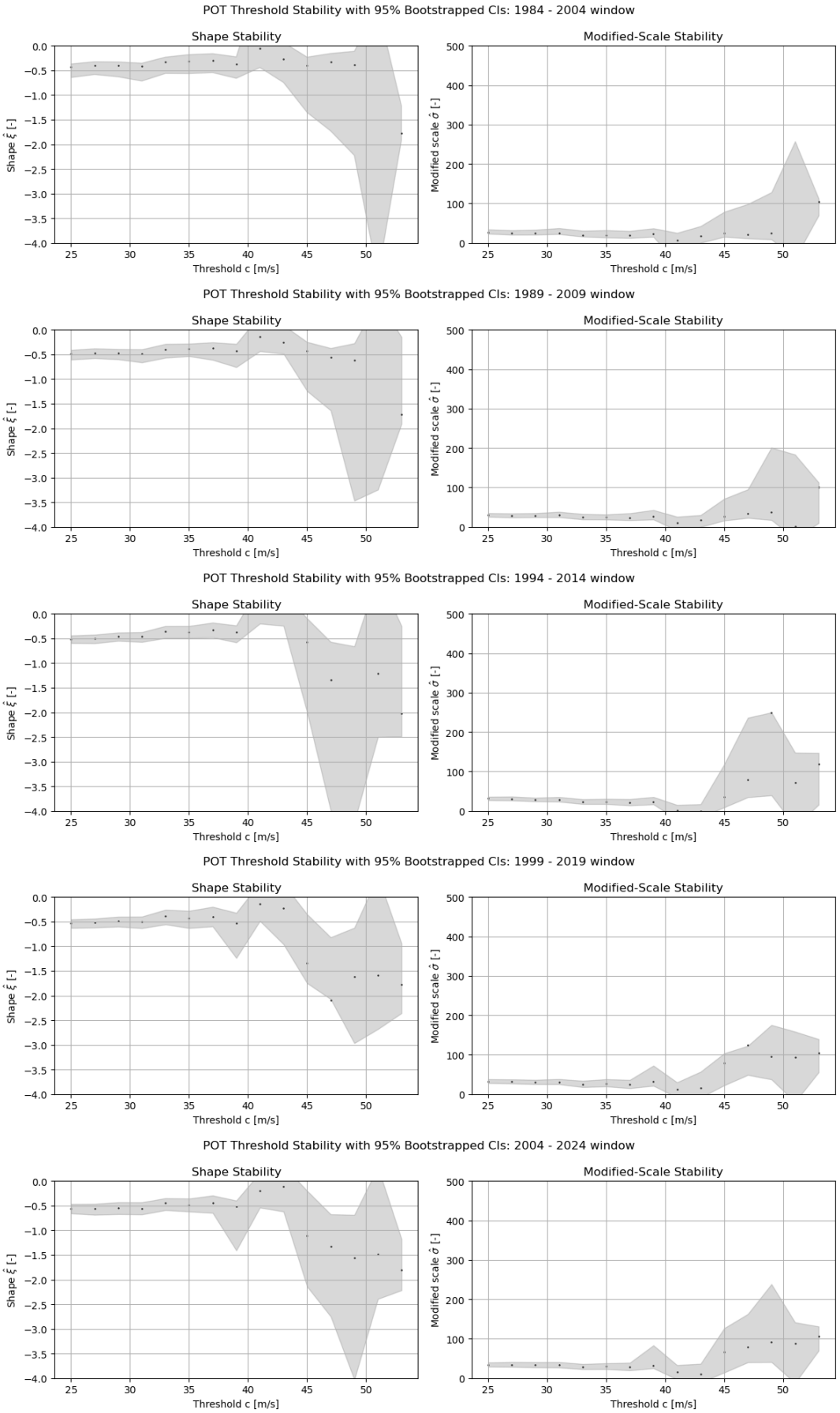

Figure H.1: The plots above show the results of the threshold stability plots of the five windows.

I

Relationship between wind speed and atmospheric pressure

In this appendix, all explored polynomials to describe the relationship between wind speed and atmospheric pressure 18-hour prior to landfall are shown.

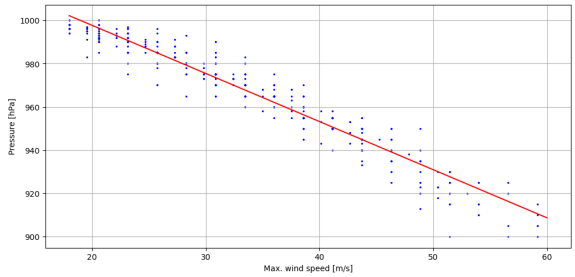

(a) First order polynomial (OMT: Rejected)

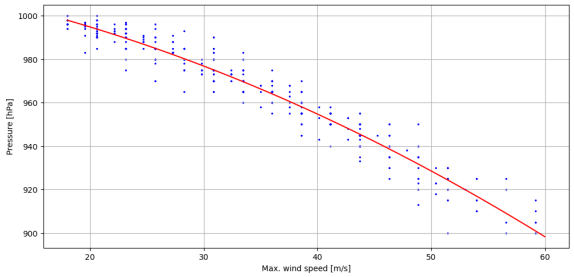

(b) Second order polynomial (OMT: Rejected)

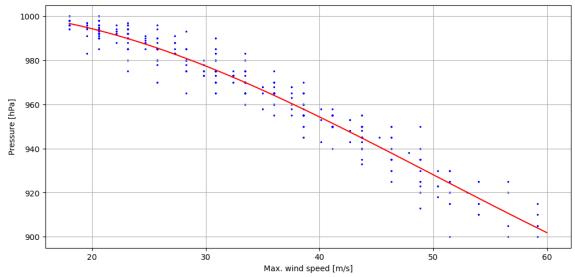

(c) Third order polynomial (OMT: Rejected)

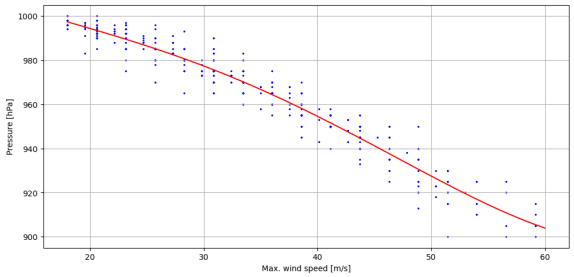

(d) Fourth order polynomial (OMT: Rejected)

Figure I.1: The figure show the different order polynomial exploring the correlation between the wind speed and atmospheric pressure data 18 [h] to landfall.

J

Elaboration and validation of storm surge height formulas

In this appendix the selection of candidate relationships describing the storm surge height is explained. The most suitable formula is identified by validating each candidate against historical typhoon events. The choice of the best-fitting relationship is based on visual inspection and comparison of the R^2 values and the $RMSE$ values. R^2 is also known as the coefficient of determination and represents the proportion of the variance in the dependent variable that is predictable from the independent variables. A value of 1 implies that all the variability in the dependent variable is explained by the independent variables, while a value of 0 suggests that the independent variables do not explain any of the variability. A negative R^2 value means that a statistical model's predictions are worse than simply guessing the mean of the data. $RMSE$ is the root mean squared error and represents the average magnitude of the differences between predicted and actual values, and is calculated by taking the square root of the average of the squared errors. In this report, four different relationships are considered and validated. The four different relationships are outlined below, followed by the validation and conclusion.

Needham and Keim - Needham and Keim investigated the relationship between storm surge heights and tropical cyclone winds at 3-hour increments prior to landfall. The highest correlation was found between storm surge height and wind speeds 18-hours before landfall, where the wind speeds are raised to a power of 2.2 (Needham & Keim, 2013).

Horikawa formula - An empirical formula linking storm surge height to atmospheric pressure, maximum wind speed, and wind direction was proposed by Horikawa in 1978, see Equation J.1 (Horikawa, 1978):

$$H_{ss}[cm] = a\,\Delta p + b\,U_{\max}^2 \cos\theta \tag{J.1}$$

As described by Needham & Keim, the highest correlation between wind speeds of typhoons and the storm surge is found for wind speed 18-hours prior to landfall. Accordingly, for the Horikawa formula, wind speeds 18-hours before landfall are used in this report instead of the maximum wind speeds U_{max} as Horikawa does not specify the location for the maximum wind speed. As a result, the maximum wind speed could occur days before or after hitting Tokyo, which would imply a low correlation with the storm surge in Tokyo.

The formula contains two empirical constants, a and b. For Tokyo, these values are $a = 1.059$ $[cm/mbar]$ and $b = 0.138$ $[cm]$ (Horikawa, 1978). Additionally, θ is defined as the angle between the optimal wind direction for generating the largest storm surge, set to S70E by Horikawa, and the actual wind direction. Δp is equal to the difference between the spatial mean atmospheric pressure over the sea surface, $p = 1010[hPa]$ and the lowest atmospheric pressure on the sea surface. For consistency the latter is replaced by the atmospheric pressure 18-hours prior to landfall. The relationship gives the storm surge height in $[cm]$.

In 2003, **Miyazaki** revised Equation J.1 by Horikawa, 1978 and determined new empirical constants, $a = 2.332$ $[cm/mbar]$ and $b = 0.112$ $[cm]$, and found the optimum wind direction to be S29W (Miyazaki, 2003). These revised constants by Miyazaki are considered the third relationship to be validated.

SSHPI - In 2021, a Storm Surge Hazard Potential Index (SSHPI) was developed, incorporating the maximum wind speed ($V_{\max}$), the radius of 50 $[kt]$ winds (R_{50}), the storm translation speed (S), and information on coastal geometry and bathymetry (L_{30}). This index is created based on data about Japan spanning from 1978 until 2019.

In the formula, R_{ref}, V_{ref}, S_{ref}, and L_* represent reference constants, corresponding respectively to: 50 $[kt]$ (the lower bound of the tropical storm category), 95 [NM] (the historical mean R_{50} at landfall in Japan), and 35 $[km/h]$ (the historical mean storm translation speed at landfall). L_* was set to 30 $[km]$ to ensure that the SSHPI values approximately matched the observed peak storm surge heights in the study area (Islam, Lee, et al., 2021).

The SSHPI is formulated as shown in Equation J.2.

$$\text{SSHPI} = \left(\frac{V_{\max}}{V_{\text{ref}}}\right)^2 \left(\frac{R_{50}}{R_{\text{ref}}}\right) \left(\frac{S}{S_{\text{ref}}}\right)^a \left(\frac{L_{30}}{L_*}\right) \tag{J.2}$$

To convert the SSHPI to storm surge height, the empirical relationship given in Equation J.3 can be used.

$$H_{ss} = 25.14 \cdot \text{SSHPI} + 60.05 \tag{J.3}$$

To validate the four previously selected relationships, the relationships are used to model storm surge heights of historic typhoon events. The observed storm surge heights of the evaluated historic typhoons events are shown in Figure J.1. For each relationship, the simulated storm surge heights are plotted against the actual observed storm surge heights of the evaluated historic typhoons. The results of the validation can be found per evaluated relationship in Figure J.2. The R^2 and $RMSE$ values explaining whether the observed values match the simulated values can be found in Table J.1.

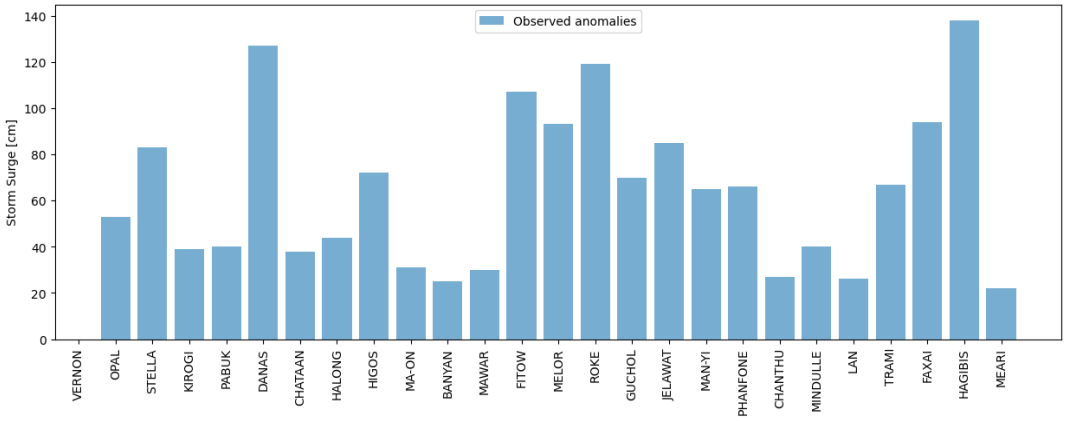

Figure J.1: Observed tidal anomalies during typhoon events 1984 - 2024 (JMA, 2025b).

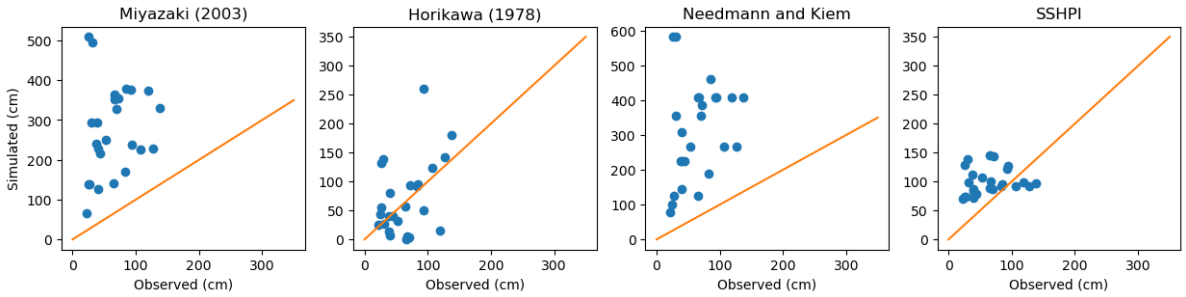

Figure J.2: Observed vs simulated results of storm surge heights.

Formula	R^2	$RMSE$
Horikawa, 1978	-1.95	57.81
Miyazaki, 2003)	-48.80	237.18
Needham and Keim, 2013	-67.38	278.18
SSHPI	-63.57	54.07

Table J.1: R^2 and RMSE for various storm surge formulas.

Figures J.2 and Table J.1 show that both the relation described by Miyazaki and Needham and Keim strongly overestimate the storm surge height. Visually the simulated values using the SSHPI relationship seem to match the observed values better than the previous named relationships. However, based on the R^2 it can be concluded that this relation does not capture the events correctly. The relationship posed by Horikawa seems to provide the best match between observed values and simulated values despite that there still are many outliers as visible in Figure J.2.

K

MCDA gate type

K.1. Method

K.1.1. Criteria

The MCDA for the gates follows a similar procedure as for the barrier location in section 2.2.3. Each gate type is evaluated according to five main criteria.

Ease of construction

Ease of construction depends on several factors. Gate types that have been built repeatedly offer the advantage of accumulated experience, which reduces risks, uncertainty and saves time during planning and execution. Initial costs are also important, since higher upfront investment can limit feasibility. Constructional complexity influences both the duration and the need for specialized skills, with more intricate gates requiring longer build times and highly trained workforces. Finally, modularity can improve constructability by allowing large components to be prefabricated off-site and installed more efficiently, reducing on-site challenges and delays.

Required space

The gates require a certain amount of space for construction and storage, which varies depending on the gate type. Some gates are stored in the water, while others are kept dry on land. Additional land requirements lead to higher costs. The more land is needed, the larger the costs. Therefore, the gate type that requires the least extra land is generally the most cost-effective.

Ease of maintenance

Ease of maintenance depends largely on the number of moving parts, as more components increase failure risk, inspection needs, and costs. Sediment buildup can further complicate operations, requiring frequent dredging or cleaning. Accessibility is equally important: gates designed for safe, direct access reduce risks and time for repair crews. Maintenance costs vary with structural complexity, servicing frequency, and whether work can be done on land or must occur underwater, the latter being far more demanding. Simpler, more accessible designs therefore tend to offer greater reliability and lower long-term costs.

Adaptability

Adaptability reflects the gate's capacity to accommodate future upgrades or functional modifications without requiring complete reconstruction. As environmental conditions and operational demands evolve, designs that allow for the integration of new technologies or increased protection levels are advantageous. This criterion also includes the ability of the gate to resist hydraulic head from both directions, as some gate types are primarily designed to withstand pressure from one side only. Structures that combine structural flexibility with bidirectional stability offer greater long-term value and resilience.

Operation time

Operation time covers both the speed of closure in response to sudden events, such as a tsunami and the speed of reopening so that shipping traffic can resume quickly. Rapid reopening is also vital due to potential heavy rainfall raising water levels behind the gates, since prolonged closure increases flood risk. Gates with long operation times may therefore reduce safety and disrupt navigation, while designs that allow both reliable closure and swift reopening minimize risks and economic impacts.

K.1.2. Scoring

Each gate type is rated qualitatively from $--$ to $++$, corresponding to numerical values from 1 to 5, as shown in Table 2.1. The scores are assigned based on literature and engineering reasoning (Aerts et al., 2013; Daniel & Paulus, 2019; Mooyaart & Jonkman, 2017; Nakayasu, 2024; Tara, 2023).

K.1.3. MCDA weights

The relative importance of the evaluation criteria was established using a pairwise comparison matrix, similar to Section 2.2.3. The resulting weights are shown in Table K.3.

K.1.4. Weighted sum

The weighted MCDA score for each gate is calculated by multiplying the scores with the corresponding weight and adding these results for each gate type.

K.2. Results

Criteria

Table K.1 shows the assessment of each gate type on each criterion.

Table K.1: Comparison of gate types, using predefined criteria.

Criteria	**Sector Gate**	**Flap Gate**	**Inflatable Gate**	**Rotary Segment Gate**
Ease of construction	above water, non-modular, high complexity, moderate experience, very high initial costs [1, 4]	under water, modular, moderate complexity, moderate experience, high initial costs [1, 2, 5]	underwater, non-modular, little experience, lower initial costs [1, 3, 4]	under water, modular, high complexity, high experience, high initial costs [1, 4]
Required space [m^2]	requires space for large dry docks [1]	small footprint [1, 5]	small footprint [1]	moderate footprint [1]
Ease of maintenance	moving parts of high complexity, barely influenced by sediment build up, easily accessible [1]	few and small mechanical parts, sediment build up has some influence, accessible but under water so divers are needed [1, 2, 5]	no moving parts, sediment build up has some influence, under water and harder to access [1]	lots of hydraulic and mechanical parts and electric circuitry, strong influence by sediment build up, gates can be lifted above water but hinges are only accessible underwater [1]
Adaptability	almost no adaptability, can not handle water from backside	gates could be upgraded but it should already be accounted for in advance	rubber dam could be upgraded but difficult and expensive	almost no adaptability, uncertain how well it can handle water from backside

Criteria	Sector Gate	Flap Gate	Inflatable Gate	Rotary Segment Gate
Operation Time	slow opening and closing time [1]	fast opening and relatively fast closing [1, 5]	slow opening and closing time due to massive volume of air or water that needs to be pumped [1]	moderately fast opening and closing time [1]

Sources:
[1] Daniel and Paulus, 2019
[2] Tara, 2023
[3] Aerts et al., 2013
[4] Mooyaart and Jonkman, 2017
[5] Nakayasu, 2024

K.2.1. Scoring

Table K.2 presents the assigned qualitative scores of the gates to each criterion.

Table K.2: Qualitative comparison of gate types. Symbols defined in Table 2.1.

Criteria	Sector	Flap	Inflatable	Rotary
Ease of construction	+	-	-	- -
Required space [m^2]	- -	++	++	0
Ease of maintenance	+	- -	- -	+
Adaptability	-	+	0	- -
Operation Time	-	++	- -	0

K.2.2. MCDA weights

The resulting normalized weights indicate that *ease of construction* is considered the most important factor, followed by *ease of maintenance*, while *required space*, *adaptability*, and *operation time* have lower relative influence (Table K.3).

Table K.3: Pairwise comparison matrix and resulting normalized weights.

Criteria	a	b	c	d	e	**Sum**	**Weight**
Ease of construction (a)	x	1	1	1	1	4	0.3077
Required space (b)	0	x	0	1	0	1	0.0833
Ease of maintenance (c)	0	1	x	1	1	3	0.2500
Adaptability (d)	0	1	0	x	1	2	0.1667
Operation time (e)	0	1	0	1	x	2	0.1667

K.2.3. Weighted sum

Table 3.27 presents the final weighted MCDA results.

Table K.4: Final result of the MCDA for the gate type of the SSB, combining the qualitative scores per criterion with their associated weight.

Criteria	Sector Gate		Flap Gate		Inflatable Gate		Rotary Segment Gate	
	S	S*W	S	S*W	S	S*W	S	S*W
Ease of construction	4	1.2308	2	0.6154	2	0.6154	1	0.3077
Required space [m^2]	1	0.0833	5	0.4167	5	0.4167	3	0.2500
Ease of maintenance	4	1.0000	1	0.2500	1	0.2500	4	1.0000
Adaptability	2	0.3333	4	0.6667	3	0.5000	1	0.1667
Operation Time	2	0.3333	5	0.8333	1	0.1667	3	0.5000
Total		3.3077		3.4615		1.6154		3.0000

The flap gate ranks as the most favorable option overall, offering a balance between constructability, spatial efficiency, and adaptability. Its main drawbacks include the need for underwater maintenance and potential sediment buildup. Future work should investigate its durability and maintenance strategy under Tokyo Bay conditions.

L

Considered Gate Types

For the gate design, a proper gate type must be selected. Four gate types are considered: sector gate, flap gate, inflatable gate and rotary segment gate. The characteristics of these gates are discussed below.

L.1. Sector gate

Figure L.1: Top view of a sector gate (Mooyaart & Jonkman, 2017).

Vertically hinged sector gates have a circular shape, and have been applied in many other barriers, such as the Maeslantkering. It is a double gated mechanism (Mooyaart and Jonkman, 2017). The gates can be applied for wide openings up to 300 meters and its maintenance can be done above water. On the other hand, much space is required to harbor these large gates, and the system is quite complex and expensive (Daniel & Paulus, 2019). A simple sketch of this gate type can be seen in Figure L.1

L.2. Flap gate

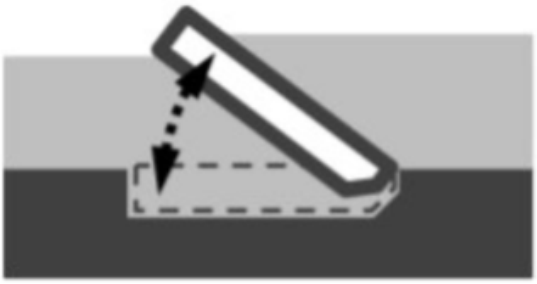

Figure L.2: Cross-section of a flap gate (Mooyaart & Jonkman, 2017).

Flap gates have a retaining surface that can be straight or curved, and are hinged at a fixed axis (Erbisti, 2014). This axis can be at sill level or has its axis above water level (Mooyaart and Jonkman, 2017). By filling the gates with air, the gates are put in closed position. In fully open position, the gates lie on the waterway floor. Therefore, there is no maximum vertical clearance height, but maintenance should be done in the water, leading to high maintenance costs. Due to its relatively simple design, the initial costs are low. Flap gates allow for the opportunity of an analog system, which increases resilience during a power failure, for instance. in this preliminary design the choice is made to look into the flap gates of the type that the Kanadevia company in Japan designs and makes, since they are relatively unknown and they look like a promising solution. A simple sketch of a classical flap gate can be seen in Figure L.2

L.3. Inflatable gate

Figure L.3: Cross-section of an inflatable gate (Mooyaart & Jonkman, 2017).

Inflatable gates are made of flexible material and rest on the sill and walls, imposing no hindrance to navigation. When needed, the gate is inflated with air and/or water (Mooyaart & Jonkman, 2017). The inflatable gates can be used up to a span of eighty meter. Different material choices are possible as flexible material, and for inflation. However, the material is vulnerable to punching loads and UV-light, and there are risks of instability (Daniel & Paulus, 2019). A simple sketch of this gate type can be seen in Figure L.3

L.4. Rotary segment gate

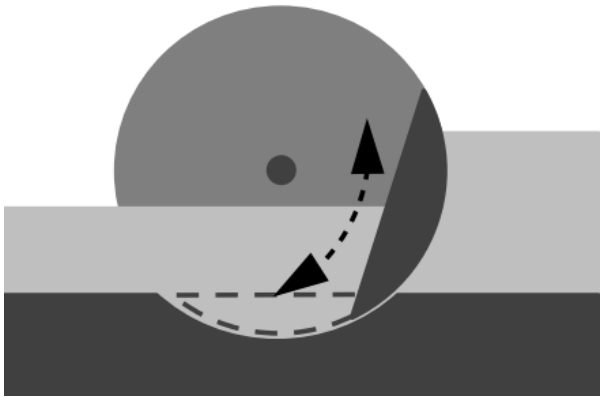

Figure L.4: Cross-section of a rotatory segment gate (Mooyaart & Jonkman, 2017).

This curved gate rotates around a horizontal axis and is lifted in open position. Rotary gates are found in several other SSBs, i.e. Thames Barrier (Mooyaart and Jonkman, 2017). Hence, much experience has been gained on its performance. Up to 80 meters width can be spanned by these gates, and its inspection and maintenance can be done above water. The gates are suitable for navigation openings. In contrast, the gates are relatively expensive and debris could accumulate at the bottom (Daniel & Paulus, 2019). A simple sketch of this gate type can be seen in Figure L.4

M

Calculations dimensions and loads on flap gate

In this appendix the calculations performed to determine the dimensions of the flap gate and the acting loads are presented.

The height-to-width ratio of the Kanadevia flap gate (Coastal Technology Research Center, 2020):

$$h_{Kanadevia}/B_{Kanadevia} = 13/8 = 1.625$$

Based on the height-to-width ratio, the width of the flap gate is estimated:

$$B = \frac{32.86}{1.625} = 20.22 \text{ [m]}$$

The area of the skin plate is calculated by multiplying the height of the flap gate by the width:

$$A_{skin\,plate} = B \cdot h = 20.22 \cdot 32.86 = 664.4 \ [m^2]$$

The ratio between the flap gate height and the length of the substructure of the Kanadevia flap gate is calculated as follows:

$$h_{Kanadevia}/L_{Kanadevia} = 13/19.5 = 0.67$$

The length of the substructure for the Tokyo Bay flap gate is calculated with the gate height and the ratio of the Kanadevia flap gate:

$$L = \frac{32.86}{0.67} = 49.29 \text{ [m]}$$

The depth-to-length ratio of the Kanadevia flap gate is calculated as follows:

$$d_{Kanadevia}/L_{Kanadevia} = 6/19.50 = 0.31$$

The depth of the Tokyo Bay flap gate is calculated with the depth-to-length ratio of the Kanadevia flap gate and the length of the Tokyo Bay substructure:

$$d = 0.31 \cdot 49.29 = 15.17 \text{ [m]}$$

The remaining lengths of the flap gate are calculated based on the dimensional ratios of the Kanadevia flap gate and the total length of the Tokyo Bay substructure:

$$w_1 = \frac{w_{1\,Kanadevia}}{L_{Kanadevia}} \cdot L = \frac{1.9}{19.50} \cdot 49.29 = 4.80 \ [m]$$

$$w_2 = \frac{w_{2\,Kanadevia}}{L_{Kanadevia}} \cdot L = \frac{2.525}{19.50} \cdot 49.29 = 6.38\ [m]$$

$$w_3 = \frac{w_{3\,Kanadevia}}{L_{Kanadevia}} \cdot L = \frac{2}{19.50} \cdot 49.29 = 5.06\ [m]$$

Wind load

Using the parameters from the methodology, the wind speed on the gate is determined:

$$p_{wind} = 0.5 \cdot \rho_{air} \cdot U_{10}^2 = 0.5 \cdot 1.225 \cdot 58.4^2 = 2.1\ [kN/m^2]$$

The exposed height is taken as $0.55 \cdot H_{max} = 0.55 \cdot 7 = 3.85\ [m]$, based on the closed gate geometry. Acting over the exposed section of 3.85 $[m]$, the resulting line load per unit gate width equals:

$$F_{wind} = p_{wind} \cdot h_{wind} = 2.1 \cdot 3.85 = 8.1\ [kN/m]$$

Equation 2.51 can be improved upon by introducing location, dimension and/or other factors. These vary depending on the region the structure is located in.

Hydrostatic load

The hydrostatic loads are determined using the equation from the methodology. The hydrostatic pressure underneath the substructure

$$H_1 = \frac{1}{2} \cdot \rho_{water} \cdot g \cdot (D_{max} + d)^2 = 0.5 \cdot 1025 \cdot 9.81 \cdot (25.25 + 15.21)^2 = 8.231 \cdot 10^6\ [N/m] = 8172\ [kN/m]$$

$$H_2 = -\frac{1}{2} \cdot \rho_{water} \cdot g \cdot (LAT + d)^2 = -0.5 \cdot 1025 \cdot 9.81 \cdot (21.35 + 15.21)^2 = -6.721 \cdot 10^6\ text[N/m]\ =\ -6704\ [kN/m]$$

$$V_1 = 0.5 \cdot \rho_{water} \cdot g \cdot (D_{max} + d - LAT - d) \cdot L$$

$$= 0.5 \cdot 1025 \cdot 9.81 \cdot (32.86 - 21.35) \cdot 49.29 = 941650\ [N/m] = 942\ [kN/m]$$

$$V_2 = \rho_{water} \cdot g \cdot (LAT + d) \cdot L$$

$$= 1025 \cdot 9.81 \cdot (21.35 + 15.17) \cdot 49.29 = 18097320\ [N/m] = 18097\ [kN/m]$$

Wave load

The wave loads are determined using the equations from the methodology: The design wave height is:

$$H_d = 1.8 \cdot H_s = 1.8 \cdot 4.38 = 7.0\ [m]$$

The height above the still water level (SWL) influenced by waves is:

$$\eta = 0.75 \cdot H_d = 0.75 \cdot 7 = 5.9\ [m]$$

The design wave length is:

$$L_d = \frac{g \cdot T^2}{2\pi} = \frac{9.81 \cdot 7.19^2}{2\pi} = 80.7\ [m]$$

The wave pressure factor at SWL is:

$$\alpha_1 = 0.6 + 0.5 \cdot \left(\frac{4\pi \frac{h}{L_d}}{sinh(4\pi \frac{h}{L_d})} \right)^2 = 0.6 + 0.5 \cdot \left(\frac{4\pi \frac{32.86}{80.7}}{sinh(4\pi \frac{32.86}{80.7})} \right)^2 = 0.61\ [-]$$

The wave pressure at SWL is:

$$p_1 = \alpha_1 \cdot \rho_{water} \cdot g \cdot H_d = 0.61 \cdot 1025 \cdot 9.81 \cdot 7.0 = 48532 \ [N/m^2]$$

The wave pressure at the bottom is:

$$p_2 = \frac{p_1}{cosh(2\pi \cdot \frac{h}{L_d})} = \frac{48532}{cosh(2\pi \cdot \frac{32.86}{80.7})} = 13434 \ [N/m^2]$$

the wave pressure at the top is:

$$p_3 = p_1 - p_1 \cdot \frac{1.1 \cdot H_s}{\eta} = 48532 - 48532 \cdot \frac{1.1 \cdot 4.38}{5.9} = 8987 [N/m^2]$$

The wave force is subdivided into four components, a top, intermediate, bottom and surface component, see Figure 3.30.

$$H_{w1} = 0.5 \cdot 1.1 \cdot H_s \cdot (p_1 - p_3) = 0.5 \cdot 1.1 \cdot 4.38 \cdot (48532 - 8987) = 95.262 \ [[N/m] = 95 \ [kN/m]$$

$$H_{w2} = 0.5 \cdot (p_1 - p_2) \cdot h = 0.5 \cdot (48532 - 13434) \cdot 32.96 = 441347 \ [N/m] = 441 \ [kN/m]$$

$$H_{w3} = p_2 \cdot h = 13434 \cdot 32.96 = 337874 \ [N/m] = 338 \ [kN/m]$$

$$H_{w4} = p_3 \cdot 1.1 \cdot H_s = 8987 \cdot 1.1 \cdot 4.38 = 43301 \ [N/m] = 43 \ [kN/m]$$

Self-weight

The self weight of the flap gate, the substructure and the water column above the substructure are determined using the equation from the methodology:

$$G_{flap} = G_{main\,beam} + G_{sub\,beam} + G_{girder} + G_{skin\,plate}$$

$$G_{main\,beam} = -\rho_{steel} \cdot g \cdot \pi \cdot (D_{out} - t) \cdot t \cdot L$$

$$= -7800 \cdot 9.81 \cdot \pi \cdot (0.76 - 0.03) \cdot 0.03 \cdot 98.58 = -519729 \ [N] = -520 \ [kN]$$

$$G_{sub\,beam} = -\rho_{steel} \cdot g \cdot \pi \cdot (D_{out} - t) \cdot t \cdot L = -7800 \cdot 9.81 \cdot \pi \cdot (0.24 - 0.02) \cdot 0.02 \cdot 202.21 = -100934 \ [N] = -101 \ [kN]$$

$$G_{girder} = -\rho_{steel} \cdot g \cdot \pi \cdot (D_{out} - t) \cdot t \cdot L = -7800 \cdot 9.81 \cdot \pi \cdot (0.08 - 0.003) \cdot 0.03 \cdot 230.01 = -12127 \ [N] = -12 \ [kN]$$

$$G_{skin\,plate} = -\rho_{steel} \cdot g \cdot t \cdot A = -7800 \cdot 9.81 \cdot 0.025 \cdot 664.4 = -3993039 \ [N] = -3993 \ [kN]$$

$$G_{flap} = -520 - 101 - 12 - 3993 = -4626 \ [kN]$$

To evaluate the flap gate at a cross-sectional level, the self-weight of the flap gate is divided by the width of the barrier, thereby assuming that the weight is equally spread across the width. However, this is not the case in reality.

$$G_{flap\,avg\,width} = \frac{G_{flap}}{B} = \frac{-4626}{20.22} = -229 \ [kN/m]$$

$$G_s = -\rho_{concrete} \cdot g \cdot V_{concrete} =$$

$$= -\rho_{concrete} \cdot g \cdot (w_1 \cdot d + w_2 \cdot (d - D_{tubular}) + w_3 \cdot d + (L - w_1 - w_2 - w_3) \cdot \frac{1}{3} d)$$

$$= -2400 \cdot 9.81 \cdot (4.80 \cdot 15.17 + 6.38 \cdot (15.17 - 2) + 5.06 \cdot 15.17 + (49.29 - 4.80 - 6.38 - 5.06) \cdot \frac{1}{3} \cdot 15.17$$

$$= -9431456 \ [N/m] = -9431 \ [kN/m]$$

$$G_w = -\rho_{water} \cdot g \cdot V_{water} = -\rho_{water} \cdot g \cdot l \cdot L$$

$$= -1025 \cdot 9.81 \cdot 32.86 \cdot 49.29 = -12464470 \ [N/m] = -12464 \ [kN/m]$$

Buoyancy

The buoyancy is determined using the equation from the methodology:

$$V_{b\,flap} = V_{b\,main\,beam} + V_{b\,sub\,beam} + V_{b\,girder} + V_{b\,skin\,plate}$$

$$V_{b\,main\,beam} = \rho_{water} \cdot g \cdot \pi \cdot L \cdot 0.25 \cdot D_{out}^2 = 1025 \cdot 9.81 \cdot \pi \cdot 98.58 \cdot 0.25 \cdot 0.76^2 = 444646\ [N] = 444\ [kN]$$

$$V_{b\,sub\,beam} = \rho_{water} \cdot g \cdot \pi \cdot L \cdot 0.25 \cdot D_{out}^2 = 1025 \cdot 9.81 \cdot \pi \cdot 202.21 \cdot 0.25 \cdot 0.24^2 = 86352\ [N] = 86\ [kN]$$

$$V_{b\,girder} = \rho_{water} \cdot g \cdot \pi \cdot L \cdot 0.25 \cdot D_{out}^2 = 1025 \cdot 9.81 \cdot \pi \cdot 230.01 \cdot 0.25 \cdot 0.08^2 = 10375\ [N] = 10\ [kN]$$

$$V_{b\,skin\,plate} = \rho_{water} \cdot g \cdot A \cdot t = 1025 \cdot 9.81 \cdot \cdot 664.4 \cdot 0.025 = 167026\ [N] = 167\ [kN]$$

$$V_{b\,flap} = 444 + 86 + 10 + 167 = 708\ [kN]$$

To evaluate the flap gate at a cross-sectional level the buoyancy of the flap gate is divided by the width of the barrier, thereby assuming that the buoyancy is equally spread across the width. However, this is not the case in reality

$$V_{b\,flap\,avg\,width} = \frac{V_{b\,flap}}{B} = \frac{708}{20.22} = 35\ [kN]$$